Advanced Engineering Research

Theoretical and scientific-practical journal

Vol. 22

no. 1

2022

ISSN 2687-1653

1 Mechanics

2 Machine Building and Machine Science

3 Information Technology, Computer Science, and Management

DOI 10.23947/2687-1653

vestnik-donstu.ru

Theoretical
and scientific-practical journal

Advanced Engineering Research

Vol. 22, no. 1

Published since 1999

Quarterly
January-March 2022

ISSN 2687-1653
DOI: 10.23947/2687-1653

Founder and publisher ─ Federal State Budgetary Educational Institution of Higher Education

Don State Technical University (DSTU)

The journal was known as Vestnik of Don State Technical University (until August 2020)

Included in the list of peer-reviewed scientific editions where the basic research results of doctoral, candidate's theses should be published (State Commission for Academic Degrees and Titles List) in the following research areas:

01.02.01 – Analytical Mechanics (Engineering Sciences)
01.02.04 –Deformable Solid Mechanics (Engineering Sciences)
01.02.04 –Deformable Solid Mechanics (Physicomathematical Sciences)
01.02.06 – Dynamics, Strength of Machines, Gear, and Equipment (Engineering Sciences)
05.02.02 – Engineering Science, Drive Systems and Machine Parts (Engineering Sciences)
05.02.04 –Machine Friction and Wrear (Engineering Sciences)
05.02.07 – Technology and Equipment of Mechanical and Physicotechnical Processing (Engineering Sciences)
05.02.08 – Engineering Technology (Engineering Sciences)
05.02.10 –Welding, Allied Processes and Technologies (Engineering Sciences)
05.02.11 – Testing Methods and Diagnosis in Machine Building (Engineering Sciences)
05.13.11 – Software and Mathematical Support of Machines, Complexes and Computer Networks (Engineering Sciences)
05.13.17 – Foundations of Information Science (Engineering Sciences)
05.13.18 –Mathematical Simulation, Numerical Methods and Program Systems (Engineering Sciences)

The journal is indexed and archived in the Russian Science Citation Index (RSCI), in the International Database EBSCO (Academic Search Ultimate Magazines and Journals), Dimensions, CyberLeninka, ROAD, GoogleScholar. The journal is a member of Directory of Open Access Journals (DOAJ), Association of Science Editors and Publishers (ASEP) and CrossRef.

Certificate of mass media registration ЭЛ № ФС 77 – 78854 of 07.08.2020 is issued by the Federal Service for Supervision of Communications, Information Technology, and Mass Media

The issue is prepared by:

Inna V. Boyko, Gennady I. Rassokhin, Marina P. Smirnova (English version)

Founder's, Publisher's and Printery Address:

Gagarin Sq. 1, Rostov-on-Don, 344003, Russia. Phone: +7 (863) 2-738-372

E-mail: vestnik@donstu.ru http://vestnik-donstu.ru/

CONTENTS

MECHANICS

MACHINE BUILDING AND MACHINE SCIENCE

INFORMATION TECHNOLOGY, COMPUTER SCIENCE, AND MANAGEMENT

MECHANICS

Check for updates

UDC 539.3

Original article

https://doi.org/10.23947/2687-1653-2022-22-1-4-13

Vibration analysis of a composite magnetoelectroelastic bimorph depending on the volume fractions of its components based on applied theory

Arkadiy N. Soloviev[1,2], **Do Thanh Binh**[1], **Valerii A. Chebanenko**[3], **Olga N. Lesnyak**[1], **Evgeniya V. Kirillova**[4]

[1]Don State Technical University (Rostov-on-Don, Russian Federation)

[2]Southern Federal University (Rostov-on-Don, Russian Federation)

[3]Federal Research Centre the Southern Scientific Centre of the Russian Academy of Sciences (Rostov-on-Don, Russian Federation)

[4]Rhein-Main University of Applied Sciences (Wiesbaden, Germany)

✉ solovievarc@gmail.com

Introduction. Transverse vibrations of a bimorph consisting of two piezomagnetoelectric layers and located in the alternating magnetic field are investigated. Piezomagnetoelectric layers are multilayer composites with alternating piezoelectric and piezomagnetic layers. The mechanical and physical properties of such a composite are given by known effective constants.

Materials and Methods. The applied theory of multilayer plate vibrations takes into account the nonlinear distribution of electric and magnetic potential in piezoactive layers in the longitudinal and transverse directions. On the basis of this theory, the stress-strain state, the dependences of deflection, electric and magnetic potentials on the volume ratio of the composition of the hinged bimorph, are investigated. The electric potential is assumed to be zero at all electrodes, while the magnetic potential is zero at the inner boundary and unknown at the outer boundaries. Therefore, the distribution of electric and magnetic potentials in the middle of the layer are unknown functions. In the case of the magnetic potential, the distribution at the outer boundary is also unknown. In the problem, the Kirchhoff hypotheses for mechanical characteristics were accepted. The use of the variational principle and the quadratic dependence of the electric and magnetic potentials on the thickness of piezoactive layers made it possible to obtain a system of differential equations and boundary conditions.

Results. When the volume ratio of the composition of piezoactive bimorph materials changes, the electric potential in the middle of the layer changes nonlinearly. The magnetic potential in the middle of the layer and at the outer boundary increases almost linearly with an increase in the volume percentage of $BaTiO_3$. The dependence of the deflection in the middle of the layer is determined.

Discussion and Conclusions. An applied theory for calculating transverse vibrations of a bimorph with two piezomagnetoelectric layers is constructed. The dependence of the characteristics of the stress-strain state, electric and magnetic fields on the volume fractions of piezomagnetic and piezoelectric materials, is investigated.

Keywords: piezoelectrics, piezomagnetics, composite, bimorph, magnetoelectroelasticity, bending vibrations.

For citation: Soloviev, A. N., Do Thanh Binh, Chebanenko, V. A., Lesnyak, O. N., Kirillova, E. V. Vibration analysis of a composite magnetoelectroelastic bimorph depending on the volume fractions of its components based on applied theory. Advanced Engineering Research, 2022, vol. 22, no. 1, pp. 4–13. (In Russ). https://doi.org/10.23947/2687-1653-2022-22-1-4-13

Funding information: The work (first author) was supported by the Government of the Russian Federation (contract No. 075-15-2019-1928). The third author carried out work within the framework of the State Assignment of the Southern Scientific Center of the Russian Academy of Sciences (State Reg. Project AAA-A-A16-116012610052-3).

Introduction. In the production of sensor and measuring systems, small household appliances, cell phones, and wireless sensor systems, powerful energy sources are not needed to monitor and diagnose the technical condition of objects. In this case, the prerequisites are the mobility and volatility of the above devices.

Piezoelectric materials directly convert electrical energy into mechanical energy and vice versa. This property allows them to be widely used in science and technology. These materials are used in ultrasonic emitters of elastic and acoustic waves, receivers of such waves, devices for suppressing vibrations of machine elements and structures, etc. Recently, another field of application of piezoelectrics has been rapidly developing — energy collection and storage devices. In this case, piezoelectric materials are part of piezoelectric energy generators (PEG). PEG are placed on elements of machines or structures that vibrate intensively, which are in the zone of elastic wave propagation or are exposed to variable pressure. The main types of these devices have a bimorph or stack multilayer structure and experience bending or longitudinal deformations, respectively. Low-power sources of electric current are created on the basis of PEG. They include autonomous power sources (e.g., for damage monitoring devices in hard-to-reach places of pipeline structures, etc.). An overview of such devices is available in [1–2]. One of the ways to design effective PEG is the use of piezoactive composites of various types of connectivity and heterogeneous materials based on piezoceramics, including porous one.

PEG, in whose design there are additional electromagnetic elements or permanent magnets, can fix or use the energy of an alternating magnetic field. One of the ways to solve this problem is the use of piezomagnetic materials in combination with piezoelectric ones. In this case, the alternating magnetic field causes the deformation of the piezomagnetic and the coupled piezoelectric, as a result, the latter generates electrical energy. There is a class of materials with ferromagnetic properties. Piezomagnetism is a phenomenon observed in some antiferromagnetic and ferromagnetic crystals. It is characterized by a linear relationship between the magnetic polarization of the system and mechanical deformation. In a piezomagnetic material, a spontaneous magnetic moment can be induced through applying mechanical stress, or deformation by applying a magnetic field. In studies of piezomagnetic materials [3–5], $CoFe_2O_4$ is very often considered. In [6–8], a composite based on $CoFe_2O_4$ and $BaTiO_3$ with piezoelectric and piezomagnetic properties is studied simultaneously.

Solutions to the problems of electroelasticity and magnetoelasticity are given in [9–11]. In [12], applied theories of vibrations of multilayer piezoelectric plates were developed considering the specifics of the distribution of electric potential over the structure thickness.

The problems on steady-state oscillations of an electro-magneto-elastic layer and a half-space under the action of harmonic loads are presented in [13, 14]. The prestressing is taken into account, as well as various electrical and magnetic conditions at the boundaries. The effect of these factors on the dispersion properties is investigated.

Earlier [15, 16], an applied theory was developed that considers the inhomogeneous distribution of the electric potential in the longitudinal direction, and the quadratic dependence on thickness. In the same papers, the stress-strain and electrical state of a hinged and cantilevered bimorph is investigated. In both cases, the applied theory showed good convergence with the finite element modeling results. The authors also developed an applied theory of bimorph vibrations [17] consisting of an electroelastic and magnetoelastic layer. This approach is in good agreement with the finite element analysis results.

In this paper, the vibrations of the device are considered in the framework of a plane deformation. Based on the variational principle, an applied theory of bending vibrations of a two-layer piezoelectric bimorph is constructed. For steady-state vibrations, boundary conditions and a system of differential equations are obtained for four unknown functions (deflection, electric potential in the middle of the layer, magnetic potential in the middle of the layer and at the outer boundary), depending on the length of the bimorph. The influence of different percentage volume ratios of the bimorph composition on deflection, electric and magnetic potentials in certain positions, is investigated. The study results provide selecting the makeup of a composite piezomagnetoelectric material to achieve the most efficient operation of the device.

Materials and Methods. A plate consisting of two identical piezoelectric layers is considered. It performs steady-state transverse vibrations within a plane deformation. Each layer is a 2–2 connectivity composite consisting of alternating piezoelectric and piezomagnetic layers (Fig. 1).

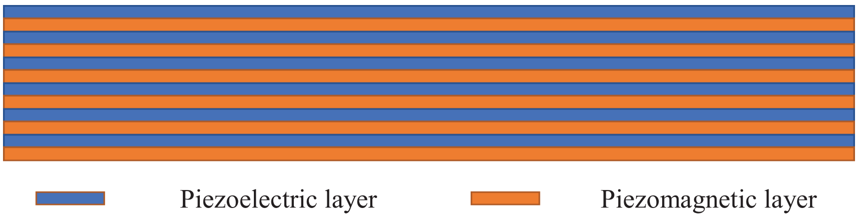

Fig. 1. 2-2 composite structure

Effective properties of such a composite were found in [8]. Large surfaces of the layers are electrodated, and the layers themselves are polarized in thickness. The bimorph is hinged at the edges, all surfaces are free from mechanical stresses. The upper and lower boundaries of the plate are affected by magnetic flux B_0, while at the boundary between the layers, the magnetic potential is considered to be zero. The electrical potential is zero at all electrodes. The side surfaces are considered to be insulated from magnetic and electric fields.

The equations for describing the vibrations of a composite with effective properties, connectivity of mechanical, electric and magnetic fields, have the form [18]:

$$\nabla\cdot\sigma+\rho f=\rho\ddot{u},\quad \nabla\cdot D=\sigma_\Omega,\quad \nabla\cdot B=0,$$
$$\sigma=c:\varepsilon-e^T\cdot E-h^T\cdot H,$$
$$D=e:\varepsilon+\kappa\cdot E+\alpha\cdot H,$$
$$B=h:\varepsilon+\alpha^T\cdot E+\mu\cdot H,$$
$$\varepsilon=\frac{1}{2}\left(\nabla u+\left(\nabla u\right)^T\right),\quad E=-\nabla\varphi,\quad H=-\nabla\xi. \tag{1}$$

Here, σ and ε — mechanical stress and strain tensors, D and E — vectors of electric induction and electric field strength, B and H — vectors of magnetic induction and magnetic field strength, ρ — material density, c — elastic moduli tensor, e — piezoelectric moduli tensor, h — piezomagnetic moduli tensor, κ — dielectric permittivity tensor, α — magnetoelectric moduli tensor, μ — magnetic permeability tensor, f — mass force density vector, σ_Ω — electric charge volume density, u — displacement vector, φ and ξ — electrical and magnetic potentials.

The boundary conditions are determined for the mechanical, electric and magnetic fields, respectively.

For the first case, we note the absence of mechanical stresses at the bimorph boundary:

$$\sigma_{ij}\cdot n_j\big|_S=0,\qquad i,j=1.3.$$

The biomorph is hinged at the ends (Fig. 2):

$$u_i\big|_{(0,0)} = u_i\big|_{(L,0)} = 0, \qquad i = 1.3\,.$$

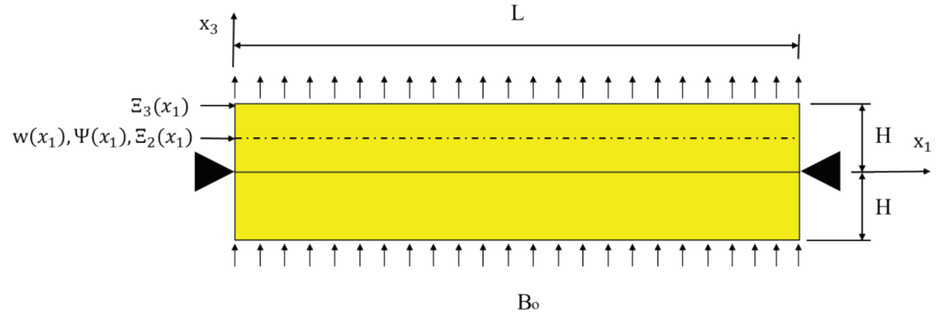

Fig. 2. Geometry and boundary conditions of bimorph with composite piezomagnetoelectric layers

Next, we formulate the electrical boundary conditions. Electrical potential on the internal and external electrode, respectively:

$$\varphi\big|_{x_3=0} = V_0, \qquad \varphi\big|_{x_3=H} = V_2\,.$$

We indicate the magnetic boundary conditions. Magnetic potential at the inner boundary:

$$\xi\big|_{x_3=0} = M_0\,.$$

Magnetic flux B_0 affects the upper and lower boundaries of the plate:

$$H\big|_{x_3=\pm H} = B_0\,.$$

We use the variational equation for steady-state vibrations [10]. It generalizes Hamilton's principle in the electroelasticity theory taking into account magnetic components. For the case of plane deformation in the absence of surface loads and in the presence of magnetic flux:

$$\iint_S \delta\tilde{H}dS - \rho\omega^2 \iint_S u_i\delta u_i dS + \iint_S \left(p_i\delta u_i + \sigma_0\delta\varphi + B_0\delta\xi\right)dS = 0\,, \tag{2}$$

where $\delta\tilde{H} = \sigma_{ij}\delta\varepsilon_{ij} - D_i\delta E_i - B_i\delta H_i$.

To construct an applied theory of vibrations, we will accept Kirchhoff's hypotheses. In accordance with them, the distribution of displacements along the thickness has the form:

$$u_1(x_1, x_3) = -x_3 w_{,1},\ u_3(x_1, x_3) = w(x_1) \tag{3}$$

In particular, the single normal hypothesis is accepted for a mechanical field. Next, we consider a problem in which the value of the electric potential on the electrodes can be zero, so its distribution is not described by a linear function. Taking into account the possible inhomogeneity in the length of the element associated with the influence of boundary conditions at the ends of the bimorph, its thickness distribution is assumed to be quadratic:

$$\varphi(x_1, \tilde{x}_3) = V_0(x_1)\frac{\tilde{x}_3}{H}\left(\frac{2\tilde{x}_3}{H} - 1\right) + V_1(x_1)\left(1 - \frac{4\tilde{x}_3^2}{H^2}\right) + V_2(x_1)\frac{\tilde{x}_3}{H}\left(\frac{2\tilde{x}_3}{H} + 1\right). \tag{4}$$

Here, $\tilde{x}_3 = x_3 - h/2$. Functions V_0, V_1 and V_2 are responsible for the value of the electric potential at the inner electrode, in the middle of the layer, and at the outer electrode, respectively. To satisfy the conditions of the problem, we take these functions in the following form (see Fig. 2):

$$V_0(x_1) = V_0 = const,\ V_1(x_1) = \Phi(x_1),\ V_2(x_1) = V_2 = const.$$

Here, function $\Phi(x_1)$ is unknown.

We represent a quadratic distribution of the magnetic potential over the thickness of each layer. The distribution along the length is heterogeneous, at the inner boundary of the layers, its value is assumed to be zero:

$$\xi(x_1, \tilde{x}_3) = M_0(x_1)\frac{\tilde{x}_3}{H}\left(\frac{2\tilde{x}_3}{H} - 1\right) + M_1(x_1)\left(1 - \frac{4\tilde{x}_3^2}{H^2}\right) + M_2(x_1)\frac{\tilde{x}_3}{H}\left(\frac{2\tilde{x}_3}{H} + 1\right). \tag{5}$$

Here, $\tilde{x}_3 = x_3 - h/2$. Functions M_0, M_1 and M_2 are responsible for the value of the magnetic potential at the inner boundary, in the middle of the layer, and at the outer boundary, respectively, and are taken as follows (Fig. 2):

$$M_0(x_1) = M_0 = const, \quad M_1(x_1) = \Xi_2(x_1), \quad M_2(x_1) = \Xi_3(x_1).$$

Here, functions $\Xi_2(x_1)$ and $\Xi_3(x_1)$ are unknown.

We substitute relations (3)–(5) into equation (2) and integrate it by the bimorph thickness, and then we equate the coefficients with independent variations δw, $\delta\Phi$, $\delta\Xi_2$ and $\delta\Xi_3$ to zero. Thus, we obtain a system of four differential equations (6) from four unknown functions depending on x_1 (then, we omit the subscript), and five boundary conditions (7).

$$\begin{gathered}
\frac{16\tilde{\epsilon}_{33}}{3H}V_0 + \frac{16\tilde{\epsilon}_{33}}{3H}V_2 - \frac{32\tilde{\epsilon}_{33}}{3H}\Phi(x) - \frac{32\tilde{\alpha}_{33}}{3H}\Xi_2(x) + \frac{16\tilde{\alpha}_{33}}{3H}\Xi_3(x) - \frac{16\epsilon_{11}H}{15}\frac{d^2}{dx^2}\Phi(x) - \\
-\frac{16\alpha_{11}H}{15}\frac{d^2}{dx^2}\Xi_2(x) - \frac{2\alpha_{11}H}{15}\frac{d^2}{dx^2}\Xi_3(x) - \frac{4\tilde{e}_{31}H}{3}\frac{d^2}{dx^2}w(x) + \frac{16\tilde{\alpha}_{33}}{3H}M_0 = 0, \\
\frac{16\tilde{\alpha}_{33}}{3H}V_0 + \frac{16\tilde{\alpha}_{33}}{3H}V_2 - \frac{32\tilde{\alpha}_{33}}{3H}\Phi(x) - \frac{32\tilde{\mu}_{33}}{3H}\Xi_2(x) + \frac{16\tilde{\mu}_{33}}{3H}\Xi_3(x) - \frac{16\alpha_{11}H}{15}\frac{d^2}{dx^2}\Phi(x) - \\
-\frac{16\mu_{11}H}{15}\frac{d^2}{dx^2}\Xi_2(x) - \frac{2\mu_{11}H}{15}\frac{d^2}{dx^2}\Xi_3(x) - \frac{4\tilde{h}_{31}H}{3}\frac{d^2}{dx^2}w(x) + \frac{16\tilde{\mu}_{33}}{3H}M_0 = 0, \\
-\frac{2\tilde{\alpha}_{33}}{3H}V_0 - \frac{14\tilde{\alpha}_{33}}{3H}V_2 + \frac{16\tilde{\alpha}_{33}}{3H}\Phi(x) + \frac{16\tilde{\mu}_{33}}{3H}\Xi_2(x) - \frac{14\tilde{\mu}_{33}}{3H}\Xi_3(x) - \frac{2\alpha_{11}H}{15}\frac{d^2}{dx^2}\Phi(x) - \\
-\frac{2\mu_{11}H}{15}\frac{d^2}{dx^2}\Xi_2(x) - \frac{4\mu_{11}H}{15}\frac{d^2}{dx^2}\Xi_3(x) + \frac{5\tilde{h}_{31}H}{3}\frac{d^2}{dx^2}w(x) - 2B_0 - \frac{2\tilde{\mu}_{33}}{3H}M_0 = 0, \\
\frac{4\tilde{e}_{31}H}{3}\frac{d^2}{dx^2}\Phi(x) + \frac{4\tilde{h}_{31}H}{3}\frac{d^2}{dx^2}\Xi_2(x) - \frac{5\tilde{h}_{31}H}{3}\frac{d^2}{dx^2}\Xi_3(x) - 2p_3H - \\
-\frac{2\rho\omega^2H^3}{3}\frac{d^2}{dx^2}w(x) + 2\omega^2\rho w(x)H + \frac{2H^3\tilde{c}_{11}}{3}\frac{d^4}{dx^4}w(x) = 0.
\end{gathered} \tag{6}$$

$$\begin{gathered}
\frac{16\epsilon_{11}H}{15}\frac{d}{dx}\Phi(x) + \frac{16\alpha_{11}H}{15}\frac{d}{dx}\Xi_2(x) + \frac{2\alpha_{11}H}{15}\frac{d}{dx}\Xi_3(x) = 0, \\
\frac{16\alpha_{11}H}{15}\frac{d}{dx}\Phi(x) + \frac{16\mu_{11}H}{15}\frac{d}{dx}\Xi_2(x) + \frac{2\mu_{11}H}{15}\frac{d}{dx}\Xi_3(x) = 0, \\
\frac{2\alpha_{11}H}{15}\frac{d}{dx}\Phi(x) + \frac{2\mu_{11}H}{15}\frac{d}{dx}\Xi_2(x) + \frac{4\mu_{11}H}{15}\frac{d}{dx}\Xi_3(x) = 0, \\
\frac{\tilde{e}_{31}H}{3}V_0 - \frac{5\tilde{e}_{31}H}{3}V_2 + \frac{4\tilde{e}_{31}H}{3}\Phi(x) + \frac{4\tilde{h}_{31}H}{3}\Xi_2(x) - \frac{5\tilde{h}_{31}H}{3}\Xi_3(x) + \frac{2H^3\tilde{c}_{11}}{3}\frac{d^2}{dx^2}w(x) + \frac{\tilde{h}_{31}H}{3}M_0 = 0, \\
-\frac{4\tilde{e}_{31}}{3}\frac{d}{dx}\Phi(x) - \frac{4\tilde{h}_{31}H}{3}\frac{d}{dx}\Xi_2(x) + \frac{5\tilde{h}_{31}H}{3}\frac{d}{dx}\Xi_3(x) - \frac{2H^3\tilde{c}_{11}}{3}\frac{d^3}{dx^3}w(x) + \frac{2\rho\omega^2H^3}{3}\frac{d}{dx}w(x) = 0.
\end{gathered} \tag{7}$$

Here, the following designations were introduced: $\tilde{c}_{11} = c_{11} - c_{13}^2/c_{33}$, $\tilde{e}_{31} = e_{31} - c_{13}e_{33}/c_{33}$, $\tilde{h}_{31} = h_{31} - c_{13}h_{33}/c_{33}$, $\tilde{\alpha}_{33} = -\alpha_{33} - e_{33}h_{33}/c_{33}$, $\tilde{\epsilon}_{33} = -\epsilon_{33} - {e_{33}}^2/c_{33}$. They occurred after satisfying condition $\sigma_{33} = 0$ and exclusion of ε_{33}.

Research Results. The results of the bimorph calculation according to the proposed theory are compared to the finite element calculation in the low-frequency region for the volume ratio of the piezoelectric and piezomagnetic components 80 % $BaTiO_3$ and 20 % $CoFe_2O_4$. The comparison has shown that the error in finding the characteristics of the mechanical and magnetic fields is less than 1%. When determining the electric field in the middle part of the plate, the difference was about 5%. Describing the situation in the vicinity of the support points, it should be noted that the size of the neighborhood along the longitudinal coordinate is approximately equal to the bimorph thickness. Here, when determining the electric field, a difference of 20% is recorded.

The first step in studying the vibrations of a two-layer piezomagnetoelectric bimorph with a change in the volume ratio of $BaTiO_3$ and $CoFe_2O_4$ in the composite is to determine its effective properties. Tables 1 and 2 present these properties found from the results of study [8].

Table 1

Material constants (elastic modules, dielectric and magnetic permittivity) for different $BaTiO_3$ volume fraction

Volume fraction $BaTiO_3$ (%)	Elastic modules GPa					Dielectric permittivity 10^{-9} f/m		Magnetic permittivity 10^{-4} N s²/C²	
	c_{11}	c_{12}	c_{13}	c_{33}	c_{44}	κ_{11}	κ_{33}	μ_{11}	μ_{33}
0	286.0	173.0	170.0	269.5	45.30	0.080	0.093	5.900	1.570
10	270.9	160.4	154.9	260.0	45.07	1.469	0.073	5.315	0.632
20	256.6	148.5	142.6	250.2	44.84	2.815	0.098	4.730	0.396
30	242.8	137.2	131.3	240.8	44.61	4.063	0.122	4.145	0.285
40	229.9	126.8	120.9	231.9	44.38	5.287	0.147	3.560	0.223
50	217.6	116.9	111.0	224.0	44.15	6.413	0.171	2.975	0.186
60	206.7	108.1	102.1	215.6	43.92	7.490	0.220	2.390	0.155
70	195.9	99.7	93.8	208.2	43.69	8.517	0.294	1.805	0.136
80	186.0	92.3	85.9	201.3	43.46	9.448	0.441	1.220	0.120
90	176.6	85.4	78.9	193.9	43.23	10.353	0.857	0.635	0.110
100	166.0	77.0	78.0	162.0	43.00	11.200	12.600	0.050	0.100

Table 2

Material constants (piezoelectric, piezomagnetic and magnetoelectric modules) for different $BaTiO_3$ volume fraction

Volume fraction $BaTiO_3$ (%)	Piezoelectric modules C/m²			Piezomagnetic modules N/A m			Magnetoelectric modules 10^{-8} Ns/VC	10^{-11} Ns/VC
	e_{31}	e_{33}	e_{15}	h_{31}	h_{33}	h_{15}	α_{11}	α_{33}
0	0	0	0	580.3	–699.7	550	0	0
10	–0.006	0.029	1.16	223.6	–244.1	495	–1.33	1.97
20	–0.013	0.059	2.32	130.0	–132.3	440	–2.35	2.36
30	–0.019	0.088	3.48	86.7	–79.8	385	–3.07	2.48
40	–0.025	0.132	4.64	61.6	–52.5	330	–3.48	2.50
50	–0.031	0.176	5.80	43.3	–34.2	275	–3.62	2.47
60	–0.038	0.220	6.96	29.7	–22.8	220	–3.45	2.43
70	–0.040	0.352	8.12	20.5	–13.7	165	–3.00	2.36
80	–0.060	0.571	9.28	13.7	–9.1	110	–2.27	2.29
90	–0.263	1.187	10.44	4.6	–4.6	55	–1.28	2.16
100	–4.400	18.600	11.60	0	0	0	0	0

The bimorph vibrations were excited by a magnetic flux applied to the upper and lower faces (Fig. 2), which varied according to the harmonic law with an amplitude of $B_0 = 5\times10^{-5}$ Wb and a frequency of 10 kHz.

Figure 3 shows the deflection in the middle of the layer depending on volume fraction of $BaTiO_3$. It can be seen from the graph that the deflection in the position having coordinates $x_1 = L/2$, $x_3 = H/2$, is zero if the bimorph consists only of a piezoelectric $BaTiO_3$. The deflection of the bimorph reaches the greatest value if it contains only piezoelectric magnet $CoFe_2O_4$. The deflection almost linearly depends on the volume ratio of the components of piezoactive materials.

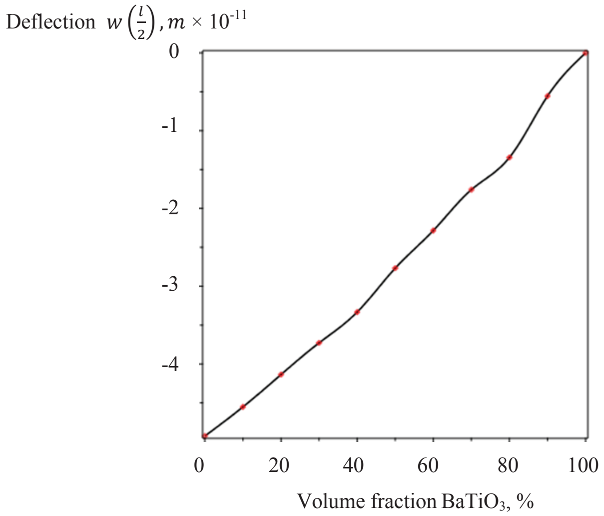

Fig. 3. Deflection $w(x_1)$ in the middle of the layer for different $BaTiO_3$ volume fraction

Based on the data in Figure 4, it can be concluded that the electric potential in the middle of the layer varies nonlinearly with a change in the volume ratio of the composition of bimorph piezoactive materials. If the bimorph consists only of $BaTiO_3$ or $CoFe_2O_4$, then the electric potential at the point $(L/2, H/2)$ is zero and reaches the highest value at 35 % $BaTiO_3$ in the bimorph.

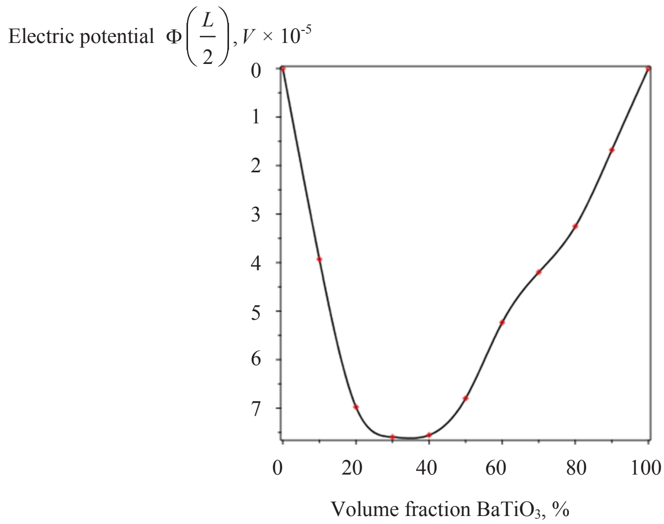

Fig. 4. Electric potential $\Psi(x_1)$ for different $BaTiO_3$ volume fraction

The analysis of Figures 5 and 6 allows us to conclude that the magnetic potential in the middle of the layer $\Xi_2(L/2)$ and at the outer boundary $\Xi_3(L/2)$ increases almost linearly with an increase in the volume of $BaTiO_3$ in the bimorph.

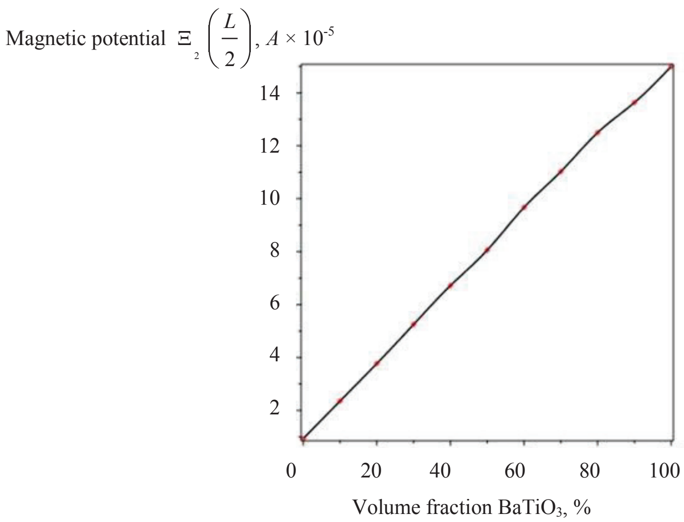

Fig. 5. Magnetic potential $\Xi_2(L/2)$ for different $BaTiO_3$ volume fraction

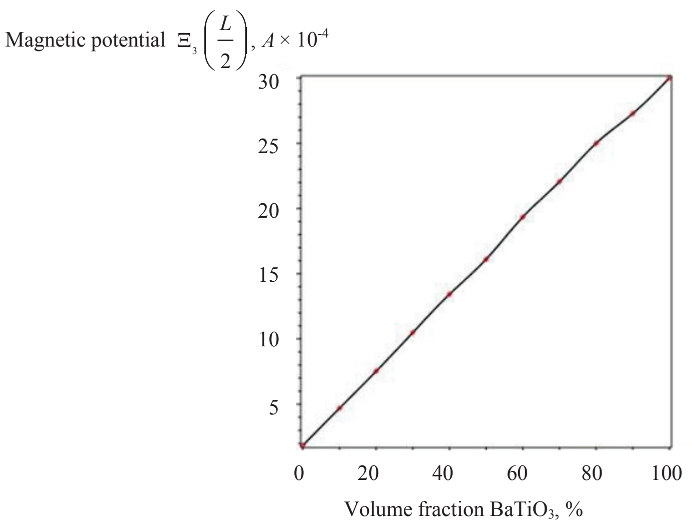

Fig. 6. Magnetic potential $\Xi_3(L/2)$ for different $BaTiO_3$ volume fraction

Discussion and Conclusions. An applied theory is proposed for calculating transverse vibrations of a bimorph made of two layers of a composite based on $CoFe_2O_4$ and $BaTiO_3$ with both piezoelectric and piezomagnetic properties, in an alternating magnetic field. Such a design can serve as a model of a piezoelectric generator of a device for collecting and storing energy under the action of an external magnetic field. In the low-frequency region (below the natural frequency of the first bending mode), calculations of the stress-strain state of the bimorph, the distribution of electric and magnetic fields, are carried out. The dependence of the deflection, electric and magnetic potentials on the volume ratio of the bimorph composition is investigated. In further work, it is assumed to determine the output potential and power of an electric current excited by an alternating magnetic field. The purpose of these surveys will be to collect electrical energy.

References

1. Paolo Gaudenzi. Smart structures: physical behavior, mathematical modeling and applications. New York: John Wiley & Sons; 2009. 194 p. https://doi.org/10.1002/9780470682401

2. Qader IN, Kok M, Dagdelen F, et al. A review of smart materials: Researches and applications. El-Cezeri Journal of Science and Engineering. 2019;6:755–788. https://doi.org/10.31202/ecjse.562177

3. Amrillah T, Hermawan A, Wulandari CP, et al. Crafting the multiferroic $BiFeO_3$-$CoFe_2O_4$ nanocomposite for next-generation devices: A review. Materials and Manufacturing Processes. 2021;36:1579–1596. https://doi.org/10.1080/10426914.2021.1945096

4. Abraime B, Mahmoud A, Boschini F, et al. Tunable maximum energy product in $CoFe_2O_4$ nanopowder for permanent magnet application. Journal of Magnetism and Magnetic Materials. 2018;467:129–134. https://doi.org/10.1016/j.jmmm.2018.07.063

5. Lamouri R, Mounkachi O, Salmani E, et al. Size effect on the magnetic properties of $CoFe_2O_4$ nanoparticles: a Monte Carlo study. Ceramics International. 2020;46:8092–8096. https://doi.org/10.1016/j.ceramint.2019.12.035

6. Jin-Yeon Kim. Micromechanical analysis of effective properties of magneto-electro-thermo-elastic multilayer composites. International Journal of Engineering Science. 2011;49:1001–1018. https://doi.org/10.1016/j.ijengsci.2011.05.012

7. Siva KV, Kaviraj P, Arockiarajan A. Improved room temperature magnetoelectric response in $CoFe_2O_4$-$BaTiO_3$ core shell and bipolar magnetostrictive properties in $CoFe_2O_4$. Materials Letters. 2020;268:127623. https://doi.org/10.1016/j.matlet.2020.127623

8. Challagulla KS, Georgiades AV. Micromechanical analysis of magneto-electro-thermo-elastic composite materials with applications to multilayered structures. International Journal of Engineering Science. 2011;49:85–104. https://doi.org/10.1016/j.ijengsci.2010.06.025

9. Novatskii V, Shachnev VA. Ehlektromagnitnye ehffekty v tverdykh telakh. Moscow: Mir; 1986. 160 p. (In Russ.)

10. Parton VZ, Kudryavtsev BA. Ehlektromagnitouprugost' p'ezoehlektricheskikh i ehlektroprovodnykh tel. Moscow: Nauka; 1988. 472 p. (In Russ.)

11. Bagdasaryan GE, Danoyan ZN. Ehlektromagnitouprugie volny. Yerevan: Yerevan State University Publ. House; 2006. 492 p. (In Russ.)

12. Vatul'yan AO, Rynkova AA. Flexural vibrations of a piezoelectric bimorph with a cut internal electrode. Journal of Applied Mechanics and Technical Physics. 200;42:164–168. https://doi.org/10.1023/A:1018837401827

13. Levi MO, Kalinchuk VV. Some features of the dynamics of electro-magneto-elastic half-space with initial deformations. In: Proc. 2017 Dynamics of Systems, Mechanisms and Machines (Dynamics), IEEE. 2017. P. 262–266. https://doi.org/10.1109/Dynamics.2017.8239478

14. Levi MO, Andzhikovich IE, Vorovich EI, et al. The influence of boundary conditions on the dynamics of semibounded electromagneto-elasticity media. Vestnik SSC RAS. 2012;8:14–19.

15. Soloviev AN, Chebanenko VA, Parinov IA, et al. Applied theory of bending vibrations of a piezoelectric bimorph with a quadratic electric potential distribution. Materials Physics and Mechanics. 2019;42:65–73. https://doi.org/10.18720/MPM.4212019_7

16. Soloviev AN, Chebanenko VA, Parinov IA, et al. Study of oscillation of a bimorph plate taking into account the nonlinearity of the elastic potential. Science in the South of Russia. 2019;15:3–11. https://doi.org/10.7868/S25000640190301

17. Do Thanh Binh, Chebanenko VA, Le Van Duong, et al. Applied theory of bending vibration of the piezoelectric and piezomagnetic bimorph. Journal of Advanced Dielectrics. 2020;10:2050007. https://doi.org/10.1142/S2010135X20500071

18. Kurbatova NV, Nadolin DK, Nasedkin AV, et al. Finite element approach for composite magneto-piezoelectric materials modeling in ACELAN-COMPOS package. In book: Analysis and Modelling of Advanced Structures and Smart Systems. 2018;81:69–88. https://doi.org/10.1007/978-981-10-6895-9_5

Received 23.12.2021

Revised 20.01.2022

Accepted 24.01.2022

About the Authors

Soloviev, Arkadiy N., Head of the Theoretical and Applied Mechanics Department, Don State Technical University (1, Gagarin sq., Rostov-on-Don, 344003, RF), Dr.Sci. (Phys.-Math.), professor, ResearcherID, ScopusID, ORCID, solovievarc@gmail.com.

Do Thanh Binh, postgraduate student of the Theoretical and Applied Mechanics Department, Don State Technical University (1, Gagarin sq., Rostov-on-Don, 344003, RF), ResearcherID, ScopusID, ORCID, dothanhbinh@mail.ru.

Chebanenko, Valerii A., Senior Research Scholar, Federal Research Centre the Southern Scientific Centre of the Russian Academy of Sciences (41, Chekhov St., Rostov-on-Don, 344010, RF), Cand.Sci. (Phys.-Math.), senior research scholar, ResearcherID, ScopusID, ORCID, valera.chebanenko@yandex.ru.

Lesnyak, Olga N., associate professor of the Theoretical and Applied Mechanics Department, Don State Technical University (1, Gagarin sq., Rostov-on-Don, 344003, RF), ORCID, lesniak.olga@yandex.ru

Kirillova, Evgeniya V., Rhein-Main University of Applied Sciences (Wiesbaden, Germany (18, Kurt-Schumacher-Ring, Wiesbaden 65197, Germany), Cand.Sci. (Phys.-Math.), professor, ScopusID, ORCID, Evgenia.Kirillova@hs-rm.de

Claimed contributorship

A. N. Soloviev: academic advising; task formulation; analysis of the research results. Do Thanh Binh: derivation of equations; calculation program development; computational analysis; analysis of the research results; text preparation. V. A. Chebanenko: selection of research method; variational formulation of the problem; analysis of the research results. O. N. Lesnyak: text preparation; discussion of the results. E. V. Kirillova: analysis of the research results.

All authors have read and approved the final manuscript.

MECHANICS

UDC 539.47
https://doi.org/10.23947/2687-1653-2022-22-1-14-23

Original article

Analysis of the stress-strain state of a radially inhomogeneous transversely isotropic sphere with a fixed side surface

Natiq K. Akhmedov[1] ✉, **Sevinj M. Yusubova**[2]
[1]Azerbaijan State University of Economics (UNEC) (Baku, Azerbaijan)
[2]G. Aliyev Lyceum (Baku, Azerbaijan)
✉ anatiq@gmail.com

Introduction. The paper considers an axisymmetric problem of elasticity theory for a radially inhomogeneous transversally isotopic nonclosed sphere containing none of the 0 and π poles. It is believed that the elastic moduli are linear functions of the radius of the sphere. It is assumed that the side surface of the sphere is fixed, and arbitrary stresses are given on the conic sections, leaving the sphere in equilibrium. The work objective is an asymptotic analysis of the problem of elasticity theory for a radially inhomogeneous transversally isotropic sphere of small thickness, and a study of a three-dimensional stress-strain state based on this analysis.
Materials and Methods. The three-dimensional stress-strain state is investigated on the basis of the equations of elasticity theory by the method of homogeneous solutions and asymptotic analysis.
Research Results. After the homogeneous boundary conditions set on the side surfaces of the sphere are met, a characteristic equation is obtained, and its roots are classified with respect to a small parameter characterizing the thickness of the sphere. The corresponding asymptotic solutions depending on the roots of the characteristic equation are constructed. It is shown that the solutions corresponding to a countable set of roots have the character of a boundary layer localized in conic slices. The branching of the roots generates new solutions that are characteristic only for a transversally isotropic radially inhomogeneous sphere. A weakly damping boundary layer solution appears, which can penetrate deep away from the conical sections and change the picture of the stress-strain state.
Discussion and Conclusions. Based on the solutions constructed, it is possible to determine the applicability areas of existing applied theories and propose a new more refined applied theory for a radially inhomogeneous transversally isotropic spherical shell.

Keywords*:* equilibrium equations, Legendre equations, radially inhomogeneous sphere, characteristic equation, boundary layer solutions, variational principle, applied theory, reduction method.

For citation: Akhmedov N. K., Yusubova S. M. Analysis of the stress-strain state of a radially inhomogeneous transversely isotropic sphere with a fixed side surface. Advanced Engineering Research, 2022, vol. 22, no. 1, pp. 14–23. (In Russ). https://doi.org/10.23947/2687-1653-2022-22-1-14-23

Introduction. One of the properties of materials affecting the stress-strain state of elastic bodies is their heterogeneity. Investigating the stress-strain state of inhomogeneous bodies based on three-dimensional equations of elasticity theory is associated with significant mathematical difficulties.

A number of studies are devoted to the investigation of three-dimensional problems of elasticity theory for the sphere.

In [1], based on the equations of elasticity theory for the sphere, a general solution satisfying the boundary conditions on the contour in the sense of Saint-Venant was obtained, the stress-strain state of the sphere was analyzed. In [2], based on the equations of elasticity theory for a thick isotropic sphere, homogeneous solutions depending on the roots of the transcendental equation are constructed. In [3], on the basis of solving three-dimensional problems of elasticity theory for a sphere of small thickness, the accuracy of existing applied theories is studied, and a method for constructing refined applied theories is given. A three-dimensional asymptotic theory of a transversally isotropic spherical shell of small thickness is presented in [4]. An analysis of the three-dimensional stress-strain state of a three-layer sphere with a soft filler is described in [5]. In [6], the torsion problem is studied by the method of homogeneous solutions for a radially inhomogeneous transversally isotropic sphere of small thickness, when the elastic characteristics are changed by linear, quadratic and inversely quadratic laws along the radius. In [7], the torsion problem for a radially layered sphere with an arbitrary number of alternating hard and soft layers is studied. The existence of weakly damping boundary-layer solutions and a possible violation of the Saint-Venant principle in its classical formulation are shown. An applied theory of torsion of a radially layered sphere is constructed, which adequately takes into account the emerging features. In [8], the problem of elasticity theory for a radially inhomogeneous hollow ball is investigated using the finite element method and spline collocation. In [8], using the finite element method and spline collocation, the problem of elasticity theory for a radially inhomogeneous hollow ball is studied. The results obtained by finite element methods and spline collocation are compared. The axisymmetric problem of the theory of elasticity for a radially inhomogeneous transversally isotropic sphere of small thickness is studied by the method of asymptotic integration of the equations of the theory of elasticity in [9]. Inhomogeneous and homogeneous solutions are constructed. The nature of the stress-strain state is established. In [10], an axisymmetric problem of elasticity theory for a sphere of small thickness with variable elasticity moduli is considered by the method of homogeneous solutions. Asymptotic formulas for displacements and stresses are obtained, which provides calculating the three-dimensional stress-strain state of a radially inhomogeneous sphere.

Materials and Methods. Deformation is considered within the framework of the linear theory of elasticity of a nonclosed sphere, whose material is transversely isotropic and inhomogeneous along the radial coordinate. The thickness of the hollow sphere is assumed to be small compared to the radius and size along the arc coordinate. Boundary conditions are considered that provide solving the problem in an axisymmetric formulation. We assume that the sphere does not contain any of the poles 0 and π. In the spherical coordinate system, the area occupied by the sphere will be denoted by $\Gamma=\{r\in[r_1;\, r_2],\quad \theta\in[\theta_1;\, \theta_2],\ \phi\in[0;\, 2\pi]\}$.

The linear dependence of the elastic properties of the material along the radius is considered:

$$A_{11}=a_{11}^{(0)}r,\quad A_{12}=a_{12}^{(0)}r,\quad A_{22}=a_{22}^{(0)}r,\quad A_{23}=a_{23}^{(0)}r,\quad A_{44}=a_{44}^{(0)}r, \tag{1}$$

where $a_{11}^{(0)},a_{12}^{(0)},a_{22}^{(0)},a_{23}^{(0)},a_{44}^{(0)}$ — some constants.

The system of equilibrium equations in the absence of body forces in a spherical coordinate system r,θ,ϕ has the form [11]:

$$\frac{\partial\sigma_{rr}}{\partial r}+\frac{1}{r}\frac{\partial\sigma_{r\theta}}{\partial\theta}+\frac{2\sigma_{rr}-\sigma_{\phi\phi}-\sigma_{\theta\theta}+\sigma_{r\theta}ctg\theta}{r}=0, \tag{2}$$

$$\frac{\partial\sigma_{r\theta}}{\partial r}+\frac{1}{r}\frac{\partial\sigma_{\theta\theta}}{\partial\theta}+\frac{3\sigma_{r\theta}+(\sigma_{\theta\theta}-\sigma_{\phi\phi})ctg\theta}{r}=0, \tag{3}$$

where, $\sigma_{rr},\sigma_{r\theta},\sigma_{\phi\phi},\sigma_{\theta\theta}$ — stress tensor components, which are expressed in terms of displacement vector components $\upsilon_r=\upsilon_r(r,\theta),\ \upsilon_\theta=\upsilon_\theta(r,\theta)$ as follows [4]:

$$\sigma_{rr}=A_{11}\frac{\partial\upsilon_r}{\partial r}+\frac{A_{12}}{r}\left(\upsilon_\theta ctg\theta+2\upsilon_r+\frac{\partial\upsilon_\theta}{\partial\theta}\right), \tag{5}$$

$$\sigma_{\phi\phi}=A_{12}\frac{\partial\upsilon_r}{\partial r}+\frac{1}{r}\left[\left(A_{22}+A_{23}\right)\upsilon_r+A_{22}\upsilon_\theta ctg\theta+A_{23}\frac{\partial\upsilon_\theta}{\partial\theta}\right], \tag{6}$$

$$\sigma_{\theta\theta}=A_{12}\frac{\partial\upsilon_r}{\partial r}+\frac{1}{r}\left[(A_{22}+A_{23})\upsilon_r+A_{23}\upsilon_\theta ctg\theta+A_{22}\frac{\partial\upsilon_\theta}{\partial\theta}\right], \tag{7}$$

$$\sigma_{r\theta}=A_{44}\left(\frac{\partial\upsilon_\theta}{\partial r}-\frac{\upsilon_\theta}{r}+\frac{1}{r}\frac{\partial\upsilon_r}{\partial\theta}\right). \tag{8}$$

Substituting (5)–(8) into (2)–(3), taking into account (1), we obtain the equations of equilibrium in displacements.

$$\begin{cases} b_{11}^{(0)}\left(\dfrac{\partial^2 u_\rho}{\partial\rho^2}+2\varepsilon\dfrac{\partial u_\rho}{\partial\rho}\right)+2\left(2b_{12}^{(0)}-b_{22}^{(0)}-b_{23}^{(0)}\right)\varepsilon^2 u_\rho+\left(2b_{12}^{(0)}-b_{23}^{(0)}-b_{22}^{(0)}-b_{44}^{(0)}\right)\times \\ \times\varepsilon^2\left(\dfrac{\partial u_\theta}{\partial\theta}+u_\theta ctg\theta\right)+\varepsilon\left(b_{44}^{(0)}+b_{12}^{(0)}\right)\left(\dfrac{\partial u_\theta}{\partial\rho}ctg\theta+\dfrac{\partial^2 u_\theta}{\partial\theta\partial\rho}\right)+\varepsilon^2 b_{44}^{(0)}\left(\dfrac{\partial^2 u_\rho}{\partial\theta^2}+\dfrac{\partial u_\rho}{\partial\theta}ctg\theta\right)=0, \quad (9) \\ b_{44}^{(0)}\left(\dfrac{\partial^2 u_\theta}{\partial\rho^2}+2\varepsilon\dfrac{\partial u_\theta}{\partial\rho}-3\varepsilon^2 u_\theta+\varepsilon\dfrac{\partial^2 u_\rho}{\partial\rho\partial\theta}\right)+\left(3b_{44}^{(0)}+b_{22}^{(0)}+b_{23}^{(0)}\right)\varepsilon^2\dfrac{\partial u_\rho}{\partial\theta}+ \\ +\varepsilon^2 b_{22}^{(0)}\left(\dfrac{\partial u_\theta}{\partial\theta}ctg\theta+\dfrac{\partial^2 u_\theta}{\partial\theta^2}\right)+\varepsilon b_{12}^{(0)}\dfrac{\partial^2 u_\rho}{\partial\rho\partial\theta}-\varepsilon^2\left(b_{22}^{(0)}ctg^2\theta+b_{23}^{(0)}\right)u_\theta=0. \quad (10) \end{cases}$$

Here, $\rho=\dfrac{1}{\varepsilon}\ln\left(\dfrac{r}{r_0}\right)$ — new dimensionless variable; $\varepsilon=\dfrac{1}{2}\ln\left(\dfrac{r_2}{r_1}\right)$ — a small parameter characterizing the thickness of the sphere; $r_0=\sqrt{r_1 r_2}$; $\rho\in[-1;1]$; $u_\rho=\dfrac{\upsilon_r}{r_0}$, $u_\theta=\dfrac{\upsilon_\theta}{r_0}$, $b_{ij}^{(0)}=\dfrac{a_{ij}^{(0)}r_0}{G_0}$ — dimensionless quantities; G_0 — some parameter having the dimension of the elasticity modulus.

We assume that the lateral part of the sphere boundary is fixed, i.e.,

$$u_\rho\big|_{\rho=\pm1}=0, \tag{11}$$

$$u_\theta\big|_{\rho=\pm1}=0. \tag{12}$$

We assume that at the ends of the sphere (on the conical sections), the stresses are specified

$$\sigma_{\theta\theta}\big|_{\theta=\theta_s}=f_{1s}(\rho), \qquad \sigma_{\rho\theta}\big|_{\theta=\theta_s}=f_{2s}(\rho). \tag{13}$$

Here, $f_{1s}(\rho)$, $f_{2s}(\rho)$ $(s=1;2)$ — sufficiently smooth functions that satisfy the equilibrium conditions.

Solutions (9), (10) are sought in the form [3, 4]:

$$u_\rho(\rho,\theta)=a(\rho)m(\theta); \quad u_\theta(\rho,\theta)=d(\rho)m'(\theta), \tag{14}$$

Where function $m(\theta)$ satisfies the Legendre equation:

$$m''(\theta)+ctg\theta\cdot m'(\theta)+\left(z^2-\frac{1}{4}\right)m(\theta)=0. \tag{15}$$

After substituting (14) into (9), (10), (11), (12), taking into account (15), we obtain:

$$\begin{gathered} b_{11}^{(0)}a''(\rho)+2\varepsilon b_{11}^{(0)}a'(\rho)+\varepsilon^2\left[\left(4b_{12}^{(0)}-2b_{22}^{(0)}-2b_{23}^{(0)}\right)-\left(z^2-\frac{1}{4}\right)b_{44}^{(0)}\right]a(\rho)- \\ -\left(z^2-\frac{1}{4}\right)\varepsilon\left[\left(b_{44}^{(0)}+b_{12}^{(0)}\right)d'(\rho)-\varepsilon\left(b_{44}^{(0)}+b_{22}^{(0)}+b_{23}^{(0)}-2b_{12}^{(0)}\right)d(\rho)\right]=0, \end{gathered} \tag{16}$$

$$\begin{gathered} b_{44}^{(0)}\left(d''(\rho)+2\varepsilon d'(\rho)\right)-\varepsilon^2\left[\left(z^2-\frac{1}{4}\right)b_{22}^{(0)}+\left(b_{23}^{(0)}-b_{22}^{(0)}+3b_{44}^{(0)}\right)\right]d(\rho)+ \\ +\varepsilon^2\left(3b_{44}^{(0)}+b_{22}^{(0)}+b_{23}^{(0)}\right)a(\rho)+\varepsilon\left(b_{44}^{(0)}+b_{12}^{(0)}\right)a'(\rho)=0, \end{gathered} \tag{17}$$

$$a(\rho)=0, \text{ при } \rho=\pm1. \tag{18}$$

$$d(\rho)=0, \text{ при } \rho=\pm1. \tag{19}$$

The solution to system (16), (17) has the form:

$$a(\rho)=e^{-\varepsilon\rho}\left[p_1e^{\varepsilon s_1\rho}C_1+p_1e^{-\varepsilon s_1\rho}C_2+p_2e^{\varepsilon s_2\rho}C_3+p_2e^{-\varepsilon s_2\rho}C_4\right], \tag{20}$$

$$d(\rho)=e^{-\varepsilon\rho}\left[t_1e^{\varepsilon s_1\rho}C_1+q_1e^{-\varepsilon s_1\rho}C_2+t_2e^{\varepsilon s_2\rho}C_3+q_2e^{-\varepsilon s_2\rho}C_4\right], \tag{21}$$

where C_n $(n=\overline{1,4})$ — arbitrary constants,

$$p_k=b_{44}^{(0)}s_k^2-\left(z^2-\frac{1}{4}\right)b_{22}^{(0)}+\left(b_{22}^{(0)}-b_{23}^{(0)}-4b_{44}^{(0)}\right);$$

$$t_k=-\left(b_{44}^{(0)}+b_{12}^{(0)}\right)s_k-\left(2b_{44}^{(0)}+b_{22}^{(0)}+b_{23}^{(0)}-b_{12}^{(0)}\right);$$

$q_k = \left(b_{44}^{(0)} + b_{12}^{(0)}\right)s_k - \left(2b_{44}^{(0)} + b_{22}^{(0)} + b_{23}^{(0)} - b_{12}^{(0)}\right)$; s_k — equation roots

$$\begin{gathered} b_{11}^{(0)}b_{44}^{(0)}s^4 + \left[\left(z^2-\frac{1}{4}\right)\left((b_{12}^{(0)})^2 + 2b_{44}^{(0)}b_{12}^{(0)} - b_{11}^{(0)}b_{22}^{(0)}\right) + b_{11}^{(0)}b_{22}^{(0)} - 5b_{11}^{(0)}b_{44}^{(0)} + 4b_{12}^{(0)}b_{44}^{(0)} - \right. \\ \left. -2b_{22}^{(0)}b_{44}^{(0)} - b_{11}^{(0)}b_{23}^{(0)} - 2b_{23}^{(0)}b_{44}^{(0)}\right]s^2 + \left[\left(z^2-\frac{1}{4}\right)b_{44}^{(0)} - 4b_{12}^{(0)} + 2b_{22}^{(0)} + 2b_{23}^{(0)} + b_{11}^{(0)}\right]\times \\ \times\left[\left(z^2-\frac{1}{4}\right)b_{22}^{(0)} + b_{23}^{(0)} - b_{22}^{(0)} + 4b_{44}^{(0)}\right] - \left(z^2-\frac{1}{4}\right)\left(2b_{44}^{(0)} + b_{22}^{(0)} + b_{23}^{(0)} - b_{12}^{(0)}\right)^2 = 0. \end{gathered} \tag{22}$$

The system of linear algebraic equations with respect to C_1, C_2, C_3, C_4, is obtained through satisfying the homogeneous boundary conditions (18), (19). The zero equality of the determinant of this system is a condition for the existence of nonzero solutions and leads to a characteristic equation with respect to spectral parameter

$$\begin{gathered} \Delta(z;\varepsilon) = \left(p_1q_2 - p_2q_1\right)\left(t_1p_2 - t_2p_1\right)sh^2\left(\varepsilon\left(s_1+s_2\right)\right) + \\ +\left(p_1t_2 - p_2q_1\right)\left(p_1q_2 - p_2t_1\right)sh^2\left(\varepsilon\left(s_2-s_1\right)\right) = 0. \end{gathered} \tag{23}$$

Equation (23) has countable set of roots z_k. The general solution to the problem is obtained by summing over the roots of equation (23)

$$u_\rho = \sum_{k=1}^{\infty} M_k a_k(\rho) m_k(\theta), \tag{24}$$

$$u_\theta = \sum_{k=1}^{\infty} M_k d_k(\rho) m_k'(\theta), \tag{25}$$

where

$$\begin{gathered} a_k(\rho) = e^{-\varepsilon\rho}\left[p_1\left(e^{\varepsilon s_1\rho}\omega_1 - e^{-\varepsilon s_1\rho}\omega_2\right) + p_2\left(e^{\varepsilon s_2\rho}\omega_3 - e^{-\varepsilon s_2\rho}\omega_4\right)\right], \\ d_k(\rho) = e^{-\varepsilon\rho}\left[t_1e^{\varepsilon s_1\rho}\omega_1 - q_1e^{-\varepsilon s_1\rho}\omega_2 + t_2e^{\varepsilon s_2\rho}\omega_3 - q_2e^{-\varepsilon s_2\rho}\omega_4\right], \\ \omega_1 = p_2q_1\left(q_2-t_2\right)e^{es_1} - t_2\left(p_1q_2 - p_2q_1\right)e^{-\varepsilon\left(s_1+2s_2\right)} + q_2\left(p_1t_2 - p_2q_1\right)e^{\varepsilon\left(2s_2-s_1\right)}, \\ \omega_2 = p_2t_1\left(q_2-t_2\right)e^{-es_1} - t_2\left(p_1q_2 - p_2t_1\right)e^{\varepsilon\left(s_1-2s_2\right)} + q_2\left(p_1t_2 - p_2t_1\right)e^{\varepsilon\left(s_1+2s_2\right)}, \\ \omega_3 = t_1\left(p_1q_2 - p_2q_1\right)e^{-\varepsilon\left(2s_1+s_2\right)} - q_1\left(p_1q_2 - p_2t_1\right)e^{\varepsilon\left(2s_1-s_2\right)} + p_1q_2\left(q_1-t_1\right)e^{\varepsilon s_2}, \\ \omega_4 = t_1\left(p_1t_2 - p_2q_1\right)e^{\varepsilon\left(s_2-2s_1\right)} - q_1\left(p_1t_2 - p_2t_1\right)e^{\varepsilon\left(2s_1+s_2\right)} + p_1t_2\left(q_1-t_1\right)e^{-\varepsilon s_2}. \end{gathered}$$

The set of roots of equation (23) at $\varepsilon \to 0$ consists of countable sets of roots

$$z_k = \frac{\delta_{0k}}{\varepsilon} + O(\varepsilon). \tag{26}$$

For δ_{0k}, we have:

1^0. At $b_1 > 0,\ b_1^2 - b_2 > 0$:

$$\left(s_1-s_2\right)\left(b_{44}^{(0)} - b_{11}^{(0)}s_1s_2\right)\sin\left(\left(s_1+s_2\right)\delta\right) \pm \left(s_1+s_2\right)\left(b_{44}^{(0)} + b_{11}^{(0)}s_1s_2\right)\sin\left(\left(s_1-s_2\right)\delta\right) = 0, \tag{27}$$

where

$$\begin{gathered} s_1 = \sqrt{b_1 + \sqrt{b_1^2 - b_2}};\quad s_2 = \sqrt{b_1 - \sqrt{b_1^2 - b_2}}; \\ b_1 = \left(2b_{44}^{(0)}b_{11}^{(0)}\right)^{-1}\left(2b_{44}^{(0)}b_{12}^{(0)} + (b_{12}^{(0)})^2 - b_{11}^{(0)}b_{22}^{(0)}\right);\ b_2 = b_{22}^{(0)}(b_{11}^{(0)})^{-1}. \end{gathered}$$

2^0. At $b_1 > 0,\ b_1^2 - b_2 < 0$:

$$\begin{gathered} \beta\left[2b_{11}^{(0)}\alpha^2 - \left(b_{11}^{(0)}\left(\alpha^2-\beta^2\right) - b_{44}^{(0)}\right)\right]sh\left(2\delta\alpha\right) \pm \\ \pm\alpha\left[2b_{11}^{(0)}\beta^2 + \left(b_{11}^{(0)}\left(\alpha^2-\beta^2\right) - b_{44}^{(0)}\right)\right]\sin\left(2\delta\beta\right) = 0, \end{gathered} \tag{28}$$

where

$$\begin{gathered} s_1 = \sqrt{b_1 + \sqrt{b_1^2 - b_2}} = \pm(\alpha + i\beta); \\ s_2 = \sqrt{b_1 - \sqrt{b_1^2 - b_2}} = \pm(\alpha - i\beta). \end{gathered}$$

3^0. At $b_1 > 0,\ b_1^2 = b_2$:

$$\left(b_{11}^{(0)}s^2 - b_{44}^{(0)}\right)\sin\left(2s\delta\right) \pm 2\left(b_{11}^{(0)}s^2 + b_{44}^{(0)}\right)\delta s = 0, \tag{29}$$

where $s = \sqrt{b_1}$.

4^0. At $b_1 < 0,\ b_1^2 - b_2 > 0$:

$$\left(s_1 - s_2\right)\left(b_{44}^{(0)} - b_{11}^{(0)}s_1 s_2\right)sh\left(\left(s_1 + s_2\right)\delta\right) \pm \left(s_1 + s_2\right)\left(b_{44}^{(0)} + b_{11}^{(0)}s_1 s_2\right)sh\left(\left(s_1 - s_2\right)\delta\right) = 0, \tag{30}$$

where

$s_1 = \sqrt{|b_1| - \sqrt{b_1^2 - b_2}}$; $\quad s_2 = \sqrt{|b_1| + \sqrt{b_1^2 - b_2}}$.

5^0. At $b_1 < 0,\ b_1^2 - b_2 < 0$:

$$\begin{aligned} &\beta\left[2b_{11}^{(0)}\alpha^2 - \left(b_{11}^{(0)}\left(\alpha^2 - \beta^2\right) - b_{44}^{(0)}\right)\right]\sin\left(2\delta\alpha\right) \pm \\ &\pm\alpha\left[2b_{11}^{(0)}\beta^2 + \left(b_{11}^{(0)}\left(\alpha^2 - \beta^2\right) - b_{44}^{(0)}\right)\right]sh\left(2\delta\beta\right) = 0, \end{aligned} \tag{31}$$

where

$s_1 = \sqrt{|b_1| - \sqrt{b_1^2 - b_2}} = \pm(\alpha - i\beta)$; $\quad s_2 = \sqrt{|b_1| + \sqrt{b_1^2 - b_2}} = \pm(\alpha + i\beta)$.

6^0. At $b_1 < 0,\ b_1^2 = b_2$:

$$\left(b_{11}^{(0)}s^2 - b_{44}^{(0)}\right)sh\left(2s\delta\right) \pm 2\left(b_{11}^{(0)}s^2 + b_{44}^{(0)}\right)\delta s = 0, \tag{32}$$

where $s = \sqrt{|b_1|}$.

Equation (27)–(32) has a countable set of solutions.

Let us present an asymptotic construction of solutions corresponding to different groups of roots of the characteristic equation (23). Substituting (26) into (24), (25) and expanding the resulting expressions in powers ε, we have:

1^0.

$$\begin{aligned} \text{a) } u_p\left(\rho;\theta\right) = \sum_{k=1}^{\infty} E_k^{(1)}\delta_k^5 \Big\{\left(b_{44}^{(0)} + b_{12}^{(0)}\right)\Big[\left(b_{44}^{(0)} + b_{11}^{(0)}s_2^2\right)s_1\cos\left(\delta_k s_2\right)\sin\left(\delta_k s_1\rho\right) - \\ -\left(b_{44}^{(0)} + b_{11}^{(0)}s_1^2\right)s_2\cos\left(\delta_k s_1\right)\sin\left(\delta_k s_2\rho\right)\Big] + O\left(\varepsilon\right)\Big\} m_k\left(\theta\right), \end{aligned} \tag{33}$$

$$u_\theta\left(\rho;\theta\right) = \sum_{k=1}^{\infty} E_k^{(1)}\delta_k^4 \Big\{\left(b_{44}^{(0)} + b_{11}^{(0)}s_1^2\right)\left(b_{44}^{(0)} + b_{11}^{(0)}s_2^2\right)\Big[\cos\left(\delta_k s_2\right)\cos\left(\delta_k s_1\rho\right) - \cos\left(\delta_k s_1\right)\cos\left(\delta_k s_2\rho\right)\Big] + O\left(\varepsilon\right)\Big\} m_k'\left(\theta\right), \tag{34}$$

where δ_{0k} are the solutions to equation

$$\left(s_1 - s_2\right)\left(b_{44}^{(0)} - b_{11}^{(0)}s_1 s_2\right)\sin\left(\left(s_1 + s_2\right)\delta\right) + \left(s_1 + s_2\right)\left(b_{44}^{(0)} + b_{11}^{(0)}s_1 s_2\right)\sin\left(\left(s_1 - s_2\right)\delta\right) = 0 \tag{35}$$

$$\begin{aligned} \text{б) } u_p\left(\rho;\theta\right) = \sum_{k=1}^{\infty} E_k^{(2)}\delta_k^5 \Big\{\left(b_{44}^{(0)} + b_{12}^{(0)}\right)\Big[\left(b_{44}^{(0)} + b_{11}^{(0)}s_2^2\right)s_1\sin\left(\delta_k s_2\right)\cos\left(\delta_k s_1\rho\right) - \\ -\left(b_{44}^{(0)} + b_{11}^{(0)}s_1^2\right)s_2\sin\left(\delta_k s_1\right)\cos\left(\delta_k s_2\rho\right)\Big] + O\left(\varepsilon\right)\Big\} m_k\left(\theta\right), \end{aligned} \tag{36}$$

$$u_\theta\left(\rho;\theta\right) = \sum_{k=1}^{\infty} E_k^{(2)}\delta_k^4 \Big\{\left(b_{44}^{(0)} + b_{11}^{(0)}s_1^2\right)\left(b_{44}^{(0)} + b_{11}^{(0)}s_2^2\right)\Big[\sin\left(\delta_k s_1\right)\sin\left(\delta_k s_2\rho\right) - \sin\left(\delta_k s_2\right)\sin\left(\delta_k s_1\rho\right)\Big] + O\left(\varepsilon\right)\Big\} m_k'\left(\theta\right), \tag{37}$$

where δ_{0k} are the solutions to equation

$$\left(s_1 - s_2\right)\left(b_{44}^{(0)} - b_{11}^{(0)}s_1 s_2\right)\sin\left(\left(s_1 + s_2\right)\delta\right) - \left(s_1 + s_2\right)\left(b_{44}^{(0)} + b_{11}^{(0)}s_1 s_2\right)\sin\left(\left(s_1 - s_2\right)\delta\right) = 0\ . \tag{38}$$

2^0.

a) $$u_p(\rho;\theta)=\sum_{k=1}^{\infty}E_k^{(3)}\delta_k^5\left(b_{44}^{(0)}+b_{12}^{(0)}\right)\Big\{\left[\beta\sin(\delta_k\beta\rho)sh(\delta_k\alpha\rho)-\alpha\cos(\delta_k\beta\rho)ch(\delta_k\alpha\rho)\right]\cdot$$

$$\cdot\left[2\alpha\beta b_{11}^{(0)}\cos(\delta_k\beta)sh(\delta_k\alpha)+\left(b_{11}^{(0)}\left(\alpha^2-\beta^2\right)-b_{44}^{(0)}\right)\sin(\delta_k\beta)ch(\delta_k\alpha)\right]-$$

$$-\left[\alpha\sin(\delta_k\beta\rho)sh(\delta_k\alpha\rho)+\beta\cos(\delta_k\beta\rho)ch(\delta_k\alpha\rho)\right]\cdot$$

$$\cdot\left[2\alpha\beta b_{11}^{(0)}\sin(\delta_k\beta)ch(\delta_k\alpha)-\left(b_{11}^{(0)}\left(\alpha^2-\beta^2\right)-b_{44}^{(0)}\right)\cos(\delta_k\beta)sh(\delta_k\alpha)\right]+O(\varepsilon)\Big\}m_k(\theta), \tag{39}$$

$$u_\theta(\rho;\theta)=\sum_{k=1}^{\infty}E_k^{(3)}\delta_k^4\Big\{\left[2\alpha\beta b_{11}^{(0)}\sin(\delta_k\beta\rho)ch(\delta_k\alpha\rho)-\left(b_{11}^{(0)}\left(\alpha^2-\beta^2\right)-b_{44}^{(0)}\right)\times\right.$$

$$\left.\times\cos(\delta_k\beta\rho)sh(\delta_k\alpha\rho)\right]\left[2\alpha\beta b_{11}^{(0)}\cos(\delta_k\beta)sh(\delta_k\alpha)+\left(b_{11}^{(0)}\left(\alpha^2-\beta^2\right)-b_{44}^{(0)}\right)\sin(\delta_k\beta)ch(\delta_k\alpha)\right]-$$

$$-\left[2\alpha\beta b_{11}^{(0)}\cos(\delta\beta_k\rho)sh(\delta_k\alpha\rho)+\left(b_{11}^{(0)}\left(\alpha^2-\beta^2\right)-b_{44}^{(0)}\right)\sin(\delta_k\beta\rho)ch(\delta_k\alpha\rho)\right]\times$$

$$\times\left[2\alpha\beta b_{11}^{(0)}\sin(\delta_k\beta)ch(\delta_k\alpha)-\left(b_{11}^{(0)}\left(\alpha^2-\beta^2\right)-b_{44}^{(0)}\right)\cos(\delta_k\beta)sh(\delta_k\alpha)\right]+O(\varepsilon)\Big\}m_k'(\theta), \tag{40}$$

where δ_{0k} are the solutions to equation

$$\beta\left[2b_{11}^{(0)}\alpha^2-\left(b_{11}^{(0)}\left(\alpha^2-\beta^2\right)-b_{44}^{(0)}\right)\right]sh(2\delta\alpha)+\alpha\left[2b_{11}^{(0)}\beta^2+\left(b_{11}^{(0)}\left(\alpha^2-\beta^2\right)-b_{44}^{(0)}\right)\right]\sin(2\delta\beta)=0. \tag{41}$$

б) $$u_p(\rho;\theta)=\sum_{k=1}^{\infty}E_k^{(4)}\delta_k^5\left(b_{44}^{(0)}+b_{12}^{(0)}\right)\Big\{\left[\beta\sin(\delta_k\beta\rho)ch(\delta_k\alpha\rho)-\alpha\cos(\delta_k\beta\rho)sh(\delta_k\alpha\rho)\right]\cdot$$

$$\cdot\left[2\alpha\beta b_{11}^{(0)}\cos(\delta_k\beta)ch(\delta_k\alpha)+\left(b_{11}^{(0)}\left(\alpha^2-\beta^2\right)-b_{44}^{(0)}\right)\sin(\delta_k\beta)sh(\delta_k\alpha)\right]-$$

$$-\left[\alpha\sin(\delta_k\beta\rho)ch(\delta_k\alpha\rho)+\beta\cos(\delta_k\beta\rho)sh(\delta_k\alpha\rho)\right]\left[2\alpha\beta b_{11}^{(0)}\sin(\delta_k\beta)sh(\delta_k\alpha)-\right.$$

$$\left.-\left(b_{11}^{(0)}\left(\alpha^2-\beta^2\right)-b_{44}^{(0)}\right)\cos(\delta_k\beta)ch(\delta_k\alpha)\right]+O(\varepsilon)\Big\}m_k(\theta), \tag{42}$$

$$u_\theta(\rho;\theta)=\sum_{k=1}^{\infty}E_k^{(4)}\delta_k^4\Big\{\left[2\alpha\beta b_{11}^{(0)}\sin(\delta_k\beta\rho)sh(\delta_k\alpha\rho)-\left(b_{11}^{(0)}\left(\alpha^2-\beta^2\right)-b_{44}^{(0)}\right)\times\right.$$

$$\left.\times\cos(\delta_k\beta\rho)ch(\delta_k\alpha\rho)\right]\left[2\alpha\beta b_{11}^{(0)}\cos(\delta_k\beta)ch(\delta_k\alpha)+\left(b_{11}^{(0)}\left(\alpha^2-\beta^2\right)-b_{44}^{(0)}\right)\sin(\delta_k\beta)sh(\delta_k\alpha)\right]-$$

$$-\left[2\alpha\beta b_{11}^{(0)}\cos(\delta\beta_k\rho)ch(\delta_k\alpha\rho)+\left(b_{11}^{(0)}\left(\alpha^2-\beta^2\right)-b_{44}^{(0)}\right)\sin(\delta_k\beta\rho)sh(\delta_k\alpha\rho)\right]\times$$

$$\times\left[2\alpha\beta b_{11}^{(0)}\sin(\delta_k\beta)sh(\delta_k\alpha)-\left(b_{11}^{(0)}\left(\alpha^2-\beta^2\right)-b_{44}^{(0)}\right)\cos(\delta_k\beta)ch(\delta_k\alpha)\right]+O(\varepsilon)\Big\}m_k'(\theta), \tag{43}$$

where δ_{0k} are the solutions to equation

$$\beta\left[2b_{11}^{(0)}\alpha^2-\left(b_{11}^{(0)}\left(\alpha^2-\beta^2\right)-b_{44}^{(0)}\right)\right]sh(2\delta\alpha)-\alpha\left[2b_{11}^{(0)}\beta^2+\left(b_{11}^{(0)}\left(\alpha^2-\beta^2\right)-b_{44}^{(0)}\right)\right]\sin(2\delta\beta)=0. \tag{44}$$

3^0.

a) $$u_p(\rho;\theta)=\sum_{k=1}^{\infty}E_k^{(5)}\Big\{\left(b_{11}^{(0)}s^2+b_{44}^{(0)}\right)\left(\cos(\delta_k s)\cos(\delta_k s\rho)+\rho\sin(\delta_k s)\sin(\delta_k s\rho)\right)+$$

$$+\frac{\left(b_{11}^{(0)}s^2-b_{44}^{(0)}\right)}{s\delta_k}\sin\left(\delta_k s\right)\cos\left(\delta_k s\rho\right)+O\left(\varepsilon\right)\Bigg\}m_k\left(\theta\right), \tag{45}$$

$$u_\theta\left(\rho;\theta\right)=\sum_{k=1}^{\infty}E_k^{(5)}\left\{\frac{\left(b_{11}^{(0)}s^2+b_{44}^{(0)}\right)^2}{\left(b_{44}^{(0)}s^2+b_{12}^{(0)}\right)\delta_k s}\times\right.$$

$$\left.\times\left(\rho\sin\left(\delta_k s\right)\cos\left(\delta_k s\rho\right)-\cos\left(\delta_k s\right)\sin\left(\delta_k s\rho\right)\right)+O\left(\varepsilon\right)\right\}m_k'\left(\theta\right), \tag{46}$$

where δ_{0k} are the solutions to equation

$$\left(b_{11}^{(0)}s^2-b_{44}^{(0)}\right)\sin\left(2s\delta\right)+2\left(b_{11}^{(0)}s^2+b_{44}^{(0)}\right)\delta s=0 \tag{47}$$

б) $$u_\rho\left(\rho;\theta\right)=\sum_{k=1}^{\infty}E_k^{(6)}\left\{\frac{\left(b_{11}^{(0)}s^2-b_{44}^{(0)}\right)}{\delta_k s}\cos\left(\delta_k s\right)\sin\left(\delta_k s\rho\right)-\left(b_{11}^{(0)}s^2+b_{44}^{(0)}\right)\times\right.$$

$$\left.\times\left(\sin\left(\delta_k s\right)\sin\left(\delta_k s\rho\right)+\rho\cos\left(\delta_k s\right)\cos\left(\delta_k s\rho\right)\right)+O\left(\varepsilon\right)\right\}m_k\left(\theta\right) \tag{48}$$

$$u_\theta\left(\rho;\theta\right)=\sum_{k=1}^{\infty}E_k^{(6)}\left\{\frac{\left(b_{11}^{(0)}s^2+b_{44}^{(0)}\right)^2}{\left(b_{44}^{(0)}+b_{12}^{(0)}\right)\delta_k s}\times\right.$$

$$\left.\times\left[\rho\cos\left(\delta_k s\right)\sin\left(\delta_k s\rho\right)-\sin\left(\delta_k s\right)\cos\left(\delta_k s\rho\right)\right]+O\left(\varepsilon\right)\right\}m_k'\left(\theta\right), \tag{49}$$

where δ_{0k} are the solutions to equation

$$\left(b_{11}^{(0)}s^2-b_{44}^{(0)}\right)\sin\left(2s\delta\right)-2\left(b_{11}^{(0)}s^2+b_{44}^{(0)}\right)\delta s=0 \tag{50}$$

4^0. In case $b_1<0,\ b_1^2-b_2>0$, asymptotic formulas for displacements are obtained from (33)–(38) through replacing s_1,s_2 with is_1,is_2.

5^0. In case $b_1<0,\ b_1^2-b_2<0$, asymptotic formulas for displacements are obtained from (39)–(44) through replacing s_1,s_2 with is_1,is_2.

6^0. In case $b_1<0,\ b_1^2=b_2$, all asymptotic formulas for displacements are obtained from (45)–(50) through replacing s with is.

For roots (26), the main term of the asymptotic solution of equation (15) at $\varepsilon\to 0$ takes the form [9, 10]:

$$m_k(\theta)=\begin{cases}\dfrac{1}{\sqrt{\sin\theta}}\dfrac{1}{\sqrt[4]{-\delta_{0k}^2}}\exp\left[-\varepsilon^{-1}\sqrt{-\delta_{0k}^2}\left(\theta-\theta_1\right)\right]\left(1+O(\varepsilon)\right);\ near\ \ \theta=\theta_1,\\ \dfrac{1}{\sqrt{\sin\theta}}\dfrac{1}{\sqrt[4]{-\delta_{0k}^2}}\exp\left[\varepsilon^{-1}\sqrt{-\delta_{0k}^2}\left(\theta-\theta_2\right)\right]\left(1+O(\varepsilon)\right);\ near\ \ \theta=\theta_2.\end{cases} \tag{51}$$

We represent displacements in the form:

$$u_\rho(\rho,\theta)=\sum_{k=1}^{\infty}E_k a_k(\rho)m_k(\theta), \tag{52}$$

$$u_\theta(\rho,\theta)=\sum_{k=1}^{\infty}E_k d_k(\rho)m_k'(\theta). \tag{53}$$

We represent stresses $\sigma_{\rho\theta}$ and $\sigma_{\theta\theta}$ in the form:

$$\sigma_{\theta\theta}=\sum_{k=1}^{\infty}E_k\left(\sigma_{1k}^{(1)}(\rho)m_k(\theta)+\sigma_{1k}^{(2)}(\rho)m_k'(\theta)ctg\theta\right), \tag{54}$$

$$\sigma_{\rho\theta} = \sum_{k=1}^{\infty} E_k \sigma_{2k}(\rho) m_k'(\theta), \tag{55}$$

here,

$$\sigma_{1k}^{(1)}(\rho) = \frac{1}{\varepsilon}\left[b_{12}^{(0)} a_k'(\rho) + \varepsilon\left(b_{22}^{(0)} + b_{23}^{(0)}\right) a_k(\rho) - \varepsilon b_{22}^{(0)} \left(z_k^2 - \frac{1}{4} \right) d_k(\rho) \right];$$

$$\sigma_{1k}^{(2)}(\rho) = \left(b_{23}^{(0)} - b_{22}^{(0)}\right) d_k(\rho);$$

$$\sigma_{2k}(\rho) = \frac{b_{44}^{(0)}}{\varepsilon}\left[d_k'(\rho) + \varepsilon(a_k(\rho) - d_k(\rho)) \right].$$

The character of solutions (33)–(50) depends essentially on the type of roots δ_{0k}. The first boundary-layer terms of these solutions correspond to the Saint-Venant edge effect [4]. In the case of imaginary roots δ_{0k}, these boundary layers have weak damping. Thus, the stress-strain state is far enough away from the ends and significantly depends on them. That is, in this case, the transversely isotropic properties of the inhomogeneous material significantly, in comparison to the isotropic material of the sphere, change the pattern of the stress-strain state. At the same time, for real or complex δ_{0k}, the pattern of the stress-strain state of an inhomogeneous sphere for such materials qualitatively coincides, differing in the decay rate of the above-described Saint-Venant boundary layer solutions of an inhomogeneous plate.

From (51), it turns out that when moving away from the conic sections $\theta = \theta_j \,(j = 1, 2)$, solutions(33)–(50) decrease exponentially.

Since the constructed solutions satisfy the equilibrium equation and boundary conditions on the side surface, the Lagrange variational principle takes the following form [4, 11]:

$$\sum_{j=1}^{2} \int_{-1}^{1} \left[\left(\sigma_{\theta\theta} - f_{1j}(\rho)\right)\delta u_\theta + \left(\sigma_{\rho\theta} - f_{2j}(\rho)\right)\delta u_\rho \right]\Big|_{\theta=\theta_j} e^{2\varepsilon\rho} d\rho = 0. \tag{56}$$

Substituting (52)–(55) into (56) and taking δE_k as independent variations, we obtain an infinite system of linear algebraic equations

$$\sum_{k=1}^{\infty} E_k q_{jk} = \tau_j, \quad (j = 1, 2, ...), \tag{57}$$

Here,

$$q_{jk} = \int_{-1}^{1} \sigma_{1k}^{(1)}(\rho) d_j(\rho) e^{2\varepsilon\rho} d\rho \left(\sum_{s=1}^{2} m_k(\theta_s) m_j'(\theta_s) \right) + \int_{-1}^{1} \sigma_{1k}^{(2)}(\rho) d_j(\rho) e^{2\varepsilon\rho} d\rho \times$$

$$\times \left(\sum_{s=1}^{2} m_k'(\theta_s) m_j'(\theta_s) ctg\theta_s \right) + \int_{-1}^{1} \sigma_{2k}(\rho) a_j(\rho) e^{2\varepsilon\rho} d\rho \left(\sum_{s=1}^{2} m_k'(\theta_s) m_j(\theta_s) \right),$$

$$\tau_j = \sum_{s=1}^{2} \left[m_j'(\theta_s) \int_{-1}^{1} f_{1s}^*(\rho) d_j(\rho) e^{2\varepsilon\rho} d\rho + m_j(\theta_s) \int_{-1}^{1} f_{2s}(\rho) a_j(\rho) e^{2\varepsilon\rho} d\rho \right].$$

System (57) is always solvable under physically meaningful conditions imposed on the right side (57). The solvability and convergence of the reduction method for (57) is proved in [12].

Using the smallness of parameter ε, it is possible to construct asymptotic solutions of system (57).

Research Results. The structure of the stress-strain state of a radially inhomogeneous transversally isotropic sphere of small thickness is analyzed under kinematic conditions on the side surface. It is shown that, in the case of fixing the side surface, the character of the solution is determined by the boundary layers. It is found that the asymptotic decomposition of the stress state starts with a solution describing the Saint-Venant edge effect in the theory of transversally isotropic inhomogeneous plates. In the case of transversal isotropy of the radially inhomogeneous material of the sphere, some boundary layer solutions decay very weakly, they can penetrate deep far from the conic sections and change the pattern of the stress-strain state. Asymptotic relations for displacements and stresses are derived, which provide calculating the three-dimensional stress-strain state of a radially inhomogeneous transversally isotropic sphere of small thickness with any predetermined accuracy. It is shown that the root branching generates a countable set of new solutions for a transversely isotropic radially inhomogeneous sphere.

Discussion and Conclusions. An asymptotic analysis of the stress-strain state of inhomogeneous shells, based on three-dimensional equations of elasticity theory, makes it possible to establish the limits of application of approximate theories. The identified behavior pattern of the solution far from the ends for different boundary conditions on the side surfaces can become the basis for creating refined applied theories for calculating the deformation of a radially inhomogeneous transversally isotropic spherical shell of small thickness. One of the applications of the asymptotic analysis performed can be the calculation of shells with thin coatings, in which, in this case, a radial inhomogeneity arises [13, 14].

References

1. Galerkin BG. Ravnovesie uprugoi sfericheskoi obolochki. Journal of Applied Mathematics and Mechanics. 1942;6:487–496. (In Russ.)

2. Lurie AI. Ravnovesie uprugoi simmetrichno nagruzhennoi sfericheskoi obolochki. Applied Mathematics and Mechanics. 1942;7:393–404. (In Russ.)

3. Vilenskaya TV, Vorovich II. Asimptoticheskoe povedenie resheniya zadachi teorii uprugosti dlya sfericheskoi obolochki maloi tolshchiny. Applied Mathematics and Mechanics. 1966;30:278–295. (In Russ.)

4. Mekhtiyev MF. Asymptotic analysis of spatial problems in elasticity. Springer. 2019;99:241. https://link.springer.com/book/10.1007/978-981-13-3062-95.

5. Boev YuA, Ustinov NV. Prostranstvennoe napryazhenno- deformirovannoe sostoyanie trekhsloinoi sfericheskoi obolochki. Izvestiya Akademii nauk SSSR. Mekhanika tverdogo tela. 1985;3:136–143. (In Russ.)

6. Akhmedov NK, Mamedova TB. Asymptotic behavior of solution to torsion problem for radially inhomogeneous transversally isotropic spherical shell. Vestnik of DSTU. 2011;11:455–461.

7. Akhmedov NK, Ustinov YuA. Analysis of the structure of the boundary layer in the problem of the torsion of a laminated spherical shell. Applied Mathematics and Mechanics. 2009;73:416–426.

8. Grigorenko AYa, Yaremchenko NP, Yaremchenko SN. Analysis of the axisymmetric stress-strain state of a continuously inhomogeneous hollow sphere. International Applied Mechanics. 2018;54:577–583. https://doi.org/10.1007/s10778-018-0911-1

9. Akhmedov NK, Sofiyev AH. Asymptotic analysis of three-dimensional problem of elasticity theory for radially inhomogeneous transversally-isotropic thin hollow spheres. Thin-Walled Structures. 2019;139:232–241. http://dx.doi.org/10.1016/j.tws.2019.03.022

10. Akhmedov NK, Gasanova NS. Asymptotic behavior of the solution of an axisymmetric problem of elasticity theory for a sphere with variable elasticity modules. Mathematics and Mechanics of Solids. 2020;25:2231–2251. https://doi.org/10.1177/1081286520932363

11. Lurie AI. Theory of Elasticity. Moscow: Nauka; 1970. 939 p. (In Russ.)

12. Ustinov YuA. Matematicheskaya teoriya poperechno-neodnorodnykh plit. Rostov-on-Don: TsVVR; 2006. 257 p. (In Russ.)

13. Tolokonnikov LA. Diffraction of cylindrical sound waves by an elastic sphere with an inhomogeneous coating. Journal of Applied Mathematics and Mechanics. 2015;79:467–474. https://doi.org/10.1016/j.jappmathmech.2016.03.008

14. Kiani M, Abdolali A, Safari M. Radially inhomogeneous spherical structures; analysis of EM scattering using Taylor's series method and their potential applications. AEU – International Journal of Electronics and Communications. 2017;80:199–209.

Received 12.01.2022
Revised 06.02.2022
Accepted 10.02.2022

About the Authors:

Akhmedov, Natiq K., Head of the Mathematics and Statistics Department, Azerbaijan State University of Economics (UNEC) (6, Istiglaliyyat St., Baku, AZ 1001, Azerbaijan), Dr.Sci. (Math.), Scopus, ORCID, anatiq@gmail.com

Yusubova, Sevinj M., teacher, G. Aliyev Lyceum (50, N. Aliyev St., Baku, AZ 1025, Azerbaijan), sevinc.yusubova.75@mail.ru

Claimed contributorship

N. K. Akhmedov: task formulation; selection of the research method; discussion of the results. S. M. Yusubova: construction of an asymptotic solution to a problem with kinematic boundary conditions on lateral surfaces; discussion of the results; manuscript preparation.

All authors have read and approved the final manuscript.

MECHANICS

Check for updates

UDC 534.1:629.7

Original article

https://doi.org/10.23947/2687-1653-2022-22-1-24-29

On the ambiguity of mechanical power

Valentin D. Pavlov ✉
Vladimir Electromechanical Plant (Vladimir, Russian Federation)
✉pavlov.val.75@mail.ru

Introduction. Mechanical vibrations are widespread in the production processes. The drives of machines and mechanisms are mainly electromechanical, so mechanical reactive power is transformed into electrical reactive power of the network, impairing the quality of electricity. This explains the significance of considering the mechanical reactive power, and, as a consequence, the urgency of the presented study. The research objective is to detail the types of mechanical power under harmonic vibrations.
Materials and Methods. The literature on the issues of dynamics, kinematics, vibrations, transformation of motion in oscillatory systems, etc., has been studied. Theoretical, mainly mathematical methods of research are used.
Results. The powers developed under elastic deformations, forced harmonic vibrations of an inert body, and vibrations associated with gravitational influence, as well as reactive, active, full powers in the complex formulation, and mechanical powers in the vector representation are mathematically interpreted.
Discussion and Conclusions. Under the mechanical harmonic vibrations, along with the sign-positive thermal power, sign-variable reactive powers develop, characterizing the reversibility of kinetic and potential energies. The total mechanical power satisfies the Pythagorean formula. The concept of mechanical reactive, active, and total powers generalizes the corresponding concepts of power from electrical engineering, and thus manifesting electromechanical dualism.

Keywords: mechanical power, kinetic energy, potential energy, complex formulation, vector representation.

For citation: Pavlov V. D. On the ambiguity of mechanical power. Advanced Engineering Research, 2022, vol. 22, no. 1, pp. 24–29. (In Russ). https://doi.org/10.23947/2687-1653-2022-22-1-24-29

Introduction. Mechanical energy can be reversible (potential and kinetic), as well as irreversible (e.g., thermal in friction). The time derivative of the latter is taken as mechanical power. Note that due to the irreversibility of thermal energy, its derivative takes only positive values. At the same time, derivatives are obtained from both potential and kinetic energy. Of particular interest are harmonic vibrations [1–4], where derivatives (instantaneous powers) will be alternating functions, which fundamentally distinguishes them from thermal power.

The analogue of kinetic energy in electrical engineering is the magnetic field energy of the inductor, the analogue of potential energy is the capacitor electric field energy, and the analogue of mechanical thermal energy is the thermal energy dissipated by the resistor.

Mechanical vibrations are widespread in various production processes [5–8]. The drives of machines and mechanisms are mainly electromechanical [9–12], therefore, mechanical reactive power is transformed into electrical reactive power of the network, impairing the quality of electricity. In this regard, accounting for mechanical reactive power is of no small importance [14], and this determines the urgency of the presented study.

Materials and Methods. Mechanical power under harmonic vibrations is considered. As a literary basis, domestic and foreign sources, which cover the issues on dynamics, kinematics, vibrations, transformation of motion in oscillatory systems, etc., have been studied. Theoretical (mainly mathematical) research methods are used.

Research Results

The power developed by forced harmonic vibrations of an inert body. The body motion is described by the well-known expression:

$$x = l\sin\omega t\,.$$

Accordingly, the speed:

$$v = \dot{x} = l\omega\cos\omega t = V_m\cos\omega t.$$

For harmonic quantity, the effective value is less than the amplitude in $\sqrt{2}$:

$$V = \frac{V_m}{\sqrt{2}} = \frac{l\omega}{\sqrt{2}}. \tag{1}$$

Formula for the force is:

$$f_a = m\ddot{x} = -lm\omega^2\sin\omega t. \tag{2}$$

Formula for friction force is:

$$f_\mu = \mu\dot{x} = \mu l\omega\cos\omega t\,. \tag{3}$$

Resultant force is:

$$f = f_a + f_\mu = -lm\omega^2\sin\omega t + \mu l\omega\cos\omega t =$$

$$= l\omega\sqrt{\mu^2+m^2\omega^2}\left(\frac{\mu}{\sqrt{\mu^2+m^2\omega^2}}\cos\omega t - \frac{m\omega}{\sqrt{\mu^2+m^2\omega^2}}\sin\omega t\right).$$

Denote:

$$\varphi = \operatorname{arctg}\frac{m\omega}{\mu}. \tag{4}$$

With this in mind:

$$f = l\omega\sqrt{\mu^2+m^2\omega^2}\left(\cos\varphi\cos\omega t - \sin\varphi\sin\omega t\right) = l\omega\sqrt{\mu^2+m^2\omega^2}\cos(\omega t+\varphi).$$

Obviously,

$$F_m = l\omega\sqrt{\mu^2+m^2\omega^2}.$$

The effective value of the resultant force:

$$F = \frac{F_m}{\sqrt{2}} = \frac{l\omega\sqrt{\mu^2+m^2\omega^2}}{\sqrt{2}}. \tag{5}$$

Instantaneous resultant power:

$$s = fv = l\omega\sqrt{\mu^2+m^2\omega^2}\cos(\omega t+\varphi)l\omega\cos\omega t =$$

$$= 0,5l^2\omega^2\sqrt{\mu^2+m^2\omega^2}\left[\cos\varphi + \cos(2\omega t+\varphi)\right] =$$

$$= FV\left[\cos\varphi + \cos(2\omega t+\varphi)\right] =$$

$$= FV\left(\cos\varphi + \cos 2\omega t\cos\varphi - \sin 2\omega t\sin\varphi\right) =$$

$$= FV\cos\varphi\left(1+\cos 2\omega t\right) - FV\sin\varphi\sin 2\omega t = p + q_i. \tag{6}$$

In electrical engineering, there is an expression similar to (6), with substitutions $F \to U$ $V \to I$. The active power is determined from it:

$$P = UI\cos\varphi.$$

Therefore, the active (thermal) mechanical power should also be defined as:

$$P = FV\cos\varphi. \tag{7}$$

It is obvious that the harmonic force and velocity vibrate with a phase shift equal to φ.

From the above-mentioned formula of electrical engineering, the reactive power is determined:

$$P = UI\sin\varphi.$$

So, reactive (inertial) mechanical power should also be defined as:

$$Q_i = FV\sin\varphi. \tag{8}$$

It follows from (6) that the active power is the half-period average of the instantaneous power, and the reactive power is the amplitude value. In electrical engineering, it is similar.

Another generalization from electrical engineering is total mechanical power:

$$S = FV = \sqrt{Q_i^2 + P^2}. \tag{9}$$

It is remarkable in that, on the one hand, it is described by the Pythagorean formula, and on the other hand, it is equal to the product of the effective values of harmonic quantities.

With a view to (1), (5) and (8),

$$Q_i = FV\sin\varphi = \frac{l\omega\sqrt{\mu^2 + m^2\omega^2}}{\sqrt{2}} \frac{l\omega}{\sqrt{2}} \frac{m\omega}{\sqrt{\mu^2 + m^2\omega^2}} = \frac{ml^2\omega^3}{2}. \tag{10}$$

Here:

$$f_a v = -lm\omega^2 \sin\omega t \, l\omega\cos\omega t = -0{,}5 l^2 m\omega^3 \sin 2\omega t = -F_a V \sin 2\omega t = -Q_i \sin 2\omega t. \tag{11}$$

This corresponds to expressions (6) and (10).

Keeping in view (1), (5) and (7),

$$P = FV\cos\varphi = \frac{l\omega\sqrt{\mu^2 + m^2\omega^2}}{\sqrt{2}} \frac{l\omega}{\sqrt{2}} \frac{\mu}{\sqrt{\mu^2 + m^2\omega^2}} = \frac{\mu l^2\omega^2}{2}. \tag{12}$$

In addition:

$$f_\mu v = \mu l\omega\cos\omega t \, l\omega\cos\omega t = 0{,}5\mu l^2\omega^2(1+\cos 2\omega t) = F_\mu V(1+\cos 2\omega t) = P(1+\cos 2\omega t). \tag{13}$$

This corresponds to expressions (6) and (12).

Having in view (9), (10) and (12),

$$S = FV = \frac{l\omega\sqrt{\mu^2 + m^2\omega^2}}{\sqrt{2}} \frac{l\omega}{\sqrt{2}} = \frac{l^2\omega^2\sqrt{\mu^2 + m^2\omega^2}}{2}.$$

The power developed under elastic deformations. The expression for the force is:

$$f_k = kx = kl\sin\omega t. \tag{14}$$

Taking into account (3), the resultant force is:

$$f = f_k + f_\mu = kl\sin\omega t + \mu l\omega\cos\omega t =$$

$$= l\sqrt{k^2 + \mu^2\omega^2}\left(\frac{k}{\sqrt{k^2 + \mu^2\omega^2}}\sin\omega t + \frac{\mu\omega}{\sqrt{k^2 + \mu^2\omega^2}}\cos\omega t\right).$$

Denote:

$$\varphi = \operatorname{arctg}\frac{k}{\mu\omega}.$$

Hence,

$$f = l\sqrt{k^2 + \mu^2\omega^2}\left(\sin\varphi\sin\omega t + \cos\varphi\cos\omega t\right) = l\sqrt{k^2 + \mu^2\omega^2}\cos\left(\omega t - \varphi\right).$$

It is obvious that:

$$F_m = l\sqrt{k^2 + \mu^2\omega^2}.$$

The effective value of the resultant force is equal to:

$$F = \frac{F_m}{\sqrt{2}} = \frac{l\sqrt{k^2 + \mu^2\omega^2}}{\sqrt{2}}. \tag{15}$$

Instantaneous resultant power is:

$$s = fv = l\sqrt{k^2 + \mu^2\omega^2}\cos\left(\omega t - \varphi\right) l\omega\cos\omega t =$$

$$= 0{,}5 l^2\omega\sqrt{k^2 + \mu^2\omega^2}\left[\cos\varphi + \cos\left(2\omega t - \varphi\right)\right] =$$

$$= FV\left[\cos\varphi + \cos(2\omega t - \varphi)\right] =$$

$$= FV\left(\cos\varphi + \cos 2\omega t\cos\varphi + \sin 2\omega t\sin\varphi\right) =$$

$$= FV\cos\varphi\left(1+\cos 2\omega t\right) + FV\sin\varphi\sin 2\omega t = p + q_d. \quad (16)$$

Bearing in mind (6), (7) and (12), the active mechanical power is equal to:

$$P = FV\cos\varphi = \frac{l\sqrt{k^2+\mu^2\omega^2}}{\sqrt{2}}\frac{l\omega}{\sqrt{2}}\frac{\mu\omega}{\sqrt{k^2+\mu^2\omega^2}} = \frac{\mu l^2\omega^2}{2}.$$

Taking into account (15), (1), (8) and (16), the mechanical reactive (elastic) power is equal to:

$$Q_d = FV\sin\varphi = \frac{l\sqrt{k^2+\mu^2\omega^2}}{\sqrt{2}}\frac{l\omega}{\sqrt{2}}\frac{k}{\sqrt{k^2+\mu^2\omega^2}} = \frac{kl^2\omega}{2}. \quad (17)$$

Here:

$$f_k v = kl\sin\omega t\, l\omega\cos\omega t = 0{,}5kl^2\omega\sin 2\omega t = F_k V\sin 2\omega t = Q_d\sin 2\omega t. \quad (18)$$

This corresponds to expressions (16) and (17).

Obviously, the total power is:

$$S = FV = \sqrt{Q_d^2+P^2} = \frac{l^2\omega\sqrt{k^2+\mu^2\omega^2}}{2}.$$

Power during vibrations associated with gravitational influence. When the suspended load is deflected by angle α, the moment occurs:

$$M = mgL\alpha.$$

Suppose

$$\alpha = \alpha_0\sin\omega t.$$

Then

$$\dot{\alpha} = \alpha_0\omega\cos\omega t = \alpha_0\sqrt{\frac{g}{L}}\cos\omega t.$$

Instantaneous power has the form:

$$q_g = M\dot{\alpha} = mgL\alpha_0\sin\omega t\,\alpha_0\sqrt{\frac{g}{L}}\cos\omega t = 0{,}5m\alpha_0^2\sqrt{Lg^3}\sin 2\omega t.$$

Its amplitude and, accordingly, the reactive power of the gravitational effect is defined as:

$$Q_g = 0{,}5m\alpha_0^2\sqrt{Lg^3}.$$

Reactive, active and total power in a complex representation. In [15], it is shown that under an inert load,

$$\dot{V}_m = V_m e^{j\pi/2}.$$

In this case, the instantaneous speed is equal to:

$$v = V_m\cos\omega t = \operatorname{Im}\dot{V}_m.$$

Formulas for the effective values are not fundamentally different:

$$\dot{V} = Ve^{j\pi/2},\quad \dot{F} = Fe^{j(\pi/2+\varphi)}.$$

In electrical engineering, a feature of the complex representation is described in detail: when calculating the total power, one of the multiplied vectors must be conjugate.

$$\underline{S} = \dot{F}\overset{*}{V} = Fe^{j(\pi/2+\varphi)}Ve^{-j\pi/2} = FVe^{j(\pi/2+\varphi-\pi/2)} = FVe^{j\varphi} = FV\cos\varphi + jFV\sin\varphi = P + jQ_i.$$

This is an expression for an inert load. The elastic load differs in that the reactive power has the opposite sign:

$$\underline{S} = \dot{F}\overset{*}{V} = Fe^{j(\pi/2-\varphi)}Ve^{-j\pi/2} = FVe^{j(\pi/2-\varphi-\pi/2)} = FVe^{-j\varphi} = FV\cos\varphi - jFV\sin\varphi = P + jQ_d.$$

Here:

$$P = \operatorname{Re}\dot{F}\overset{*}{V},\quad Q = \operatorname{Im}\dot{F}\overset{*}{V}.$$

Mechanical powers in vector representation. The complex representation is based on the concept of vectors rotating in the complex plane. The same principle can be implemented in a three-dimensional Cartesian basis.

From (7)–(9), it follows:

$$P = \left(F,V\right),\quad Q = \left|\left[F,V\right]\right|,\quad S^2 = \left(F,V\right)^2 + \left[F,V\right]^2.$$

Mathematical abstraction with projections of rotating vectors has a specific material basis in the form of slot-and-crank mechanisms.

Discussion and Conclusions. Mathematical methods were used to study the following powers:

— under forced harmonic vibrations of an inert body,

— under elastic deformations,

— under vibrations associated with gravitational action,

— reactive, active and total (in complex representation),

— mechanical (in vector representation).

It is shown that under mechanical harmonic vibrations, not only sign-positive thermal power develops, but also alternating reactive powers characterizing the reversibility of kinetic and potential energies.

At the same time, the total mechanical power satisfies the Pythagorean formula.

The idea of mechanical reactive, active and total powers is a generalization of the corresponding concepts of power from electrical engineering, and thus, electromechanical dualism manifests itself.

References

1. Eliseev SV, Mironov AS, Vuong Quabg Truc. Dynamic damping under introduction of additional couplings and external actions. Vestnik of DSTU. 2019;19:38–44. https://doi.org/10.23947/1992-5980-2019-19-1-38-44

2. Eliseev SV, Orlenko AI, Nguyen Duc Huynh. Motion translation devices in dyad structure of mechanical oscillatory system. Vestnik of DSTU. 2017;17:46–59. https://doi.org/10.23947/1992-5980-2017-17-3-46-59

3. Zhang YF, Zhang W, Yao ZG. Analysis on nonlinear vibrations near internal resonances of a composite laminated piezoelectric rectangular plate. Engineering Structures. 2018;173:89–106. https://doi.org/10.1016/j.engstruct.2018.04.100

4. Beltran-Carbajal F, Silva-Navarro G, Vazquez-Gonzalez B. Multi-frequency harmonic vibration suppression on mass-spring-damper systems using active vibration absorbers. Advances in Vibration Engineering. 2016;4:1–12.

5. Xingbin Chen, Qingchun Hu, Zhongyang Xu, et al. Numerical Modeling and Dynamic Characteristics Study of Coupling Vibration of Multistage Face Gearsplanetary Transmission. Mechanical Sciences. 2019;10:475–495. https://doi.org/10.5194/ms-10-475-2019

6. Duygu Dönmez Demir, Erthan Koca. Variational Iteration Method for Transverse Vibrations of the Elastic, Tensioned Beam. International Journal of Materials, Mechanics and Manufacturing. 2017;5:187–190. https://doi.org/10.18178/ijmmm.2017.5.3.315

7. Zichen Zhang. Design and Optimization of Comb Drive Accelerator for High Frequency Oscillation. Modern Mechanical Engineering. 2018;8:1–10. https://doi.org/10.4236/mme.2018.81001

8. Birgersson F, Finnveden S, Nilsson C-M. A Spectral Super Element for Modelling of Plate Vibration. Part 1: General Theory. Sound and Vibration. 2005;287:297–314. https://doi.org/10.1016/j.jsv.2004.11.012

9. Han Gao, Michaël De Volder, Tinghai Cheng, et al. A pneumatic actuator based on vibration friction reduction with bending/longitudinal vibration mode. Sensors and Actuators A: Physical. 2016;252:112–119. http://dx.doi.org/10.1016/j.sna.2016.10.039

10. Ippei Kono, Miyamoto T, Utsumi K, et al. Study on machining vibration suppression with multiple tuned mass dampers: vibration control for long fin machining. International Journal of Automation Technology. 2017;11:206–214. http://dx.doi.org/10.20965/ijat.2017.p0206

11. Kunugi K, Kojima H, Trivailo PM. Modeling of tape tether vibration and vibration sensing using smart film sensors. Acta Astronautica. 2015;107:97–111. http://dx.doi.org/10.1016/j.actaastro.2014.11.024

12. Legeza VP. Dynamics of vibration isolation system with a ball vibration absorber. International Applied Mechanics. 2018;54:584–593. http://dx.doi.org/10.1007/s10778-018-0912-0

13. Pavlov VD. Autocompensation of reactive power in electric networks. Journal of Siberian Federal University. Engineering & Technologies. 2021;14:684–688. http://elib.sfu-kras.ru/handle/2311/144270?show=full

14. Joachim FJ, Börner J, Kurz N. How to Minimize Power Losses in Transmissions, Axles and Steering Systems. Gear Technology. 2012. P. 58–66. https://doi.org/10.1007/978-3-642-22647-2_279

15. Pavlov VD. Mathematical models of resonance and antiresonance processes. Herald of the Ural State University of Railway Transport. 2021;49:17–27. https://doi.org/10.20291/2079-0392-2021-1-17-27

Received 21.01.2022
Revised 16.02.2022
Accepted 20.02.2022

About the Author:

Pavlov, Valentin D., Head of Scientific Information Department, Vladimir Electromechanical Plan (127, ul. Noyabr'skaya, Vladimir, 600901, RF), Cand.Sci. (Eng.), ORCID, pavlov.val.75@mail.ru

The author has read and approved the final manuscript.

MECHANICS

UDC 534.1:629.7
https://doi.org/10.23947/2687-1653-2022-22-1-30-41

Check for updates
Original article

Analytical solution to approximate equations of the launch vehicle motion under the gust action for the dynamic loading calculation

Olga I. Malykhina
Space Rocket Centre Progress JSC (Samara, Russian Federation)
maloliya@ya.ru

Introduction. The launch vehicle (LV) in flight and the dynamic components of loads from the impact of a trapezoidal wind gust are considered. It is proposed to determine the dynamic components of the force factors using analytical solutions for the structure points accelerations. The work objective is to create a technique for selecting the duration of the standard gust, under the influence of which maximum loads are provided in the sections of the LV structure.

Materials and Methods. The launch vehicle is presented as an uneven beam. The description of its vibrations is reduced to a system of independent ordinary differential equations that determine the motion of an equivalent system of oscillators. The equation of oscillator vibrations under the action of a trapezoidal pulse load is solved by the overlay method, and it is reduced to the calculation of the Duhamel integral. It is proposed to get the parameters of an equivalent system of oscillators based on the results of the calculation of dynamic characteristics for a finite element LV model in the Nastran program.

Results. Analytical relations for the LV structure point accelerations under the action of a trapezoidal wind gust are given. For the beam model, test calculations of accelerations were carried out according to the technique proposed in this paper. These data are compared to the results of finite element modeling. With the help of analytical solutions, dependences are constructed that determine the nature of the change in the magnitude of the bending moment for different sections of the launch vehicle when the duration of the wind gust varies.

Discussion and Conclusions. The presented technique provides building an equivalent dynamic model of systems with a large number of degrees of freedom on the example of a LV and obtaining analytical solutions for accelerations of points of a mechanical system under trapezoidal external action. These solutions are applicable for the study of dynamic loads. The analysis results enable to select the duration of the wind gust, at which maximum loads are reached in the sections of the LV structure. Calculations based on the analytical solutions are very economical in terms of time spent. They can be used in design calculations for preliminary assessment of loading.

Keywords: launch vehicle, beam model, oscillator, structure loads, Duhamel integral, dynamic loads, gust, analytical solutions, differential equation, vibrations, bending moment.

For citation: O. I. Malykhina. Analytical solution to approximate equations of the launch vehicle motion under the gust action for the dynamic loading calculation. Advanced Engineering Research, 2022, vol. 22, no. 1, pp. 30–41. (In Russ). https://doi.org/10.23947/2687-1653-2022-22-1-30-41

Introduction. During the operation of the launch vehicle (LV), loads occur in the elements of its design. We are talking about longitudinal and shear forces, bending and torsion moments. Data on these force factors are used for strength analysis in the design of new products, experimental development of the design [1], and adaptation of launch vehicles for a specific start-up [2]. Loads are divided into quasi-static and dynamic. The quasi-static ones arising in flight are calculated from the condition of dynamic equilibrium of the LV as a solid body, taking into account the permissible parameters of the ascent trajectory.

Generalized beam models are usually used to calculate dynamic loads. Such loads are determined by the results of solving the equation of the elastic LV motion, which in general is a partial differential equation. Methods based on the application of decomposition of the solution by the eigenvibration tones of the structure are able to provide a high speed of calculation in combination with sufficient accuracy of the results [3]. As shown in [4], using the method of decomposition by the forms of natural oscillations, it is possible to proceed to a system of independent ordinary differential equations. They describe:

— centroidal motion of the LV,

— rotation of the longitudinal axis of the LV relative to the center of mass,

— transverse elastic modes of the LV in flight.

The transition to independent equations describing elastic modes of the LV means that the distributed parameters of oscillators will be taken into account, each of which is a single-degree-of-freedom system. The motion of such an oscillator can be considered independently of the others, and a solution can be obtained for each of them using well-known methods of oscillation theory.

To calculate the loads in flight, not the entire ascent trajectory is considered, but only some of its points, the so-called load cases, characterized by the extreme value of individual parameters affecting loading, or the maximum value of loads on individual structural elements. One of the most important cases of loading is the atmospheric flight of the LV [1, 5]. The influence of a turbulent atmosphere on the LV loading can be determined by statistical methods [6, 7], or within the framework of a conservative approach, when the maximum possible (with some level of probability) wind characteristics are taken into account. This paper discusses the second approach. A single specified wind gust is accepted as an external dynamic effect. The profile of the specified gust, which characterizes the change in wind speed over time, can be set in a trapezoidal [8], cosine, or sinusoidal form [9]. In this paper, we will consider the launch vehicle motion under the trapezoidal gust action. The duration of the specified gust is usually selected to be comparable with the period of the lowest transverse tone of the LV[1] vibrations. At the same time, there are often demands for its variation to achieve maximum efforts in the LV sections [8, 10]. The complexity of calculations using standard finite element (FE) analysis programs is due to:

— the need to vary the parameters of external action,

— a large number of calculated cases,

— a variety of design options and configurations of structures at the stage of design calculations [9].

This paper objective is to develop a methodology for selecting the duration of the specified gust using analytical solutions obtained for a simplified dynamic LV model presented as an equivalent system of oscillators.

A semi-analytical approach using the Duhamel integral was successfully applied in [11] for hydroelastic analysis of ships. In [12] and a number of other works, the Duhamel integral is used as part of the problem solution of loading bridges with moving loads. In this paper, the Duhamel integral is used for analytical solutions to the LV reaction to the short-term impact of a wind gust in flight.

Materials and Methods. At the stages of preliminary design, it is advisable to use flat design schemes for beam models. With the simplicity and speed of the solution, they enable to determine the motion variables and internal forces (with an accuracy acceptable for this stage of design) [13]. Imagine the LV in the form of an elastic beam with variable length mass and stiffness. Assume the usual assumptions for the resistance of materials, including the hypothesis for the smallness of elastic deformations. To determine the internal force factors in the LV section, we use the acceleration (overload) method [1, 4], which can be interpreted as a cross-section method adapted for dynamic calculation. In this case, internal forces are found from the conditions of static equilibrium of mentally cut off parts of the structure under the action of external distributed loads, supplemented by D'Alembert's forces of inertia, and the desired internal forces. Quasi-static and dynamic values of force factors are determined separately based on pre-calculated accelerations, and then summed up [4].

This paper considers the issue of determining the dynamic loading of the LV in the transverse direction under the action of a wind gust, whose speed is directed perpendicular to the longitudinal axis of the LV. It is assumed that the loading in the longitudinal direction can be calculated independently. It is not considered in this paper.

To determine dynamic accelerations, the LV is presented as a free elastic beam. Its motion is studied in the vicinity of the moment of time corresponding to the load case under consideration, and is described in deviations from the state of dynamic equilibrium in which the LV was before the wind gust, moving along the nominal (undisturbed) trajectory. Here, such parameters as the mass and moment of inertia of the LV, the motor power, and the angle of projection are assumed to be constant and equal to the characteristics of the considered point of the nominal trajectory. The perturbed motion of the elastic LV is investigated in a fixed coordinate system associated with the position that the LV occupied at the time of the calculation. The perturbed motion will be a combination of plane-parallel motion of the LV as a rigid body in the plane in which the dynamic load is applied, and elastic modes of the structure. We do not take

[1]Likhoded AI. Dinamika konstruktsii i opredelenie nagruzok. Korolev: Izd-vo AO TSNIImash; 2020. 239 p. (In Russ.)

into account the control system response, i.e., for the stabilization machine, we assume a long delay time compared to the time of application of the dynamic load. In general, under the influence of a wind gust, together with elastic modes of the body, the LV starts to move as a rigid body. The transverse component of the aerodynamic force, which is considered proportional to it at a small angle of attack, changes its value due to the displacement of the structure in the direction of the wind gust and rotation relative to the forward flow vector. The projection of gravity on the transverse axis of the LV also changes. To properly account for these changes, the equations of LV motion must be integrated with the equations describing the logic of the automatic stabilization, which is impossible at the early stages of design. Taking into account the significant mass and the moment of inertia of the LV, we will consider small:

— the angle of rotation of the LV as a rigid body for the time of calculation;

— the rate of displacement of the LV center of mass in the direction of the wind.

This enables to ignore the impact of the above changes. The angle-of-attack increment (and, consequently, the transverse component of the aerodynamic force) is considered to depend only on the magnitude of the wind gust speed given as a function of time. Thus, taking into account the accepted assumptions, the aerodynamic load in the transverse direction is a load distributed along the length of the beam with a time-dependent proportionality coefficient. The law of distribution of aerodynamic load along the length of the LV is determined experimentally and is considered to be known in advance. The law of change of the proportionality coefficient (angle of attack) from time to time is determined by the selection of the profile of the specified wind gust.

The motion of the LV modeled as an elastic beam can be described using the well-known equation of forced transverse vibrations of the beam, written with the account for Voigt's hypothesis:

$$m(x)\frac{\partial^2 y(x,t)}{\partial t^2}+\left(1+h\frac{\partial}{\partial t}\right)\frac{\partial^2}{\partial x^2}\left[B(x)\frac{\partial^2 y(x,t)}{\partial x^2}\right]=q(x,t), \quad (1)$$

where $m(x)$ — mass per unit length; $B(x)$ — bending stiffness; $q(x,t)$ — distributed external load; h — friction factor.

This equation should be supplemented with a boundary condition: the internal forces in the initial and final sections are zero. It means:

$$\frac{\partial}{\partial x}\left[B(x)\frac{\partial^2 y(x,t)}{\partial x^2}\right]=0,\ B(x)\frac{\partial^2 y(x,t)}{\partial x^2}=0,\ \text{при } x=0, x=L, \quad (2)$$

where L — the LV length.

In this paper, the aerodynamic force is taken as an external distributed load, which can be presented as a product of functions:

$$q(x,t)=R(t)Y_a(x), \quad (3)$$

where $R(t)$ — the function that determines the temporal variability of the aerodynamic force and varies according to the trapezoidal law in accordance with the wind gust model adopted in this paper; $Y_a(x)$ — the function of the aerodynamic force distribution along the LV length.

Let us consider free LV vibrations without taking into account friction forces (at $q(x,t)=0,\ h=0$). We substitute the variable separation method $y(x,t)=f(x)\cdot q(t)$. In this case, from equation (1) with boundary conditions (2), it is possible to arrive at an ordinary differential equation

$$\frac{\mathrm{d}^2}{\mathrm{d}x^2}\left[B(x)\frac{\mathrm{d}^2 f(x)}{\mathrm{d}x^2}\right]-p^2 m(x)f(x)=0, \quad (4)$$

with boundary conditions:

$$\frac{\mathrm{d}}{\mathrm{d}x}\left[B(x)\frac{\mathrm{d}^2 f(x)}{\mathrm{d}x^2}\right]=0,\ B(x)\frac{\mathrm{d}^2 f(x)}{\mathrm{d}x^2}=0,\ \text{при } x=0, x=L. \quad (5)$$

Solution (4) with conditions (5) is a classical Sturm-Liouville problem. Solving it, one can find a set of eigenforms $f_j(x)$ and eigenfrequencies p_j of the beam in question $(j=1,2,\ldots)$. It is known[2] that some solutions to system (4) correspond to zero natural frequencies. The forms corresponding to zero natural frequencies determine the translational motion of the LV as a rigid body together with the center of mass and rotation around the center of mass: $f_{-1}=1, f_0=x-x_C$, where x_C — coordinate of the LV center of mass.

It should be noted that the LV mass and stiffness characteristics most often have a piecewise constant pattern of distribution. In this case, the equations of form (1) and (4) should be written separately for each homogeneous beam section with boundary conditions at the junctions of the sections, as in the derivation of the ratios of the initial parameters method [1, 14]. In the given paper, this entry is omitted, because the calculation of the dynamic characteristics (modal analysis) of structures is carried out numerically, using the finite element method.

Let us imagine the forced vibrations of an elastic beam modeling the LV structure in the form of decomposition according to the natural modes. Assume that the beam stiffness axis passes through its center of mass.

[2] Kolesnikov KS. Dinamika raket. Moscow: Mashinostroenie; 2003. 520 p. (In Russ.)

To move the points of the LV axis, we write:

$$y(x,t) = y_C(t) + \vartheta(t)(x - x_C) + \sum_{j=1}^{N} f_j(x)\cdot q_j(t), \quad (6)$$

where $y_C(t)$ — displacement of the beam center of mass; $\vartheta(t)$ — angle of rotation of the axis of the undeformed beam; f_j — beam eigenmode corresponding to tone numbered j; $q_j(t)$ — generalized coordinate corresponding to tone numbered j; N — number of elastic tones taken into account.

After substituting (6) into (1) and applying the Bubnov-Galerkin procedure, we can arrive at an ordinary differential system with constant coefficients:

$$m\ddot{y}_C(t) = Q_y,$$
$$I\ddot{\vartheta}(t) = Q_\vartheta, \quad (7)$$
$$m_j\big(\ddot{q}_j(t) + 2n_j\dot{q}_j(t) + p_j^2 q_j(t)\big) = Q_j(t) \;\; (j = 1, 2, \ldots, \mathrm{N})$$

Here, m — LV mass; I — moment of inertia relative to the axis passing through the LV center of mass perpendicular to the plane of rotation; m_j — reduced (generalized) mass for the j-th vibration tone and determined from the formula: $m_j = \int_0^L m(x) f_j^2(x)\,dx$.

The generalized forces in expression (7), taking into account (3), are defined as follows:

$$Q_y = R(t)\int_0^L Y_a(x)\,dx = R(t)Q_a, \quad (8)$$

$$Q_\vartheta = R(t)\int_0^L Y_a(x)\,(x - x_C)dx = R(t)M_a, \quad (9)$$

$$Q_j = R(t)\int_0^L Y_a(x)\,f_j dx = R(t)Q_{0j}. \quad (10)$$

Here, Q_a — maximum value of the main transverse aerodynamic load vector; M_a — maximum value of the main transverse aerodynamic moment reduced to the LV center of mass; Q_{0j} — maximum value of the generalized force corresponding to the generalized coordinate q_j.

The first two equations in (7) define the law of change of accelerations of the LV points in the process of translational and rotational motion of the LV as a rigid body. The last equation in (7) defines the law of motion of an equivalent system of oscillators.

Consider the motion of one oscillator under the action of a trapezoidal external load, which:

— increases from zero to Q_0 over time δ,

— maintains a constant value over time θ,

— drops to zero over time δ.

For convenience, we omit the indices characterizing the tone number. Then we will rewrite the differential equation of the oscillator motion taking into account (10) in the form:

$$\ddot{q} + 2n\dot{q} + p^2 q = \frac{Q(t)}{m} = \frac{Q_0}{m}R(t), \quad (11)$$

where m — oscillator mass; p — angular frequency of natural oscillations, expressed in radians per second; n — damping coefficient (determines the oscillator damping); $Q(t) = Q_0 R(t)$ — law of variation of external load.

We represent function $R(t)$ as a set of four linear functions:

$$R_1(t) = \delta^{-1}t, \qquad R_2(t) = -\delta^{-1}(t - \delta),$$
$$R_3(t) = -\delta^{-1}(t - \delta - \theta), R_4(t) = \delta^{-1}(t - 2\delta - \theta).$$

Accordingly, external load $Q(t)$ is a combination of four linear loads $Q_i(t) = Q_0 R_i(t), (i = 1, 2, 3, 4)$. Load $Q_1(t)$ is applied from moment $t = 0$; $Q_2(t)$ — from moment $t = \delta$; $Q_3(t)$ — from moment $t = \theta + \delta$; $Q_4(t)$ — from moment $t = \theta + 2\delta$.

To determine the system response to external actions, we divide the entire duration of the load into four intervals (Fig. 1).

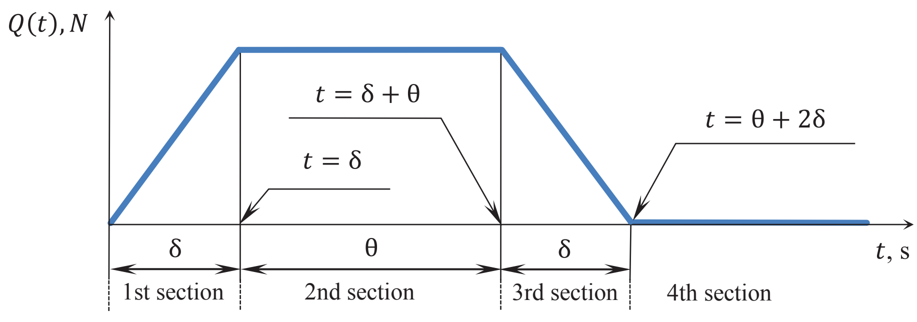

Fig. 1. Diagram of the external trapezoidal load

In accordance with the superimposition method[3], let us represent the response of the linear system under consideration to an external action in the form of the Duhamel's integral as the sum of responses to a set of independently applied elementary impulses:

$$q(t) = \int_0^t P(t-\vartheta)Y(\vartheta)d\vartheta,$$

Here, $P(t-\vartheta)$ — the shifted time law of variation of external action, and $Y(\vartheta)$ characterizes the system response to a unit impulse input. The response of mechanical system $q_l(t)$ to a linearly increasing load $P(t) = kt$ can be expressed through the system response to unit impulse $Y(\vartheta)$ and to a suddenly applied single load $Y_1(\vartheta)$:

$$q_l(t) = k\int_0^t Y_1(\vartheta)d\vartheta, \qquad Y_1(t) = \int_0^t Y(\vartheta)d\vartheta.$$

The response of a one-degree-of-freedom mechanical system with damping coefficient n to a unit pulse will have the form[4]:

$$Y(\vartheta) = \frac{1}{m\sqrt{p^2-n^2}}e^{-n\vartheta}\sin\left(\sqrt{p^2-n^2}\vartheta\right).$$

We introduce a notation for the frequency of damped vibrations $p_1 = \sqrt{p^2-n^2}$. Let us calculate the system response to a suddenly applied unit load:

$$Y_1(\vartheta) = \int_0^t Y(\vartheta)d\vartheta = \frac{1}{mp^2}\left[1 - e^{-nt}\left(\cos(p_1t) + \frac{n}{p_1}\sin(p_1t)\right)\right].$$

The response to a linearly increasing load:

$$q_l(t) = k\int_0^t Y_1(\vartheta)d\vartheta = \frac{k}{mp^2}\left\{\frac{2n}{p^2}[-1 + e^{-nt}\cos(p_1t)] + \frac{1}{p_1}\left(\frac{2n^2}{p^2} - 1\right)e^{-nt}\sin(p_1t) + t\right\}. \quad (12)$$

We accept the notations: $\Delta_1 = t - \delta, \Delta_2 = \Delta_1 - \theta, \Delta_3 = \Delta_2 - \delta$.

We introduce a function containing the harmonic terms of solution (12):

$$d(\vartheta) = 2\frac{n}{p^2}\left(\cos(p_1\cdot\vartheta) + \frac{n}{p_1}\sin(p_1\cdot\vartheta)\right)e^{-n\vartheta} - \frac{1}{p_1}\sin(p_1\cdot\vartheta)\,e^{-n\vartheta}.$$

We denote by $q_{\text{ст}}$ the motion under the action of a force statically applied to the system $Q_0 = q_{\text{ст}}mp^2$ and take into account that $k = Q_0/\delta$. The total movement of the oscillator under the action of a combination of loads $Q_i(t)$ at every time point will be the sum of the corresponding solutions (12). The system response described by equation (11) to the external impact of the trapezoidal profile will have the form:

$$q(t) = \begin{cases} q_{\text{ст}}\delta^{-1}[d(t) - 2n/p^2 + t] & at\ 0 \le t < \delta, \\ q_{\text{ст}}\delta^{-1}[d(t) - d(\Delta_1) + \delta] & at\ \delta \le t < \theta + \delta, \\ q_{\text{ст}}\delta^{-1}[d(t) - d(\Delta_1) - d(\Delta_2) + 2n/p^2 - \Delta_3] & at\ \theta + \delta \le t < \theta + 2\delta, \\ q_{\text{ст}}\delta^{-1}\left(d(t) - d(\Delta_1) - d(\Delta_2) + d(\Delta_3)\right) & at\ t \ge \theta + 2\delta. \end{cases} \quad (13)$$

The law of variation of the oscillator accelerations can be obtained from double differentiation in time of expression (13). Let us introduce function $g(\vartheta) = \frac{d^2}{d\vartheta^2}\left(d(\vartheta)\right)$. We differentiate and record the result taking into account the number of the oscillation tone:

$$g_j(\vartheta) = \left[(n_j^2 - p_{1\,j}^2)\left(2\frac{n_j}{p_j^2}\left(\cos(p_{1\,j}\cdot\vartheta) + \frac{n_j}{p_{1\,j}}\sin(p_{1\,j}\cdot\vartheta)\right) - \frac{1}{p_{1\,j}}\sin(p_{1\,j}\cdot\vartheta)\right) -\right.$$

[3] Biderman VL. Teoriya mekhanicheskikh kolebanii. Moscow: URSS; 2017. 416 p. (In Russ.)

[4] Yablonskii AA. Kurs teoreticheskoi mekhaniki. Moscow: Integral-Press; 2007. 603 p. (In Russ.)

$$-2n_j\left(2\frac{n_j}{p_j^2}\left(-p_{1\,j}\sin\left(p_{1\,j}\cdot\vartheta\right)+n_j\cos\left(p_{1\,j}\cdot\vartheta\right)\right)-\cos\left(p_{1\,j}\cdot\vartheta\right)\right)\Big]e^{-n\vartheta}. \tag{14}$$

We rewrite the expression for the frequency of damped natural vibrations:

$$p_{1\,j}=\sqrt{p_j^2-n_j^2}. \tag{15}$$

To determine the accelerations of the LV points, we differentiate twice (6):

$$\ddot{y}(t,x)=\ddot{y}_C(t)+\ddot{\vartheta}(t)(x-x_C)+\textstyle\sum_{j=1}^{N}f_j(x)\ddot{q}_j(t). \tag{16}$$

Let us express the accelerations of the generalized coordinates from the first two equations of system (7) taking into account (8) and (9). We represent the accelerations of the points of the LV axis that it acquires through moving as a rigid body:

$$a(t)=\ddot{y}_C(t)+\ddot{\vartheta}(t)(x-x_C)=R(t)(Q_a/m+M_a/I). \tag{17}$$

In addition, we take into account the law of variation of function $R(t)$ from time:

$$R(t)=\begin{cases}\delta^{-1}t & at\ 0\le t<\delta,\\ 1 & at\ \delta\le t<\theta+\delta,\\ -\delta^{-1}(t-\ 2\delta-\theta) & at\ \theta+\delta\le t<\theta+2\delta,\\ 0 & at\ t\ge\theta+2\delta.\end{cases}$$

We get:

$$a(t)=\begin{cases}\delta^{-1}t(Q_a/m+M_a/I) & at\ 0\le t<\delta,\\ Q_a/m+M_a/I & at\ \delta\le t<\theta+\delta,\\ -\delta^{-1}(t-\ 2\delta-\theta)(Q_a/m+M_a/I) & at\ \theta+\delta\le t<\theta+2\delta,\\ 0 & at\ t\ge\theta+2\delta.\end{cases} \tag{18}$$

For accelerations of generalized coordinates corresponding to the elastic vibration tones, as a result of double differentiation of expression (13), taking into account (14), we obtain:

$$\ddot{q}_j(t)=\begin{cases}\delta^{-1}q_{\text{ст}\,j}g_j(t) & at\ 0\le t<\delta,\\ \delta^{-1}q_{\text{ст}\,j}\left(g_j(t)-g_j(\Delta_1)\right) & at\ \delta\le t<\theta+\delta,\\ \delta^{-1}q_{\text{ст}\,j}\left(g_j(t)-g_j(\Delta_1)-g_j(\Delta_2)\right) & at\ \theta+\delta\le t<\theta+2\delta,\\ \delta^{-1}q_{\text{ст}\,j}\left(g_j(t)-g_j(\Delta_1)-g_j(\Delta_2)+g_j(\Delta_3)\right) & at\ t\ge\theta+2\delta.\end{cases} \tag{19}$$

Taking into account (16) and (17), the law of variation in the accelerations of the elastic LV axis points under the action of a trapezoidal wind gust will have the form:

$$\ddot{y}(t,x)=a(t)+\textstyle\sum_{j=1}^{N}f_j(x)\ddot{q}_j(t), \tag{20}$$

where $a(t)$ is determined from expression (18), $\ddot{q}_j(t)$ — from expression (19).

While investigating the LV elastic modes, damping is traditionally taken on the basis of the data obtained from the results of full-scale dynamic tests and presented in the form of values of logarithmic decrements D_j. Then, the coefficient determining the damping parameter and included in expressions (14) and (15) can be calculated from formula:

$$n_j=\frac{D_j}{2\pi}p_j. \tag{21}$$

The change in generalized coordinate q_j included in formula (19) under the action of a statically applied generalized force Q_{0j} is determined from expression:

$$q_{\text{ст}\,j}=\frac{1}{p_j^2}\frac{Q_{0j}}{m_j}=\frac{1}{p_j^2}\frac{\int_0^L Y_a(x)f_j(x)\,dx}{\int_0^L m(x)f_j^2(x)\,dx}. \tag{22}$$

Taking into account (14), (15), (18), (19), (21), (22), formula (20) is an analytical expression that defines the functions of the acceleration change over time for the points of the LV axis under the action of an external transverse aerodynamic force varying according to the trapezoidal law, taking into account the impact of dissipative forces.

Knowing the law of acceleration variation, it is possible to determine the dynamic, and then the total structure loads acting in the LV sections using the known methods [4]. We calculate the bending moment due to inertial forces from the elastic modes of the LV structure:

$$M(x,t) = -\sum_{j=1}^{N} M_j(x)\ddot{q}_j(t). \tag{23}$$

Here, $M_j(x)$ — function of distributing a unit (with acceleration $\ddot{q}_j(t)$, equal to one) bending moment for the j-th vibration tone along the LV length. It can be found from formula:

$$M_j(x) = \int_0^x \int_0^x m(x) f_j(x) dx\, dx. \tag{24}$$

As noted above, for the modal analysis in this work, the FE method was used. This approach is due to the fact that in practice, the dynamic LV model has rather complicated structure. It includes substructures, and their own dynamics cannot be neglected. Substructures can be attached to the LV body in one section, or be located parallel to the longitudinal axis of the LV and have several attachment points. In this case, the calculation of dynamic characteristics in a continuum setting is a complex mathematical problem. In addition, dynamic models of individual substructures are presented by development companies in a condensed (matrix) form in the Nastran format. For this reason, it will be optimal to use the Nastran engineering analysis software package to calculate the dynamic characteristics of the structure.

However, the use of standard FE analysis programs for the calculation of dynamic loading is fraught with certain difficulties. These include the need to pre-construct an equivalent model of the external aerodynamic load suitable for use in the FE analysis program [15], which in itself is quite difficult. In addition, there are difficulties associated with processing the calculation results. The use of the postprocessor functionality for analyzing the results is extremely time-consuming and requires a large number of manual operations. Another way involves the application of additional software for processing large array of numeric data[5]. In this paper, an approach is proposed in which the FE analysis program is used only for modal analysis. In this case, dynamic loading is calculated using specially developed software that allows you to vary external loads and automatically process the calculation results.

For a complex LV design, equations (7) retain their form [3]. The standard output information of the Nastran program can be the basis for obtaining the parameters of an equivalent system of oscillators, LV mass and moment of inertia, as well as for calculating the generalized forces included in the third equation of system (7). To form the left side of the third equation in (7), the values of natural frequencies p_j (Radians) and generalized masses m_j (Generalized mass) are required. To determine the generalized forces in the right part of the third equation in (7), the eigenmode functions $f_j(x)$ (Eigenvector) are needed. When calculating dynamic inertial loads according to (23), instead of (24), it is more convenient to use unit inertial loads (forces and moments), which are output by the Nastran program after the standard application of forces when calculating eigenforms and frequencies. Unit inertial loads are output separately for each vibration tone and multiplied by the square of the natural frequency, which should be taken into account for their correct use.

Research Results. To carry out test calculations, a medium class tandem launcher is considered. Figure 2 shows the type of functions of linear bending stiffness $B(x)$ and mass $m(x)$, as well as the distribution of concentrated masses $m_{\text{сосp}}(x) = m_{\text{сосp}_r}\Delta(x - x_r)$ along the length of the considered LV (the Dirac delta function is denoted by Δ).

[5] Malykhina OI. Avtomatizatsiya obrabotki rezul'tatov konechnoehlementnogo analiza nagruzheniya konstruktsii raketno-kosmicheskoi tekhniki. In: Proc. VII Sci.-Tech. Postdoctoral Conf., Mission Control Center. Korolev: TSNIIMash; 2017. P. 427–434. (In Russ.)

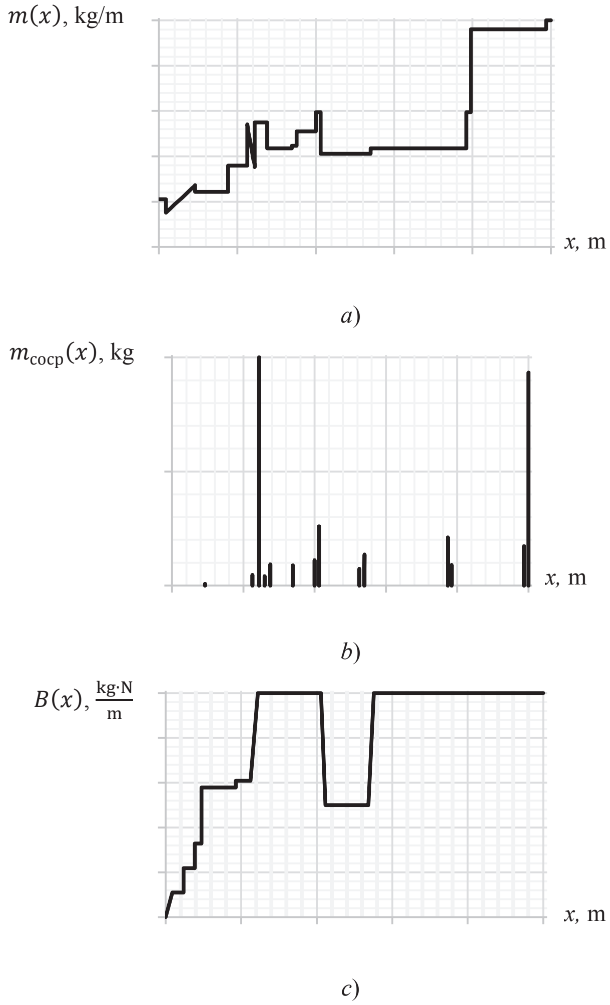

Fig. 2. Distribution of mass and stiffness characteristics along the LV length:
linear mass (a), concentrated mass (b), bending stiffness (c)

To check the obtained analytical solutions under the impact of a trapezoidal external load, the dynamic LV accelerations are calculated according to formula (20), taking into account (14), (15), (18), (19), (21), (22). At the same time, 5 elastic tones of natural transverse LV vibrations are considered. Characteristics p_j, m_j and $f_j(x)$ were obtained from the calculation results in the MSC Nastran software package using the solution sequence for modal analysis of natural vibrations (SOL 103). The LV dynamic finite element model is presented as a set of beam elements with various inertial and stiffness characteristics. The following elements are elastically or rigidly attached to the beam elements:

— elements describing the inertial properties of devices, aggregates, parts of the block structure;

— condensed models of individual blocks presented in the digital matrix form.

The finite element LV model includes about 1000 components. The elements simulating restraints were not used to preserve the ability of the LV to move as a rigid body.

According to the same finite element LV model in the MSC Nastran software package, the accelerations are calculated through the SOL 119 solution sequence used for modal transient analysis. At the same time, all tones of natural vibrations in the range up to 100 Hz were taken into account in the modal decomposition. The aerodynamic load is represented by transverse linear loads distributed over all beam elements simulating the LV structure. In addition, the trapezoidal law of the aerodynamic load variation over time is given.

Figure 3 shows the results of a comparative analysis of accelerations obtained using two different approaches $a_0(t) = \ddot{y}(t, x_0)$ of a certain point of the LV axis with coordinate $x = x_0$. It can be seen that the following two solutions agree well:

— the solution obtained for accelerations using a simplified LV model based on the analytical relations given in this paper;

— numerical solution obtained from the complete finite element LV model.

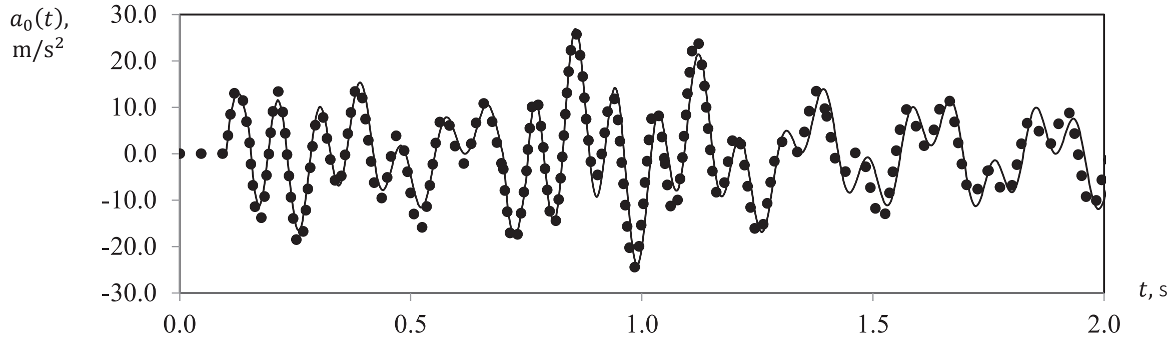

Fig. 3. Comparison of transverse accelerations obtained through two different approaches: ——— — finite element modeling, ••••• — analytical solution for a simplified model

The peak value of the bending moment selected from the time process determines the level of equivalent forces taken to carry out the strength calculation, and acts as a variable parameter when changing the parameters of external action in the transverse direction [16].

Dependences are obtained based on the values of dynamic accelerations (Fig. 4). They show how the change in peak bending moment M or different LV sections are related to parameter θ, which characterizes the gust duration. In Figure 4, the bending moment values are presented in the form of dimensionless quantities M^*. They are calculated through dividing the dimensional bending moment by the maximum value for a given section (e.g., for section $x = 0.3L$ maximum value $M_{max} = 4.6 \cdot 10^5$ N · m), found when value θ varies over the entire range under consideration.

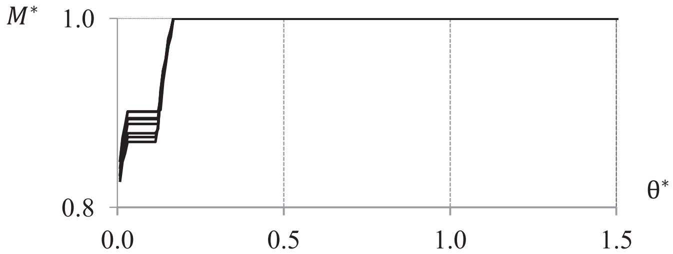

a)

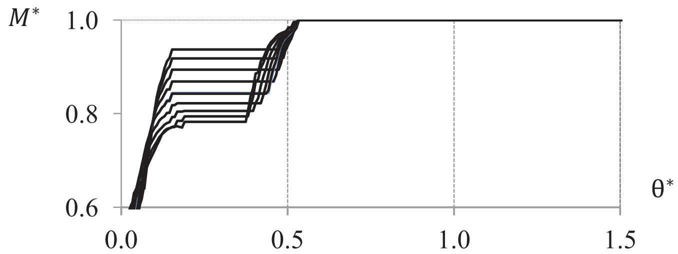

b)

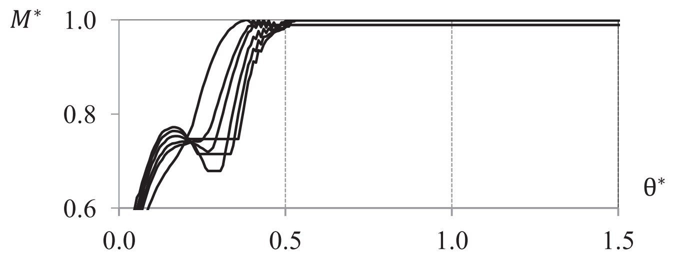

c)

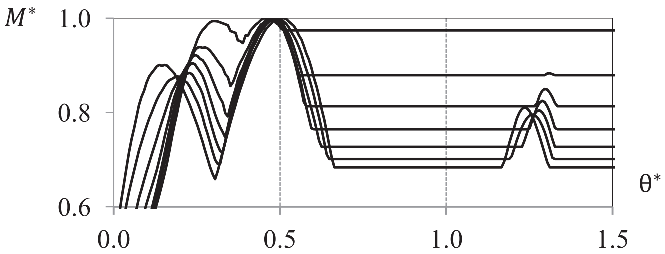

d)

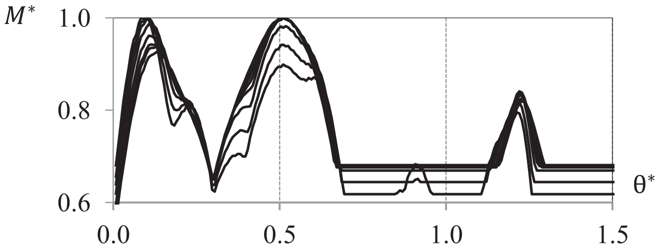

e)

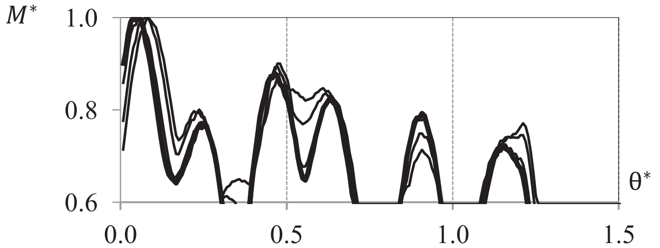

f)

Fig. 4. Dependence of the value of dimensionless bending moment M^* on the duration of wind gust θ*, expressed in fractions of period T_1 for various LV sections: zone 1 ($x = 0.0 - 0.2L$) (*a*); zone 2 ($x = 0.2L - 0.4L$) (*b*); zone 3 ($x = 0.4L - 0.55L$) (*c*); zone 4 ($x = 0.55L - 0.75L$) (*d*); zone 5 ($x = 0.75L - 0.9L$) (*e*); zone 6 ($x = 0.9L - L$) (*f*)

So, on the graphs, the duration of the gust action is represented by dimensionless value θ* obtained through dividing parameter θ by period T_1 of the first tone of the LV vibrations. Each line of the graph corresponds to one section of the LV. All LV sections are grouped according to the nature of function $M^*(\theta^*)$ and are shown on various graphs, and the LV length is appropriately divided into zones (Fig. 5).

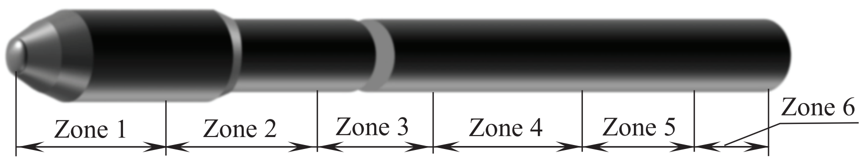

Fig. 5. LV cross-section zones

It can be seen from Figure 4 that for the first zone, the maximum bending moment is reached already at θ values at least 15% of period T_1 of the first vibration tone. For the second and third zones — slightly more than half of period T_1. A further increase in θ values does not affect the magnitudes of the maximum values of the bending moment. For zones 4-6, the maximum value of the bending moment turns out to be local and is within the zone of θ values close to the value of half of period T_1 of the first tone of the LV vibrations. The results obtained fully correspond to the results of finite element modeling carried out earlier[6].

[6] Malykhina OI, Glugovskii MS. Analiz vliyaniya profilya poryva vetra na velichinu korpusnykh nagruzok rakety-nositelya v poletnykh sluchayakh nagruzheniya. In: Proc. VI All-Russian Sci.-Tech. Conf. Samara. 2019;1:133–138. (In Russ.)

Thus, to obtain the maximum values of the bending moment in the sections of the considered LV, a dynamic analysis of the behavior of the structure with external action in the form of a wind gust of is required. Its duration is determined by parameter θ, close in value to half of the period of the first tone of the LV vibrations.

Discussion and Conclusions. Using the superposition method, analytical solutions are obtained that describe the motion of a one-degree-of-freedom system, which is affected by the friction force and an external force varying according to the trapezoidal law. The method of application of the obtained analytical solutions for systems with many degrees of freedom is given. A good coincidence of two types of solutions is shown:

— analytical one, for accelerations of LV points found from a simplified model;

— numerical data obtained from the complete finite element LV model.

It is shown that analytical solutions can be used to analyze dynamic force factors to select the duration of a wind gust, under the impact of which maximum loads are achieved in the sections of the LV structure. Similarly, it is possible to analyze the overloads that are achieved in the LV sections (e.g., at the installation points of measurement systems).

In addition, the proposed methodology provides building a full cycle of the load analysis pre-calculation in the case when an analytical representation of the external dynamic load is possible. The load analysis based on analytical solutions is very economical in terms of calculation time, and it can be a remarkable alternative to finite element modeling at the design stage, when a large number of combinations of external loads and configurations of the design under development are studied. Finite element analysis of the detailed model in this case can be used as a refine final calculation.

References

1. Karmishin AV, Likhoded AI, Panichkin NG, et al. Osnovy otrabotki prochnosti raketno-kosmicheskikh konstruktsii. Moscow: Mashinostroenie; 2007. 480 p. (In Russ.)

2. Johnson DL, Vaughan WW. The Role of Terrestrial and Space Environments in Launch Vehicle Development. Journal of Aerospace Technology and Management. 2019;11:e4719. https://doi.org/10.5028/jatm.v11.1088

3. Anisimov AV, Zolkin SN, Likhoded AI, et al. About Specific Features of Load Calculations for Structures with Variable Mass-Inertia Characteristics. Cosmonautics and Rocket Engineering. 2012;67:120–128.

4. Gladkii VF. Dinamika konstruktsii letatel'nogo apparata. Moscow: Nauka; 1969. 495 p. (In Russ.)

5. Suresh BN, Sivan K. Aerodynamics of Launch Vehicles. In book: Integrated Design for Space Transportation System. New Delhi: Springer; 2015. P. 391–454. http://dx.doi.org/10.1007/978-81-322-2532-4_10

6. Clark JB, Kim JB, Kabe AM. Statistical Analysis of Atmospheric Flight Gust Loads Analysis Data. Journal of Spacecraft and Rockets. 2000;37:443–445. https://doi.org/10.2514/2.3602

7. Kim MC, Kabe AM, Lee SS. Atmospheric Flight Gust Loads Analysis. Journal of Spacecraft and Rockets. 2000;37:446–452. https://doi.org/10.2514/2.3603

8. Mastroddi F, Stella F, Cantiani D, et al. Linearized Aeroelastic Gust Response Analysis of a Launch Vehicle. Journal of Spacecraft and Rockets. 2011;48:420–432. https://doi.org/10.2514/1.47268

9. Jayasidhan AK, Rose J, Neetha R. Dynamic Response of a Launch Vehicle to Wind Gust. International Journal of Engineering Development and Research (IJEDR). 2015;3:1–6.

10. Zolkin SN. Investigation of heavy launch vehicle loading while moving in the dense atmosphere. Trudy MAI. 2011;45:1–12.

11. Sengupta D, Datta R, Sen D. A simplified model for hydroelasticity of containerships. Journal of Engineering Mathematics. 2021;129:1–30. https://doi.org/10.1007/s10665-021-10142-2

12. Ziru Xiang, Tommy Chan, David Thambiratnam, et al. Synergic identification of prestress force and moving load on prestressed concrete beam based on virtual distortion method. Smart Structures and Systems. 2016;17:917–933. http://dx.doi.org/10.12989/sss.2016.17.6.917

13. Aleksandrov AA, Dragoon DK, Zabegaev AI. The mechanics of container rocket launch with the effect of lateral loads. Engineering Journal: Science and Innovation. 2013;15:1–10.

14. Kirilin AN, Akhmetov RN, Sollogub AV. Proektirovanie, dinamika i ustoichivost' dvizheniya raket-nositelei. Metody, modeli, algoritmy, programmy v srede MathCad. Moscow: Mashinostroenie; 2013. 296 p. (In Russ.)

15. Johnson DL, Vaughan WW. The Wind Environment Interactions Relative to Launch Vehicle Design. Journal of Aerospace Technology and Management. 2020;12:e0220. http://dx.doi.org/10.5028/jatm.v12.1090

16. Titov AV. Assessment of efforts of quasi-static bending of launch vehicle structure on loads in maximum dynamic pressure passage zone. Cosmonautics and Rocket Engineering. 2013;70:76–82.

Received 24.12.2021

Revised 17.01.2022

Accepted 23.01.2022

About the Author:

Malykhina, Olga I., design engineer of the first category, Space Rocket Centre Progress JSC (18, Zemetsa St., Samara, 443009, RF), ORCID, maloliya@ya.ru.

The author has read and approved the final manuscript.

MACHINE BUILDING AND MACHINE SCIENCE

Check for updates

UDC 621.7
https://doi.org/10.23947/2687-1653-2022-22-1-42-49

Original article

The finishing and cleaning of long parts in screw rotors

Valery A. Lebedev[1], **Luay Mohammed Rajab Al-Obaidi**[1,2], **Nikolay S. Koval**[1]

[1]Don State Technical University (Rostov-on-Don, Russian Federation)

[2]Middle Technical University, Institute of Technology-Baghdad (Baghdad, Iraq)

Introduction. To search for effective methods of finishing and stripping of long-length parts, it is advisable to create a rotary-screw process system of a pass-through type. Its main working element is a screw rotor, which is a combination of flat elements of various shapes and sizes, multidirectional with respect to the helical lines around the perimeter. The purpose of this study is to justify the intensity of the machining process in devices equipped with a screw rotor.

Materials and Methods. Metal removal is accepted as the main parameter determining the intensity of the machining process in screw rotors. Within the framework of the presented study, processing was performed on an experimental rotary-screw installation. The processing medium consisted of molded abrasive pellets of the PT 10x10 brand. The research conditions were as follows: loading volume (without part) — 60 %; rotor speed — 50 rpm; processing time — 30, 60, 90 min; rotor axis tilt angles — 0^o and 5^o. The influence of treatment modes and conditions on the process intensity was considered on plate samples with dimensions of 80×10×1 mm made of aluminum alloy D16T. To determine metal removal, the samples were weighed on Ohaus AX223 analytical balance before and after processing.

Results. The patterns of metal removal from samples at different processing times, the location of samples in the working area of a screw rotor with different angles of inclination, and its speed are presented.

Discussion and Conclusions. The regularities established in the course of research indicate the efficiency of rotary-screw process systems for solving problems on the finishing treatment of long-length parts. The main factors that control such processing in devices with a screw rotor and affect its intensity (and, as a consequence, the process performance) are the screw rotor speed, the shape of the perimeter, and the axis angle.

Keywords: finishing and cleaning, screw rotor, long parts, processing medium, process intensity, metal removal.

***For citation*:** V. A. Lebedev, L. M. R. Al-Obaidi, Nikolay S. Koval. The finishing and cleaning of long parts in screw rotors. Advanced Engineering Research, 2022, vol. 22, no. 1, pp. 42–49. (In Russ). https://doi.org/10.23947/2687-1653-2022-22-1-42-49

Introduction. Finding efficient ways of finishing and cleaning long parts [1-6] predetermined the creation of a rotary-screw through-flow process system to solve this problem (Fig. 1) [7–15] [1, 2].

[1] Babichev AP, Babichev IA, Serga GV. Device for vibration processing of long parts. RF Patent no. 2228252, 2004. (In Russ.)
[2] Lebedev VA, Al-Obaidi LMR, Koval NS, et al. Unit for finishing and cleaning of long parts. RF Patent no. 2750922, 2021. (In Russ.)

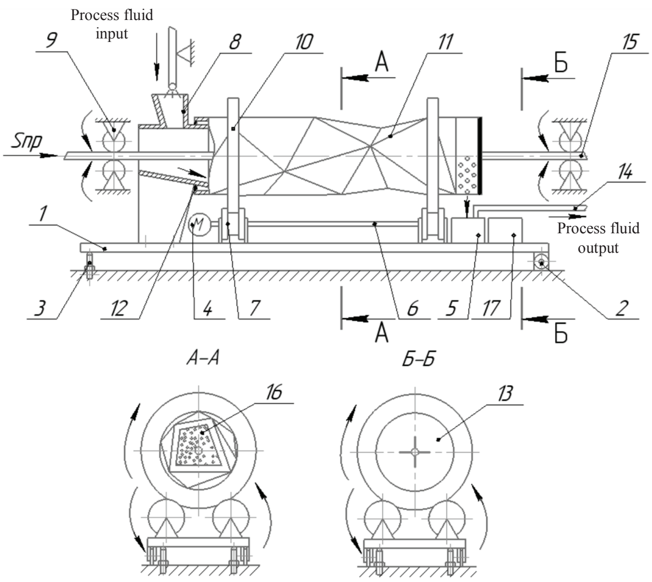

Fig. 1. Process flowchart of finishing and cleaning long parts in a screw rotor:
1 — mounting frame, 2 —lugs, 3 — adjusting screws, 4 — engine, 5 — sump tank, 6 — drive shafts, 7 — roller bearings, 8 — shells, 9 — rollers, 10 — rims, 11 — screw rotor, 12 — gasket, 13 — slotted gasket, 14 — piping system, 15 — part, 16 — processing medium, 17 — container

The main working element of this type of process system is a screw rotor. Its perimeter is made in the form of a combination of flat elements of various shapes and sizes, multidirectional with respect to the helical lines on their outer surface. The processing granular medium is located inside the rotating screw rotor. Being carried away by flat elements, at a certain moment, under the influence of gravity, it avalanches downwards. At the same time, the upper layers of the loading masses rotate around their own axes, drawing in nearby layers of particles of the loading masses. As a result, the particles of the loading masses roll relative to each other. In addition, when an avalanche rolls down the uneven surface of the underlying layers, small force strikes and sliding of the particles of the loading masses occur. Thus, the part is processed by abrasion, scratching, and, to a small extent, by blows. The technological effect of processing depends on the dimensions of the screw rotor, the particle masses of the processing medium, the filling factor of the working chamber, the speed of rotation, the geometry of the screw rotor, and a number of other factors.
The objective of the presented study is to justify the intensity of the machining process in devices equipped with a screw rotor.

Materials and Methods. Metal removal is accepted as the main parameter determining the intensity of the machining process in screw rotors.

For processing, an experimental rotary-screw installation, made on the basis of a 1K625 model screw-cutting machine, was used (Fig. 2).

Fig. 2. General view of the experimental rotary-screw installation

The processing medium consisted of molded abrasive pellets of the PT 10x10 brand. The research conditions were as follows:

— loading volume (without parts) — 60 %,

— rotor speed — 50 rpm,

— processing time — 30, 60, 90 min,

— rotor axis tilt angles — 0^o and 5^o.

The effect of processing modes and conditions on the process intensity was considered on plate samples with dimensions of 80×10×1 mm made of aluminum alloy D16T. Blanks in the form of long-length rolled products are made of this material, requiring finishing and cleaning before going into production.

In the working area of the experimental screw rotor, three sections A, B, C (Fig. 3), remote from the left end of the screw rotor at distances l_0, l_1, l_2, were determined along the length of the working area.

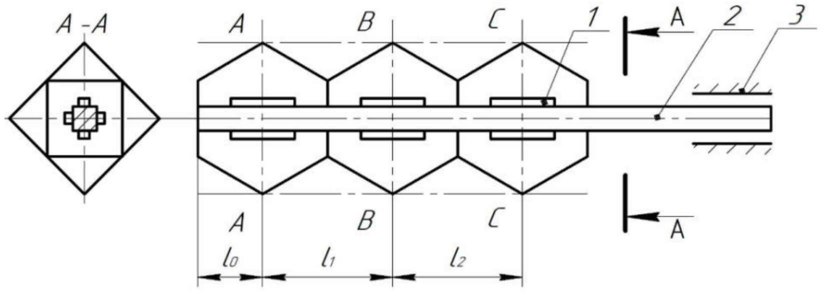

Fig. 3. Diagram of the installation of samples on the mandrel in the rotor:
1 — samples; 2 — mandrel; 3 — lathe toolholders

The samples were fixed on a long four-sided hollow rod and installed according to the scheme shown in Figure 3. Distances l_0, l_1, l_2 correspond to the position of the sections of the rotor working area. To assess the nature of the impact of the processing medium on the various surfaces of the mandrel, 4 samples were processed in each position (section). They were fixed on the edges of the mandrel in such a way that samples 1 and 2 were in the zone of active exposure to the processing medium (with a sliding layer), and samples 3 and 4 were in the passive zone (Fig. 4).

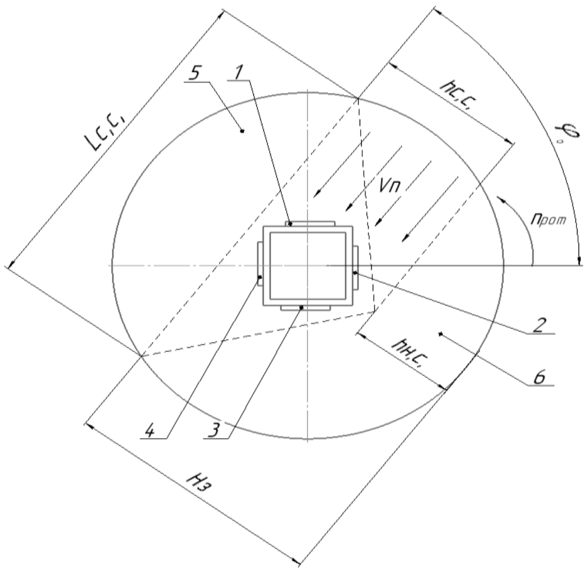

Fig. 4. Layout of samples on the mandrel in cross section:
1, 2, 3, 4 — samples; 5 — screw rotor; 6 — processing medium

The mandrel with samples was installed in the lathe toolholders and inserted into the working area of the screw rotor for processing.

To determine the mass removal of metal, samples were weighed on Ohaus AX223 analytical balance before and after processing. This model is designed for static measurements of the mass of substances and materials accurate to 0.001 g. Metal removal was controlled after thorough washing and drying of the samples.

The rate of metal removal from a unit surface area equal to the area of the square packing granules of the processing medium was determined from the ratio:

$$\gamma_{уд} = \frac{\Delta Q\ S_{уп}}{S \cdot t},\ \text{g/s},$$

where ΔQ — metal removal from the surface, g; t — processing time, s; S — area of the processed surface of the samples, mm^2; $S_{уп}$ — square packing granules of the processing medium, mm^2.

The processing duration was recorded using a time relay (timer) of VL-45UHL41 model.

The experimental results were determined as the arithmetic mean difference of the corresponding measurement values of the samples or batch of samples before and after processing.

Research Results. Figures 5–7 show the results of experimental studies on the intensity of the processing in a screw rotor.

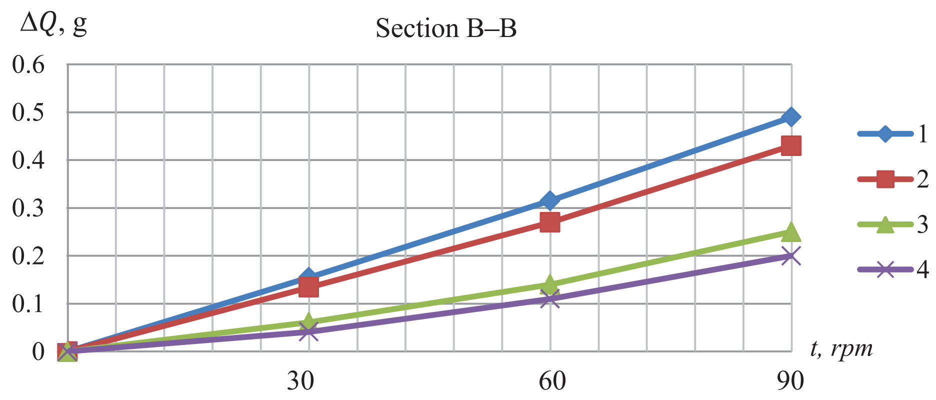

a)

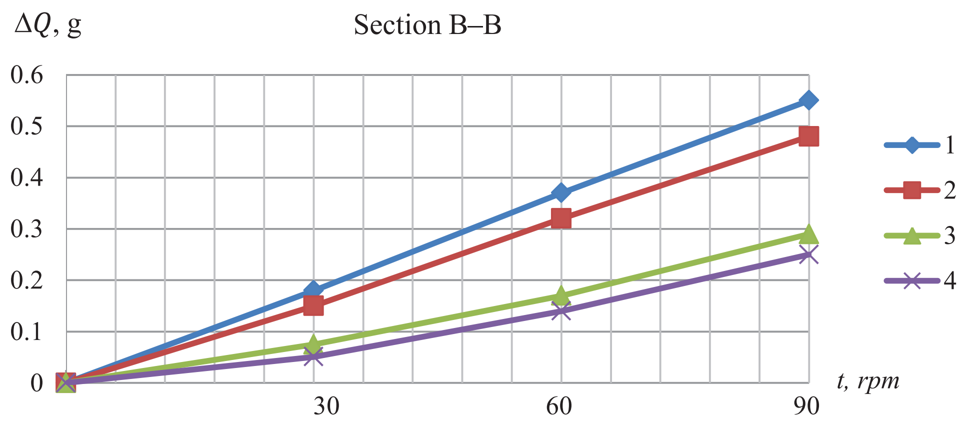

b)

Fig. 5. Change in material removal from D16T samples depending on the processing time and the location of the samples on the mandrel:
a) with an angle of inclination of 0°; *b*) with an angle of inclination of 5°

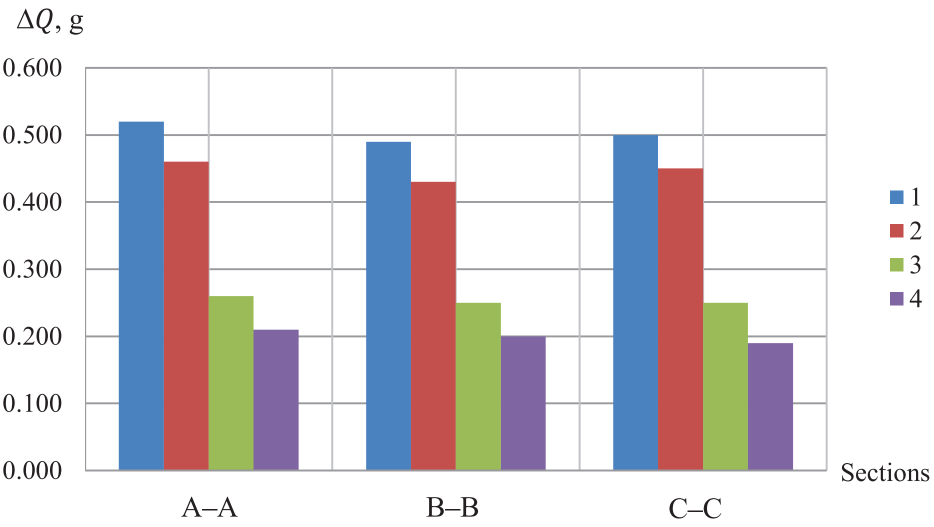

a)

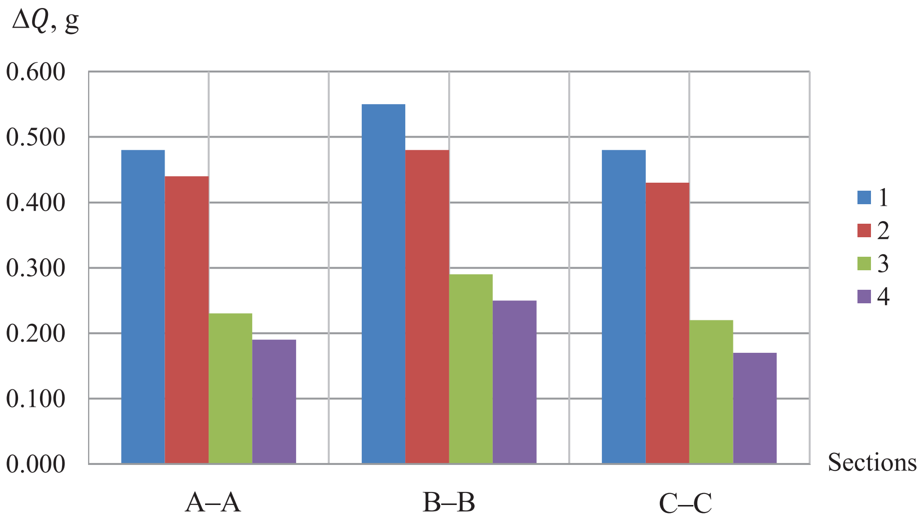

b)

Fig. 6. Change in material removal from D16T samples depending on their location in the working area of the screw rotor (in 90 min):
a) with an angle of inclination of 0°; *b*) with an angle of inclination of 5°

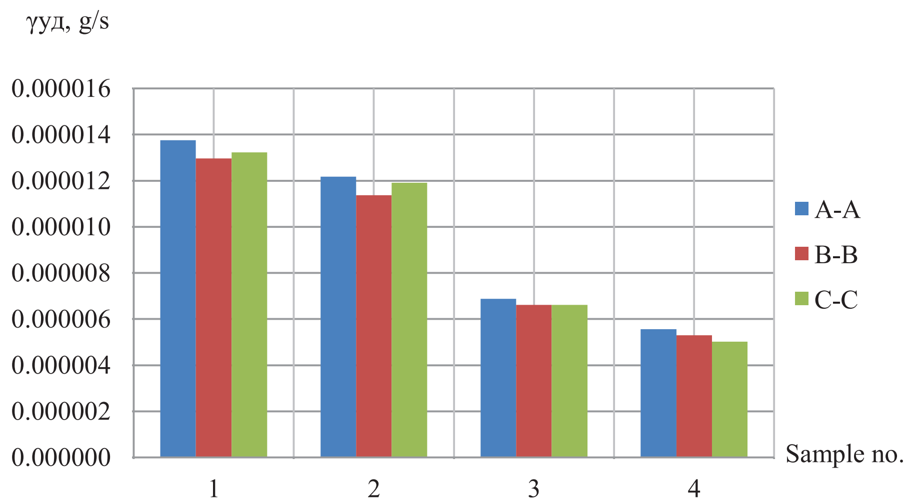

a)

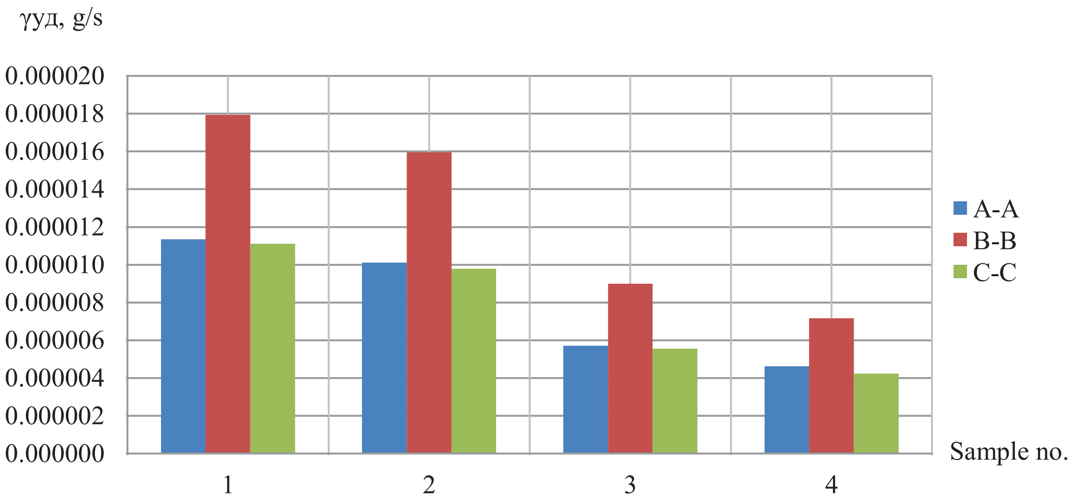

b)

Fig. 7. Change in specific metal removal from D16T samples depending on their location on the mandrel (in 90 min):
a) with an angle of inclination of 0°; *b)* with an angle of inclination of 5°

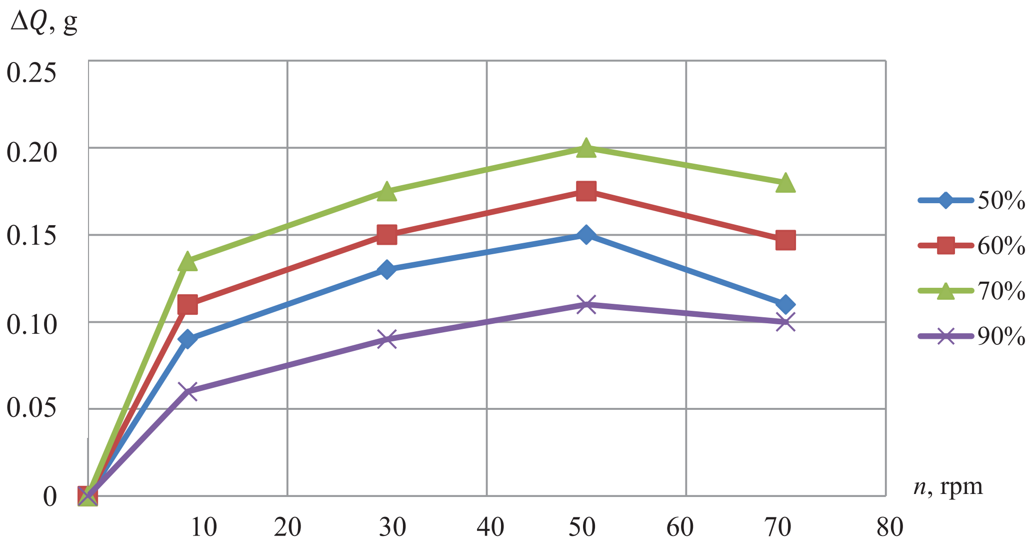

Рис. 8. Change in metal removal from D16T samples depending on the loading of the screw rotor working area by processing medium and the rotation speed (in 30 min)

Discussion and Conclusions. The research results allow us to make a number of statements.

1. The form of the curve describing the change in the amount of metal removal from the surface on the processing time is close to linear (Fig. 5). This does not depend on the location of the samples in the working area of the screw rotor, its design, and the angle of inclination relative to the axis of rotation.

2. The kinetics of particle motion and, as a consequence, the intensity of metal removal in various sections of the working area of the screw rotor are determined by the angle of inclination of the plates that create the shape of the working sections of the rotor. With their identical shape (Fig. 3), almost the same processing intensity is provided. The difference in the amount of removal in three sections was 3 %.

3. Processing intensity (Fig. 5–7) depends on the position of the surface of the samples in relation to the direction of motion of the granules of the sliding layer (Fig. 4). Two cases of metal removal were compared; first— from samples 1 and 2 installed in the active zone of the processing medium; second — from samples 3 and 4 installed in a passive zone characterized by weak energy-force interaction with the treated surface. In the first case, the metal consumption is twice as high.

4. Changing the angle of inclination of the screw rotor axis relative to the axis of its rotation increases the intensity of sample processing in the middle section (B–B) by 1.2 times and reduces it in the working areas of the end sections (Fig. 5–7). This is due to a change in the kinematics of the medium motion in the working area of the screw

rotor. With every full turn, the processing medium tends to move to the middle part of the rotor working area (section B–B). This provides:

— constancy of the media volume pressure on the samples;

— activation of shock-pulse action of the processing medium granules on the surface of samples.

In addition, when the angle of inclination of the screw rotor axis changes, the axial pressure of the processing medium on the end walls decreases. This is very important for pass-through type installations, because this prevents the granules from spilling out of the holes designed for the passage of long parts through the working area.

5. The rotation speed of the screw rotor is an important technology factor that determines the processing intensity in a rotary-screw installation. It can be seen from Figure 8 that with different loading degrees, the amount of material removal from all samples increases with an increase in the rotation speed of the screw rotor up to 50 rpm. When the speed increases to 70 rpm, the indicator decreases. This is due to the increased centrifugal forces. Their action causes a certain volume of particles of the processing medium to remain permanently at the rotor walls. As a result, the number of sliding layers of the medium is reduced, and, consequently, the intensity of the impact on the surface of the samples is reduced.

The regularities and technological capabilities of the processing in a screw rotor established in the course of research indicate the acceptability and efficiency of the rotary-screw process systems for solving problems related to the finishing processing of long-length parts.

In the conducted study, the key factors considered were the rotation speed of the screw rotor, the angle of inclination of its axis, and the shape of the perimeter. They provide finishing control in devices with a screw rotor, affect its intensity, and hence, the process performance.

References

1. Babichev AP, Motrenko PD, Gillespi LK, et al. Primenenie vibratsionnykh tekhnologii na operatsiyakh otdelochno-zachistnoi obrabotki detalei. Rostov-on-Don: DSTU Publ. Centre; 2010. 285 p. (In Russ.)

2. Babichev AP, Babichev IA. Osnovy vibratsionnoi tekhnologii. 2nd revised and enlarged ed. Rostov-on-Don: DSTU Publ. Centre; 2008. 693 p. (In Russ.)

3. Butenko VI. Finishnaya obrabotka poverkhnostei detalei: sposoby, ustroistva, instrumenty. Rostov-on-Don: DSTU Publ. Centre; 2016. 219 p. (In Russ.)

4. Tamarkin MA, Tishchenko EE, Shvedova AS. Optimization of Dynamic Surface Plastic Deformation in Machining. Russian Engineering Research. 2018;38:726–727. http://dx.doi.org/10.3103/S1068798X18090277

5. Tamarkin MA, Tishchenko EE. Osnovy optimizatsii protsessov obrabotki detalei svobodnym abrazivom. Saarboniken: Lambert Academic Publishing; 2015. 140 p. (In Russ.)

6. Li Xin, Peng Gaoliang, Li Zhe. Prediction of seal wear with thermal structural coupled finite element method. Finite Elements in Analysis and Design. 2014;83:10–21. http://dx.doi.org/10.1016/j.finel.2014.01.001

7. Taratuta VD, Belokur KA, Serga GV. Rotary screw technology systems for combine harvesters. Proceedings of the Kuban State Agrarian University. 2015;57:197–206.

8. Pesin MV. Improving the Reliability of Threaded Pipe Joints. Russian Engineering Research. 2012;32:210–212. http://dx.doi.org/10.3103/S1068798X12020232

9. Macdonald KA, Bjune JV. Failure analysis of drillstrings. Engineering Failure Analysis. 2007;14:1641–1666. http://dx.doi.org/10.1016/j.engfailanal.2006.11.073

10. Xiao-Hua Zhu, Yu Wang, Hua Tong. The parameter sensibility analysis for fishing box tap based on the overall process of elastoplasticity in oil and gas wells. Mathematical and Computer Modeling. 2013;58:1540–1547. http://dx.doi.org/10.1016/j.mcm.2013.06.004

11. Fares Y, Chaussumier M, Daidié A, et al. Determining the life cycle of bolts using a local approach and the Dang Van criterion. Fatigue & Fracture of Engineering Materials & Structures. 2006;29:588–596. http://dx.doi.org/10.1111/j.1460–2695.2006.01029.x

12. Serga GV, Seryy DG, Marchenko AYu. Investigation of physical phenomena occurred in contact area of bulk particles at their motion in screw drums by methods of similarity theory, engineering and computer graphics. Vestnik Bryanskogo gosudarstvennogo tekhnicheskogo universiteta. 2019;79:20–28. http://dx.doi.org/10.30987/article_5d10851f18f085.56011612

13. Serga GV, Lebedev VA, Belokur KA, et al. Increased productivity of technological systems for finishing and strengthening parts based on using screw rotors. Strengthening Technologies and Coatings. 2016;136:16–19.

14. Lebedev VA, Serga GV, Chaava MM, et al. The study of fine-cleaning treatment for removal of burrs in screw rotor. IOP Conference Series: Materials Science and Engineering this link is disabled. 2021;1029:012001. http://dx.doi.org/10.1088/1757-899X/1029/1/012001

15. Lebedev VA, Serga GV, Chaava MM. Method of Calculating the Machines Drive with Screw Working Bodies Mounted from Tetrahedral Hollows. ICIE 2021: Proceedings of the 6th International Conference on Industrial Engineering (ICIE 2020). 2021. P. 557–563. http://dx.doi.org/10.1007/978–3–030–54814–8_64

Received 29.12.2021
Revised 24.01.2022
Accepted 27.01.2022

About the Authors:

Lebedev, Valery A., professor of the Mechanical Engineering Department, Don State Technical University (1, Gagarin sq., Rostov-on-Don, 344003, RF), Cand.Sci. (Eng.), professor, ResearcherID, ScopusID, ORCID, va.lebidev@yandex.ru

Al-Obaidi Luay Mohammed Rajab, postgraduate student of the Mechanical Engineering Department, Don State Technical University (1, Gagarin sq., Rostov-on-Don, 344003, RF), lecturer, Middle Technical University, Institute of Technology-Baghdad (Muasker Al Rashid Street, Baghdad, Iraq) Scopus, ORCID, luayrajab@yahoo.com, luay_mohammed@mtu.edu.iq

Koval, Nikolay S., associate professor of the Tool Engineering and Biomedical Engineering Department, Don State Technical University (1, Gagarin sq., Rostov-on-Don, 344003, RF), Cand.Sci. (Eng.), associate professor, Researcher ID, ScopusID, ORCID, koval-nc@mail.ru

Claimed contributorship

V. A. Lebedev: academic advising; basic concept formulation. N. S. Koval: research objectives and tasks setting; computational analysis; text preparation; formulation of conclusions. L.M.R. Al-Obaidi: analysis of the research results; the text revision; correction of the conclusions.

All authors have read and approved the final manuscript.

MACHINE BUILDING AND MACHINE SCIENCE

Check for updates

UDC 621.9 + 621.2.082.18
https://doi.org/10.23947/2687-1653-2022-22-1-50-56

Original article

Tribotechnical properties of experimental hard alloys with modified cobalt binder

Evgeniy V. Fominov ✉, **Constantine G. Shuchev**, **Muharbiy M. Aliev**
Don State Technical University (Rostov-on-Don, Russian Federation)
✉ fominoff83@mail.ru

Introduction. This paper discusses tribomechanical characteristics of experimental hard alloys with a modified cobalt binder under friction without lubrication on hard-to-cut materials – stainless steel and titanium alloy. The research objective is to evaluate the process of friction interaction for each friction pair according to a number of parameters, and to determine the optimal combinations of "experimental hard alloy – structural material" on the basis of the established tribological indicators.

Materials and Methods. Tribological tests of hard alloys were carried out using a cylinder-to-disc friction scheme for different sliding speeds and temperatures under constant load without the use of lubricants. Comparison of the friction interaction process was carried out by the frictional force, volumetric wear and roughness of the friction tracks on the counterbody. Stainless steel 12H18N9T and titanium alloy BT3-1 were used as counterbody materials. The resistance of experimental compositions to the abrasive type of wear was determined through measuring the surface dynamic microhardness on a scanning nanohardness tester by analyzing the thickness of the scratches caused by the indenter.

Results. According to the results of surface microindentation, the experimental alloys 2.22 (binder 5.65% Co + 1.8% Mo + 0.6% Ti) and 2.23 (binder 5.1% Co + 2.7% Mo + 0.61 % Ti) are characterized by the highest microhardness. For these materials, the average scratch width at various forces was minimal. During tribological tests, the best frictional characteristics were recorded for stainless steel in combination with experimental alloy 2.22, and for the friction pair "titanium alloy VT3-1 — hard alloy 2.23". The friction of this combination of materials was characterized by low friction coefficients with a low level of fluctuations, minimal wear of samples, and changes in the initial microrelief of their surfaces.

Discussion and Conclusions. As a result of the research, the optimal friction pairs from the point of view of tribological interaction were established, specifically "titanium alloy VT3-1 — hard alloy 2.23" and "stainless steel 12X18N9T — hard alloy 2.22". The frictional interaction for these combinations of materials is characterized by minimal volumetric wear, which will contribute to increasing the wear resistance of the tool in the areas of elastic contact on the front and rear surfaces.

Keywords: hard alloys, wear resistance, stainless steel, titanium alloy.

For citation: E. V. Fominov, C. G. Shuchev, M. M. Aliev. Tribological properties of experimental hard alloys with modified cobalt binder. Advanced Engineering Research, 2022, vol. 22, no. 1, pp. 50–56. (In Russ). https://doi.org/10.23947/2687-1653-2022-22-1-50-56

Introduction. Various materials based on tungsten carbide, including hard alloys (HA), are widely used in many branches of modern production due to a number of advantages of their physical and mechanical properties [1–3]. The largest share (about 65%) of tool cutting materials (TCM) used in metalworking also belongs to HA that provide high cutting speeds when processing various structural materials [1, 3]. Currently, many directions related to improving the HA performance characteristics by various methods are being developed [4–6].

One of them is the creation of new binder compositions for carbide phases [7–9]. Experimental hard alloys (EHA) based on single-carbide alloy VK8 with various types of modified binders[1] have been developed at the Metal-Cutting Machines and Tools Department, Don State Technical University. Despite the fact that cobalt, because of its properties, is the most common binder for WC, the use of this metal is economically unprofitable due to its scarcity and high price. Experimental alloys are characterized by high values of the thermal entropy of the modified cobalt binder (Table 1) and, consequently, lower thermo-emf with respect to tungsten carbide, which increases the electrochemical stability of these materials [9–11]. Among the materials processed with a carbide tool, titanium-aluminum alloys and austenitic stainless steels can be distinguished. Due to a number of characteristics, these materials are used for the manufacture of parts in the most critical areas of mechanical engineering, including aerospace, nuclear, food, and medical production. Due to a number of characteristics, these materials are used for manufacturing parts in the most critical areas of mechanical engineering, including aerospace, nuclear, food and medical production. Cutting of titanium alloys and stainless steels is difficult due to their low thermal conductivity, high cutting forces, as well as unsatisfactory tribotechnical characteristics [12]. In this regard, the investigation of the features of the frictional interaction of newly developed TCM with the mentioned materials is an urgent task. Taking into account modern environmental and economic requirements for the organization of production, the processing of these structural materials takes place mainly in the mode of minimum output (MQL - minimum quantity lubrication) or without the use of lubricant-cooling process media (LCPM) [13, 14].

Then, the contact areas of the TCM and the workpiece material to be processed on the front and rear surfaces of the cutting tool can be considered as tribosystems operating in the friction mode without LCPM or in the mode of boundary friction. This does not exclude a significant proportion of metal contact. In this case, the operational parameters of the TCM, as an element of the friction couple, will be significantly effected by its tribotechnical characteristics in the dry friction mode.

The presented paper is devoted to investigating tribotechnical characteristics of experimental hard alloys under dry friction on hard-to-cut materials, as well as to determining the optimal combination of "EHA — structural material" from the point of view of frictional interaction. This work is part of a complex of studies on physico-mechanical, tribological and cutting properties of experimental HA with modified cobalt binder.

Materials and Methods. The following HA compositions were selected as objects of study of surface mechanical characteristics (Table 1). Tribological tests were carried out on square-section indenters (a=5 mm, Ra=0.1-0.12 μm) of the three most promising compositions (2.21, 2.22, and 2.23) on tribometer T-11 (Poland) implementing a "finger-disk" friction scheme. During the experiments, a change in the friction force (*F,* N) was recorded depending on the friction path (*L*, m). Each experiment was repeated 3–5 times, the experimental results were processed using methods of dispersion analysis [0]. Titanium alloy VT3-1 and stainless steel 12X18H9T were selected as the material of the rotating disk (counterbody); the surface roughness of these samples was within R_a 0.12–0.15 μm.

[1] Ryzhkin AA, Meskhi BCh, Bokov AI, et al. Hard alloy based on tungsten carbide (options). RF patent no. 2531332, 2014. (In Russ.)

Table 1

EHA chemical composition and thermodynamic properties

Carbide grade	Composition	Entropy, J/mol·deg	
		$(S^0_{298})_{WC}$	$(S^0_{298})_{связ.}$
1	2	3	4
2.19	92.63% WC+7.37%[1.52%Co+ +5.03%Fe+0.82%Cu]	35.6	28.60
2.20	92.38% WC+7.62% [3.6%Co+ +3.2%Fe+0.82%Cu]		29.31
2.21	92.45% WC+7.55% [5.3%Co+l.43%Fe+0.82%Cu]		29.83
2.22	91.95% WC+8.05% [5.65%Co+l.8%Mo+0.6%Ti]		29.72
2.23	91.59% WC+8.41% [5.1%Co+2.7%Mo+0.61%Ti]		29.59
2.24	90.62% WC+9.38% [3.34%Co+5.44%Mo+0.6%Ti]		29.22
VK8 (Basic)	92% WC + [7.5–8]%Co, Fe≤0.3%		28.50

The studies were carried out at different sliding speeds and temperatures at constant load P=20 N. The mass of the samples was determined on LV 210-A balance. The roughness of the friction tracks on the counterbody after the experiments was measured on the Abris-PM7 profilometer (Russia). The dynamic microhardness of the EHA surfaces was determined using a scanning nanohardness tester NanoSCAN-01 (Russia) through analyzing the thickness of scratches applied with different forces. The studies on worn surfaces of EHA samples were carried out on inverted ZEISS AxioVert. A1 microscope.

Research Results. The smallest width h of scratches applied by various forces F_s belongs to alloys 2.22 and 2.23, the binder in which was modified by Mo-Ti group (Table 2).

Table 2

Scratch width h under various forces F_s according to the results of EHA sclerometry

F_s, N	h, µm						
	Carbide grades						
	2.19	2.20	2.21	2.22	2.23	2.24	VK8
5	0.3	0.2	0.5	-	-	1.5	1.1
15	1.3	1.3	1.5	0.7	1.2	2.5	1.8
25	2.4	1.8	2.4	1.2	1.8	3.3	2.9

Thus, these materials are characterized by the highest surface hardness at the micro-level, which implies better resistance to abrasive wear. It must be said that no noticeable changes in the surface microrelief were detected in these alloys under forces F_s<15 N. The lowest microhardness according to the test results was demonstrated by composition 2.24.

To determine and compare the HA wear resistance, the mass loss of the indenter was measured for each value of friction path L, and then the volumetric wear of samples ΔV was determined (Fig.1, 2).

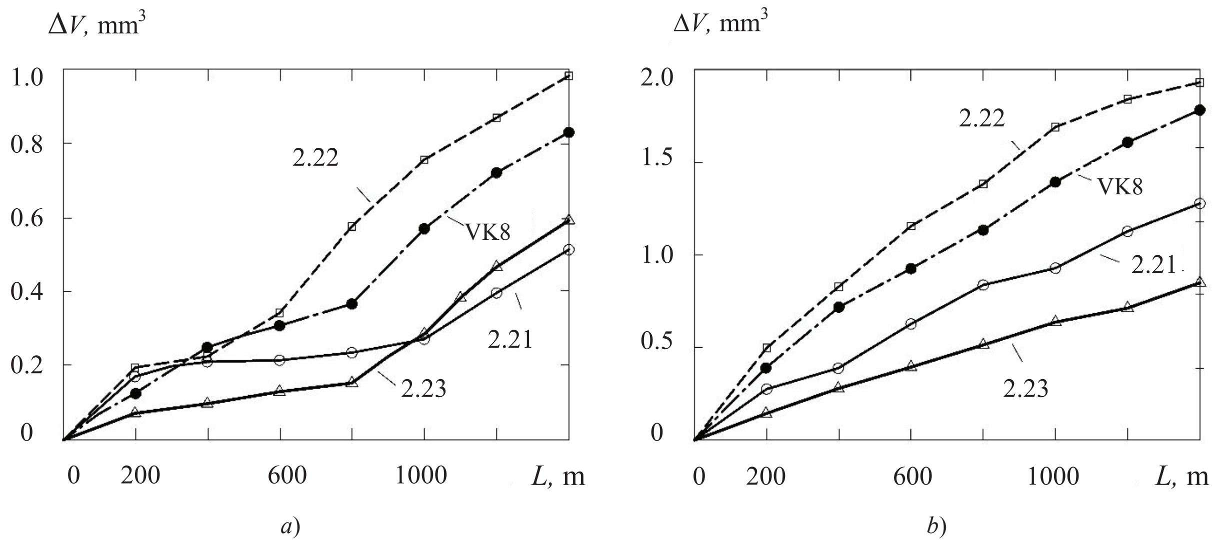

Fig. 1. Volumetric wear of EHA indenters under friction on titanium alloy VT3-1 at temperatures: *a*) 25° C; *b*) 300° C

Under friction on a titanium alloy at different temperatures, the greatest volumetric wear *ΔV* was observed in alloy 2.22. The best wear resistance was demonstrated by composition 2.23 (Fig. 1). Under friction on stainless steel, the lowest values of parameter *ΔV* were recorded for composition 2.22 (Fig. 2). In this case, the greatest volume wear also belongs to the HA experimental compositions. At room temperature, alloy 2.21 demonstrates the highest wear intensity, and, when the friction zone is heated, the maximum wear values are fixed for composition 2.23.

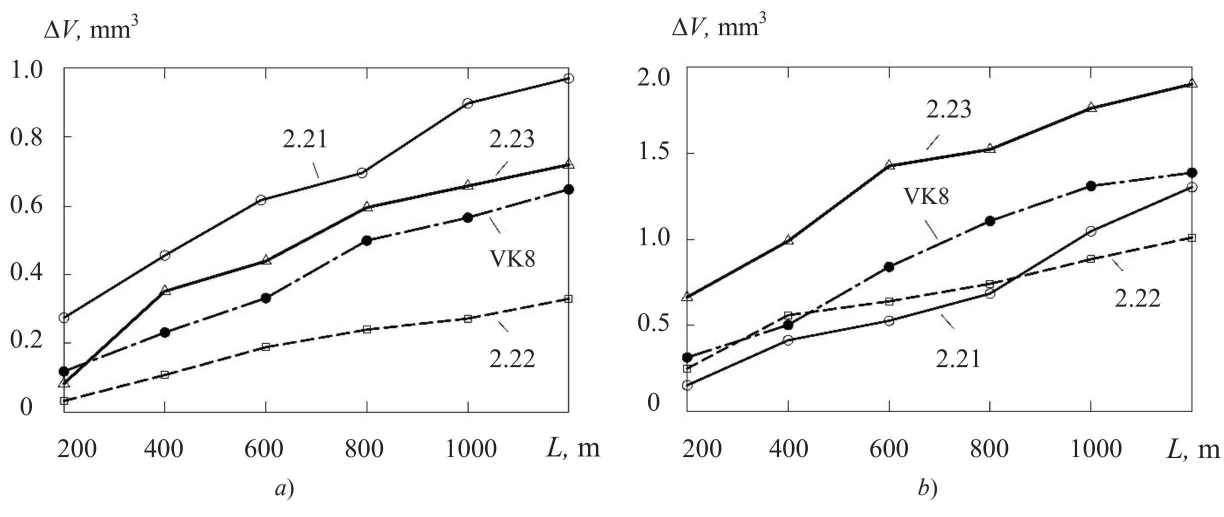

Fig. 2. Volumetric wear of EHA indenters under friction on stainless steel 12X18N9T at temperatures: *a*) 25^{o} C; *b*) 300^{o} C

The surfaces of indenters made of alloys that have demonstrated maximum volume wear are characterized either by the predominance of worn areas, or the original surface of the material is preserved only in the form of individual rare fragments. Figure 3 shows pictures of the surfaces of indenters made of alloys 2.23 and VK8 after friction on 12X18N9T steel at a temperature of 300° C for friction path *L*=600 m.

The surface of the more wear-resistant alloy 2.22 has a spotted structure with a predominance of initial unworn areas (Fig. 3 *a*). The surface of the base alloy VK8 is characterized by a large scale of destruction, rare fragments of the initial surface are discretely located, their total area is much smaller (Fig. 3 *b*).

The frictional interaction of friction couples was estimated through comparing the average values of friction coefficient f_{cp} and its fluctuations without taking into account the run-in stage I (Fig. 4 *a, b*). The comparison of the friction coefficient fluctuations was carried out by standard deviation σ_{cp} of this parameter from f_{cp} at the steady-state friction stage II.

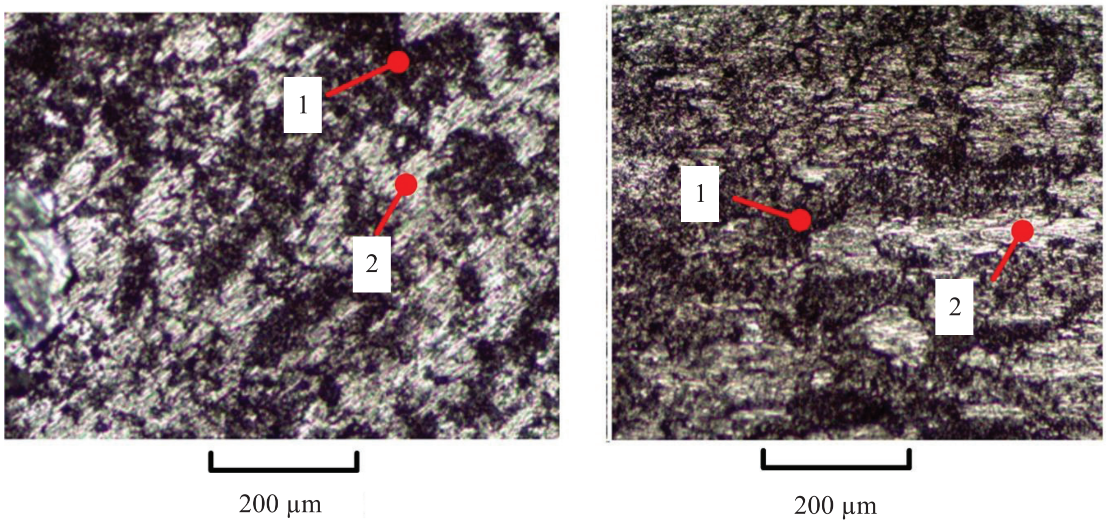

a) *b*)

Fig. 3. Comparison of surfaces of indenters of alloys 2.22 (*a*) and VK8 (*b*) after friction on 12X18N9T stainless steel (T=300° C, v=0.3 m/s): 1 — worn surface areas; 2 — fragments of the initial surface

The surface of the more wear-resistant alloy 2.22 has a spotted structure with a predominance of initial unworn areas (Fig. 3 *a*). The surface of the base alloy VK8 is characterized by a large scale of destruction, rare fragments of the initial surface are discretely located, their total area is much smaller (Fig. 3 *b*).

The frictional interaction of friction couples was estimated through comparing the average values of friction coefficient f_{cp} and its fluctuations without taking into account the run-in stage I (Fig. 4 *a, b*). The comparison of the friction coefficient fluctuations was carried out by standard deviation σ_{cp} of this parameter from f_{cp} at the steady-state friction stage II.

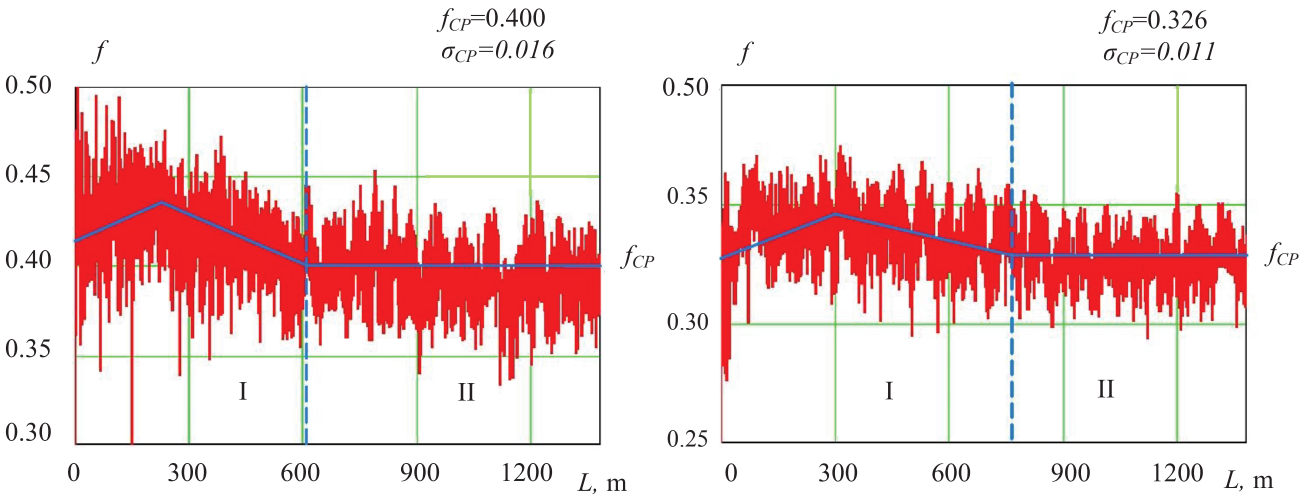

a) *b*)

Fig. 4. Dependence of friction coefficients f on path L under friction on VT3-1 alloy (T=25° C, v=0.3 m/s): *a*) 2.23; *b*) VK8: I — run-in stage; II — stable friction stage

In the case of friction on a titanium alloy at different temperatures, the average friction coefficients and their standard deviations for all EHA were higher than for the base grade VK8. However, the lowest values of these parameters among the experimental compositions belong to alloy 2.23 (Fig. 4 *a*).

Under friction on steel 12Kh18N9T, both at room temperature and with heating, the largest values of parameters f_{cp} and σ_{cp} belong to VK8 base alloy (at 25° C: f_{cp}=0.72 and σ_{cp}=0.048; at 300° C: f_{cp}=0.68 and σ_{cp}=0.032). In this series of experiments, the minimum coefficients of friction and its fluctuations were fixed for composition 2.22.

Under friction without heating for this material, the values of the estimated parameters were f_{cp}=0.44 and σ_{cp}=0.025, and at 300° C, they increased to f_{cp}=0.57 and σ_{cp}= 0.029.

The average roughness of the friction tracks on the counterbodies was measured and compared for the maximum value of the friction path. Under friction on steel 12Kh18N9T, the smallest values of this parameter belong to alloy 2.22. At a temperature of 25° C, the roughness was $Ra_{2.22}$=4.12 µm, at 300° C — $Ra_{2.22}$=5.12 µm. The highest roughness values were recorded during friction of VK8 base alloy. At room temperature, the value of this parameter was Ra_{BK8}=5.07 µm, with heating of the friction zone — Ra_{BK8}=5.95 µm. High roughness values indicate that the frictional interaction of this material and stainless steel was accompanied by larger-scale destruction under the formation, and destruction of adhesive and cohesive seams on the surface of the counterbody material.

In a series of experiments with titanium alloy VT3-1, the best indicators of counterbody roughness were recorded after friction of the experimental composition 2.23 ($Ra_{2.23}$=3.35 µm at 25° C and $Ra_{2.23}$=4.54 µm at 300° C). The greatest surface damage was obtained for the samples after frictional interaction with alloy 2.22. The surface roughness during friction without heating was $Ra_{2.22}$=6.88 µm, with heating — $Ra_{2.22}$=8.07 µm.

Discussion and Conclusions. As a result of the study of the tribological characteristics of experimental hard alloys under friction on hard-to-cut materials, the best combinations in terms of the frictional interaction of a pair of materials have been established. For stainless steel 12Kh18N9T, the best tribological parameters were recorded under friction in combination with alloy 2.22, for titanium alloy — with composition 2.23. The friction process for these combinations of materials at different temperatures is characterized by minimal volumetric wear, low coefficients of friction, and a smaller scale of destruction of the surfaces of both hard-alloy indenters and counterbodies made of structural materials.

References

1. García J, Ciprés VC, Blomqvist A, et al. Cemented carbide microstructures: A review. Journal of Refractory Metals and Hard Materials. 201;80:40–68. https://doi.org/10.1016/j.ijrmhm.2018.12.004

2. Heydari L, Lietor PF, Corpas-Iglesias FA, et al. Ti(C,N) and WC-Based Cermets: A Review of Synthesis, Properties and Applications in Additive Manufacturing. Materials. 2021;14:6786. https://doi.org/10.3390/ma14226786

3. Sandoval DA, Roa JJ, Ther O, et al. Micromechanical properties of WC-(W, Ti, Ta, Nb) C-Co composites. Journal of Alloys and Compounds. 2019;777:593–601. https://doi.org/10.1016/j.jallcom.2018.11.001Pötschke J, Kroedel A, Vornberger A, et al. Influence of Cemented Carbide Composition on Cutting Temperatures and Corresponding Hot Hardnesses. Materials. 2020;13:4571. https://doi.org/10.3390/ma13204571

4. Ćorić D, Šnajdar Musa M, Sakoman M, et al. Analysis of Different Complex Multilayer PACVD Coatings on Nanostructured WC-Co Cemented Carbide. Coatings. 2021;11:823. https://doi.org/10.3390/coatings11070823

5. Siwak P. Indentation Induced Mechanical Behavior of Spark Plasma Sintered WC-Co Cemented Carbides Alloyed with Cr_3C_2, TaC-NbC, TiC, and VC. Materials. 2021;14:217. https://doi.org/10.3390/ma14010217

6. Yanju Qian, Zhiwei Zhao. Microstructure and Properties of Ultrafine Cemented Carbides Prepared by Microwave Sintering of Nanocomposites. Crystals. 2020;10:507. https://doi.org/10.3390/cryst10060507

7. Zhao Zhenye, Lin Jianwei, Tang Huaguo, et al. Investigation on the mechanical properties of WC–Fe–Cu hard alloys. Journal of Alloys and Compounds. 2015;632:729–734. https://doi.org/10.1016/j.jallcom.2015.01.300

8. Jianzhan Long, Kai Li, Fei Chen, et al. Microstructure evolution of WC grains in WC–Co–Ni–Al alloys: Effect of binder phase composition. Journal of Alloys and Compounds. 2017:710:338–348. http://dx.doi.org/10.1016/j.jallcom.2017.03.284

9. Ryzhkin AA, Burlakova VE, Moiseev DV, et al. Determination of the efficiency of high-entropy cutting tool materials. Journal of Friction and Wear. 2016;37:47–54. https://doi.org/10.3103/S1068366616010153

10. Ryzhkin AA, Burlakova VE, Novikova AA. Wear and performance of hard alloys. Russian Engineering Research. 2018;38:438–441. https://doi.org/10.3103/S1068798X18060151

11. Ryzhkin AA, Ilyasov VV. O svyazi mezhdu iznosostoikost'yu i fizicheskimi svoistvami instrumental'nykh materialov. Russian Engineering Research. 2000;12:32–40. (In Russ.)

12. Grzesik W. Advanced Machining Processes of Metallic Materials: Theory, Modelling, and Applications. 2nd ed. Elsevier; 2017. 578 p.

13. Sheng Qin, Zhongquan Li, Guoqiang Guo, et al. Analysis of Minimum Quantity Lubrication (MQL) for Different Coating Tools during Turning of TC11 Titanium Alloy. Materials. 2016;9:804. https://doi.org/10.3390/ma9100804

14. Tadeusz Leppert, Ru Lin Peng. Residual stresses in surface layer after dry and MQL turning of AISI 316L steel. Production Engineering. 2012;6:367–374. https://doi.org/10.1007/s11740-012-0389-3

15. Montgomery DC. Design and analysis of experiments. 8th ed. New York: John Wiley & Sons;2013. 612 p.

Received 10.01.2022

Revised 28.01.2022

Accepted 09.02.2022

About the Authors:

Fominov, Evgeniy V., senior lecturer of the Engineering and Computer Graphics Department, Don State Technical University (1, Gagarin sq., Rostov-on-Don, 344003, RF), Cand.Sci. (Eng.), Researcher ID, ScopusID, ORCID, fominoff83@mail.ru

Shuchev, Constantine G., professor of the Metal-Cutting Machines and Tools Department, Don State Technical University (1, Gagarin sq., Rostov-on-Don, 344003, RF), Cand.Sci. (Eng.), professor, ScopusID, ORCID, cshuchev53@mail.ru

Aliev, Muharbiy M., associate professor of the Metal-Cutting Machines and Tools Department, Don State Technical University (1, Gagarin sq., Rostov-on-Don, 344003, RF), Cand.Sci. (Eng.), associate professor, ScopusID, ORCID, m_aliev62@mail.ru

Claimed contributorship

Fominov E. V.: research objectives and tasks setting; conducting experiments; analysis of the research results; formulation of conclusions. Shuchev C. G.: academic advising; analysis of the research results; the text revision; correction of the conclusions. Aliev M. M.: sample preparation; post-experimental examination of samples; the text revision.

All authors have read and approved the final manuscript.

INFORMATION TECHNOLOGY, COMPUTER SCIENCE, AND MANAGEMENT

Check for updates

UDC 681.3
https://doi.org/10.23947/2687-1653-2022-22-1-57-66

Original article

Challenge of the performance management of trust control systems with deep learning

Aleksandr A. Zelensky ✉, **Tagir K. Abdullin**, **Marina M. Zhdanova**, **Vyacheslav V. Voronin**, **Andrey A. Gribkov**
Moscow State Technological University "STANKIN" (Moscow, Russian Federation)
✉ Zelenskyaa@gmail.com

Introduction. The significance of machine learning under the conditions of digital transformation of industry, and methods of implementing deep learning to provide the performance of trust management systems are considered. The necessity of using convolutional artificial neural networks for deep machine learning is determined. Various technologies and architectures for the implementation of artificial neural networks are briefly considered; a comparative analysis of their performance is carried out. The work objective is to study the need to develop new approaches to the architecture of computing machines for solving problems of deep machine learning in the trust management system implementation.
Materials and Methods. In the context of digital transformation, the use of artificial intelligence reaches a new level. The technical implementation of artificial neural systems with deep machine learning is based on the use of one of three basic technologies: high performance computing (HPC) with parallel data processing, neuromorphic computing (NC), and quantum computing (QC).
Results. Implementation models for deep machine learning, basic technologies and architecture of computing machines, as well as requirements for trust assurance in control systems using deep machine learning are analyzed. The problem of shortage of computation power for solving such problems is identified. None of the currently existing technologies can solve the full range of learning and impedance problems. The current level of technology does not provide information security and reliability of neural networks. The practical implementation of trust management systems with deep machine learning based on existing technologies for a significant part of the tasks does not provide a sufficient level of performance.
Discussion and Conclusions. The study made it possible to identify the challenge of the computation power shortage for solving problems of deep machine learning. Through the analysis of the requirements for trust management systems, the external challenges of their implementation on the basis of existing technologies, and the need to develop new approaches to the computer architecture are determined.

Keywords: deep machine learning, processor, trust system, information security, computer, artificial intelligence.

For citation: A. A. Zelensky, T. K. Abdullin, M. M. Zhdanova, V. V. Voronin, A. A. Gribkov. Challenge of the performance management of trust control systems with deep learning. Advanced Engineering Research, 2022, vol. 22, no. 1, pp. 57–66. (In Russ). https://doi.org/10.23947/2687-1653-2022-22-1-57-66

Funding information: the research is done on the Russian Science Foundation grant no. 21-79-10392, https://rscf.ru/project/21-79-10392/

Introduction. Over the past 9 years, the fourth industrial revolution has been taking place on an increasingly large scale in the world, including in Russia. One of its key components is digital transformation affecting all aspects of economic life — from a large-scale industrial production to the service sector, science, education, and households. Under these conditions, the use of the machine in tasks with which a person does not cope or copes worse than the machine, significantly expands. If earlier it was about the mechanization of manual labor and production automation, now a human being can be replaced by a machine in solving the problems of data processing, analysis, forecasting and management of various systems: equipment, engineering processes, industrial enterprises, retail chains, etc.

The practical basis for replacing a human being with a machine in certain areas of intellectual activity is the use of artificial intelligence. The creation of a "strong" artificial intelligence is a task of the future, associated with the need to create and develop new technologies, as well as solving significant ethical problems. Currently, machine learning systems of varying complexity are available for application, representing a step towards creating a "strong" artificial intelligence.

The global market for machine learning systems is expanding rapidly. In 2020, its volume amounted to $11.33 bln, in 2021, it grew to $15.50 bln, and by 2028, it will reach $152.24 bln, showing an average annual growth of 38.6 %[1].

The scope of machine learning systems is very large and includes marketing and trade, banking, industrial production, medicine, etc. Machine learning systems are most in demand in the following industries:

- robotics for the intellectualization of industrial and service robots, including collaborative ones;
- automated control systems for processes and enterprises;
- production process control systems;
- supply chain and customer relationship management systems;
- executive production systems;
- production analytics systems for process equipment;
- business intelligence systems, etc.

Complex process systems, e.g., implemented in the designs of machine tools with real-time numerical control, currently cannot be equipped with control systems suitable for machine learning. This requires computing power capable of performing significant computations in tens of microseconds. Such a problem cannot be solved with the help of modern technical means. Therefore, in most cases, the process of machine learning of the control system is carried out on computers separated from it without time limits, and then the learning results are transferred to the control system in the form of recommendations, instructions on operating modes, tool changes, verification intervals, etc.

Machine learning methods conditionally correspond to the types of inferences that underlie them: induction, deduction, and traduction. The case-based supervised learning method, when large amounts of data prelabeled by a human operator are loaded into the machine, corresponds to induction. The unsupervised learning method, when the machine itself must find patterns in the data, identify patterns, arrange and structure the data, corresponds to induction and traduction. The expert method based on the use of specified patterns and patterns for data processing correspond to deduction and traduction. Traduction is implemented mainly through the use of transfer learning, based on the application to a given task of knowledge gained in solving another task.

Machine learning uses various technologies and mathematical models. The model of artificial neural networks (ANN), built by analogy with biological neural networks, i.e., networks of nerve cells of a living organism, has the greatest potential for development. ANN is a system of interconnected and interacting artificial neurons implemented in the form of processors, processor elements in the form of accelerators or coprocessors under the control of a central

[1] Machine Learning Market, 2021-2028. Hardware & Software IT Services Market Research Report. 2021. P. 160. URL: https://www.fortunebusinessinsights.com/infographics/machine-learning-market-102226 (accessed: 06.11.2021)

processor. ANN neurons are located in levels (layers). The first level corresponds to receiving, processing input data, and passing them to the next level. Intermediate levels are hidden, their task is to process incoming data and transfer it to the last (output) level. A neural network may have several hidden levels interspersed with levels where logical, mathematical, and other transformations are performed. From level to level, the data is processed, at each subsequent level, the relationships of the previous one, are identified. Such a multi-level ANN has great potential and can be used to implement deep machine learning [1–3].

Deep machine learning is an ANN design method using multilayer filters to extract and model features from a set of input data[2]. Such learning can be supervised or unsupervised. It is also possible to use deep machine learning for expert systems.

The technical implementation of artificial neural systems with deep machine learning is based on the application of one of three basic technologies: high-performance computing with parallel data processing, neuromorphic and quantum computing[3].

Materials and Methods

High-performance computing. High-performance computing with parallel data processing is implemented through hybrid computing systems, i.e., systems with a heterogeneous hardware computing structure, including a central processing unit (CPU) and an additional computing module in the form of an accelerator or coprocessor. Depending on the processors used for parallel data processing, hybrid computers have one of four architectures:

1. Graphic processing unit (GPU) based architecture. The most common solutions are graphics accelerators that expand the computing capabilities of the central processing unit of a computer system. The latest advances in this field are NVIDIA Tesla V100 graphics accelerators, providing 120 TFLOPS performance for deep machine learning tasks, i.e., 1.2×1014 floating-point operations per second[4].This is 500-1000 times higher than the performance of an ordinary personal computer (PC). It should also be taken into account that the specified performance is provided when solving problems that require significant computing power and significant time costs, but not when working in real time. Currently, GPU-based architecture is the most accessible one. In particular, to implement a system with limited computing power, it is enough to have a video card with a NVidia graphics processor on a PC that implements the CUDA parallel computing hardware and software architecture. Along with CUDA, GPGPU technologies that use the graphics processor of a video card for computer graphics to perform mathematical calculations include AMD FireStream technology (for ATI graphics processors). The global GPU market is currently around $26 bln and is growing at a rate of up to 34% per year[5].

2. Architecture based on field-programmable gate arrays (FPGA) — semiconductor devices that can be reprogrammed and change the topology of connections in use. The rated performance of these devices is relatively low — about 20 TFLOPS, however, the efficiency of using computing power is the highest among all the considered architectures. It is 6-7 times higher than that of graphics accelerators. The high efficiency of FPGA is due to the flexibility and speed of adjustment to the computational tasks being solved. According to Grand View Research, in 2020, the global FPGA market amounted to $ 9.85 bln, the expected market growth rate for the period up to 2027 is 9.7% per year[6].

---

[2] Glek P. Deep Learning: short tutorial. neurohive.io. URL: https:// neurohive.io /ru/osnovy-data-science/glubokoe-obuchenie-deep-learning-kratkij-tutorial/ (accessed: 06.11.2021) (In Russ.)

[3] Kak sokratit' izderzhki pri ispol'zovanii II. HitachiVantaraCorporation. URL: https://hitachi.cnews.ru/articles/2021-06-14_kak_sokratit_izderzhki_pri_ispolzovanii (accessed: 07.11.2021) (In Russ)

[4] Kak sokratit' izderzhki pri ispol'zovanii II. Op. cit.

[5] Global Graphics Processing Unit (GPU) Market Insights and Forecast to 2027. QYResearch. 2021. P. 116. URL: https://reports.valuates.com/market-reports/QYRE-Auto-25V3358/global-graphics-processing-unit-gpu (accessed: 10.11.2021)

[6] Field Programmable Gate Array Market, 2020 — 2027. Grand View Research, 2020. P. 130. URL: https://www.grandviewresearch.com/industry-analysis/fpga-market (accessed: 11.11.2021)

3. Architecture based on the advanced special integrated circuit (ASIC). Due to the narrow specialization of the computational problems to be solved, they can be much simpler, cheaper, and more compact. ASIC performance can reach 1000 TFLOPS, but the efficiency of using computing power, e.g., the number of recognized images, is about 2 times lower than in graphics accelerators. The growth rate of the ASIC market is significantly lower than that of the GPU market. In 2020, according to Global Industry Analysts, the global ASIC market amounted to $17.3 billion, the expected average annual market growth until 2027 is 7.7%[7].

4. Architecture based on single-chip accelerators (SoC). "System on a chip" SoC is a fully functional electronic device that has a motherboard, processor, and other components required for operation, placed on a single integrated circuit. SoC are common in mobile computers (smartphones), single board computers, and other embedded systems. At the same time, SoC have a significant potential use as part of hybrid computers. In addition, solutions are possible in the form of a single-chip SoC assembly with FPGA elements (Xilinx[8] Versal architecture for adaptive computing). The SoC market is currently very large, and it was worth $79.7 bln in 2020. For the period up to 2027, the market is projected to grow by 4.4% per year, by 2027, the market volume will reach $107.4 bln $[9].

Figures 1 and 2 show data on the actual and projected growth of the global market for chips for deep machine learning, prepared by Omdia[10] consulting company.

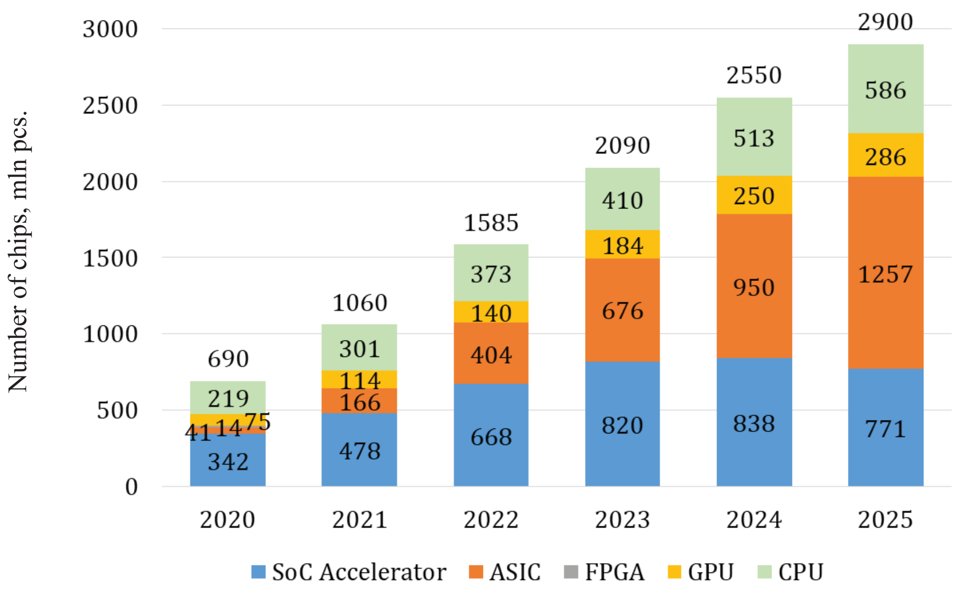

Fig. 1. Growth dynamics of number of chips for deep learning year-wise

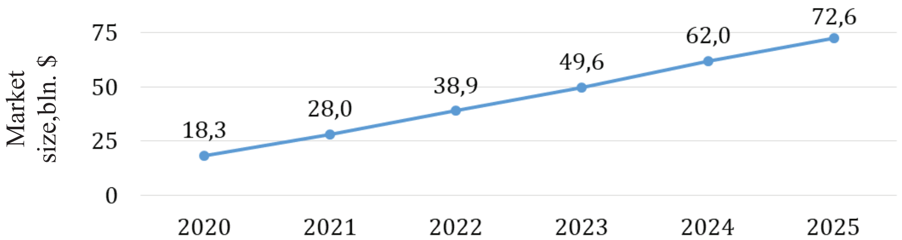

Fig. 2. Dynamics of the market for deep learning chips year-wise[11]

[7] ASIC - Global Market Trajectory & Analytics April 2021. Global Industry Analysts, Inc.; 2021. P. 185. URL: https://www.researchandmarkets.com/reports/5140939/asic-global-market-trajectory-and-analytics (accessed: 11.11.2021)

[8] Michael Feldman. Xilinx Unveils Its Most Ambitious Accelerator Platform. 2018. URL: https://www.top500.org/news/xilinx-unveils-its-most-ambitious-accelerator-platform/ (accessed: 10.11.2021)

[9] System-On-A-Chip (SoC) - Global Market Trajectory & Analytics. Report, April 2021. Global Industry Analysts, Inc.; 2021. URL: https://www.researchandmarkets.com/reports/2832316/system-on-a-chip-soc-global-market-trajectory (accessed: 11.11.2021)

[10] Joshi A. Deep Learning Chipsets Report – 2020. Omdia Marke, 2020. URL: https://omdia.tech.informa.com/products/deep-learning-chipsets-report---2020 (accessed: 11.11.2021)

[11] Joshi A. Deep Learning Chipsets Report – 2020. Op cit. (accessed: 12.11.2021)

The analysis shows that against the background of the general growth of the market, ASIC have the greatest prospects, GPU and SoC will also retain significant positions. For a fairly long term, GPU accelerators do not have an adequate replacement for solving complex problems, including in the learning process, and SoC are indispensable for mobile implementations of deep machine learning systems, as well as for parallel computing to offload the central processor. Rejection of FPGA in deep machine learning systems seems optional, although the share of such processors is likely to be relatively small.

One of the most promising directions in the development of hybrid computers is the use of tensor and other specialized coprocessors, such as machine vision processors. Such coprocessors can be based on the most common and high-performance ASIC, as well as FPGA or GPU. The difference between coprocessors and accelerators is in the degree of integration with the central processor. The central processor translates control instructions to the accelerator through a special memory area. The coprocessor monitors the flow of machine code instructions from RAM to the CPU and intercepts instructions appropriate to its functional purpose, such as tensor transform tasks, pattern recognition, etc. To solve large-scale problems that require long-term distributed computing, it is advisable to use an accelerator; for frequent and repeated execution of simple computing tasks, use a coprocessor, in which the central processor is not loaded and does not slow down data processing.

The operational properties of computers depend significantly on the architecture used. For solving deep machine learning problems, where up to 80% of computing power is spent, machines based on graphics accelerators are best suited. They have high performance in solving complex tasks that require a significant investment of time, have high flexibility and maximum calculation accuracy, but low relative performance. Specifically, for NVidia processors, it is 1.3–1.8 GOPS/W. ASIC-based computers have the highest absolute and relative performance. For neuIBM processors, e.g., the relative performance is 254 GOPS/W [4]. However, such machines have low flexibility and limited accuracy, so, it is advisable to use them when solving typical, e.g., matrix or tensor transformations, repetitive or multi-threaded tasks in real time.

FPGA-based computers have high parameters of flexibility, accuracy, absolute and relative performance. For Tegra TX1 processors, e.g., the relative performance is 70 GOPS/W. However, such machines have a relatively high cost, so it is advisable to use them for scientific purposes, when only a few computers of a given configuration are required, as well as for developing the architecture of mass-produced ASIC and SoC processors.

Despite the improvement in the architecture of computers, the potential for growth in capacities for high-performance computing will soon be exhausted. The number of transistors on a chip over the past 5 years has increased by about 12 times [5], and the amount of calculation in the process of machine learning has increased by 150 thousand times[12].

Neuromorphic computing. A possible way to address the lack of computing power for artificial neural systems with deep machine learning is to use neuromorphic computing and related chips. A neuromorphic chip is a processor based on the principles of the human brain. Such a chip simulates the work of neurons and their processes — axons and dendrites, which are responsible for the data transmission and perception. Connections between neurons are formed by synapses — special contacts through which electrical signals are transmitted.

Some of the best-known developments in this area include IBM TrueNorth neuromorphic processors and Intel Loihi processors. They use an asynchronous cluster architecture and a convolutional neural network model — a unidirectional multilayer network with alternating convolutional and subsampling layers. TrueNorth processor is based on 28 nm technologies, Loihi — on 14 nm [6].

[12]Thompson NC, Greenewald K, Lee K, et al. The Computational Limits of Deep Learning. arXiv preprint arXiv:2007.05558. 2020 (accessed: 12.11.2021)

TrueNorth NS16e-4 multiprocessor system, containing 100 mln neurons and designed to work with networks for deep machine learning, was introduced by IBM in 2018 [7]. Each chip contains 1 mln digital neurons and 256 mln synapses enclosed in 4096 synapse nuclei; power consumption of each chip is 70 mW.

Loihi processor, introduced in 2017, contains 131,000 artificial neurons and 131 mln synapses. In 2019–2020, Intel introduced two products based on Loihi — PohoikiBeach and PohoikiSprings. PohoikiBeach computing system, which includes 64 Loihi processors, has a total of 8.32 mln neurons and 8.32 bln synapses. PohoikiSprings Computing System Includes 768 Loihi processors, 100 mln neurons, and 100 bln synapses[13].

In Russia, work on the creation of neuromorphic processors has been going on for several years. In 2020, Motive Neuromorphic Technologies created the Altai neurochip [8]. The processor technology standard is 28 nm, power consumption is about 0.5 W, the crystal area is 64 mm^2 (for comparison: TrueNorth - 430 mm^2, Loihi - 60 mm^2). It has 131 thousand neurons, between them, there are 67 mln connections.

To assess the quality of neuromorphic processors, the following is used:

1. Absolute performance indicator. This is the number of billions of synoptic operations performed per second (GSOPS).

2. Energy efficiency indicator. This is the number of picojoules of energy expended in performing one synaptic operation (pJ/SOP).

TrueNorth processor has a performance of 58 GSOPS and an energy efficiency of 26 pJ/SOP[14]. Similar power efficiency (23.7 pJ/SOP [9]) is provided by Loihi processor.

The only competitor of neuromorphic processors in the implementation of neural networks with deep machine learning in the midterm (8–12 years) is hybrid computers with ASIC coprocessors. Such processors have a lower but comparable performance of synaptic operations and higher energy efficiency. In particular, ASIC processor described in [10] provides a synaptic performance of 8.7 GSOPS and an energy efficiency of 15.2 pJ/SOP.

The global market for neuromorphic chips is relatively new and therefore small. In 2020, its volume amounted to only $22.5 mln. At the same time, the growth rate of the market is very high. By 2026, the market will grow to $333.6 mln, which corresponds to an average annual growth of 47.4%[15].

Sometimes neuromorphic chips are understood as all types of processors that externally reproduce the work of neurons, regardless of the internal structure of the technical device, which may not correspond to the nature of the interaction of neurons. Such processors used to build artificial neural networks are properly called neural. Along with neuromorphic chips, neural processors also include processors (chips) with tensor and other specialized coprocessors for machine vision, speech recognition, etc. The world market for neural processors currently stands at $2.3 bln, and, by 2027, it will grow to $10.4 bln, thus, the average growth will be 24.2% per year[16].

Quantum computing. In the long term, the development of quantum computing can become a means of eliminating the shortage of computing power. Quantum computing solves problems through manipulating quantum objects: atoms, molecules, photons, electrons, and specially created macrostructures. Manipulations of quantum objects provide using:

— quantum superposition, which manifests itself in the ability of quantum systems to simultaneously be in all possible states;

[13] Intel Scales Neuromorphic Research System to 100 Million Neurons. Intel, 2020. URL: https://newsroom.intel.com/news/intel-scales-neuromorphic-research-system-100-million-neurons/?utm_source=ixbtcom#gs.7oc6iw (accessed: 12.11.2021)

[14] Neurochip "Altai". motivnt.ru. URL: https://motivnt.ru/neurochip-altai/ (accessed: 10.11.2021) (In Russ.).

[15] Neuromorphic Chip Market - Growth, Trends, COVID-19 Impact, and Forecasts (2021 - 2026). Mordor Intelligence, 2020. URL: https://www.mordorintelligence.com/industry-reports/neuromorphic-chip-market (accessed: 11.11.2021)

[16] Neuromorphic Chips - Global Market Trajectory & Analytics. Global Industry Analysts, Inc. 2021. 118 p. URL: https://www.researchandmarkets.com/reports/4805280/neuromorphic-chips-global-market-trajectory-and (accessed: 10.11.2021)

— quantum entanglement, which manifests itself in a strong relationship between the parameters of specially prepared quantum systems.

Devices for quantum computing are usually divided into two large classes [11]: general purpose quantum computers and quantum simulators. The former, like central processing units, can solve any algorithmic problem, and quantum simulators are analog computers for solving highly specialized problems.

Technologies for creating universal quantum computers are currently at the stage of formation. The created computers demonstrate “quantum superiority” in solving certain problems, but so far, they cannot be used to form artificial neural networks with deep machine learning. Companies that are most active in creating a quantum computer include:

1. Google. In 2018, a 72-qubit Bristlecone quantum processor was built, in 2019, a more accurate 53-qubit Sycamore quantum processor was built.
2. Intel. A 49-qubit TangleLake superconducting quantum chip was built in 2018.
3. IBM. In 2017, a 50-qubit quantum processor was created and tested, in 2019 — the world's first commercial 20-qubit quantum computer IBM Q SystemOne, etc.

The only adiabatic quantum computer on the market is D-WaveSystems, available in 16 to 2000 qubits, arranged in clusters of 8 qubits each.

The field of quantum simulators is also rapidly developing. One of the most complex simulators of this type is a 2017 joint development of the University of Maryland and the National Institute of Standards and Technology (USA). This 53-qubit simulator uses cold ytterbium ions as qubits. A similarly capable 51-qubit quantum simulator based on rubidium atoms was developed by a group of scientists at Harvard University and Massachusetts Institute of Technology.

A number of projects developing quantum computing technologies are also being implemented in Russia. In particular, for several years now, the development of a superconducting processor has been carried out by scientists from a consortium, which includes National University of Science and Technology (MISIS), Osipyan Institute of Solid State Physics of the Russian Academy of Sciences (ISSP RAS), Institute of Solid State Physics, Bauman Moscow State Technical University (MBSTU), Dukhov Automatics Research Institute (VNIIA), and other organizations. To date, the consortium has debugged the technology for manufacturing superconducting two-qubit circuits, experimentally characterized and demonstrated two-qubit logic gates that perform quantum entanglement, which is required for the operation of quantum processors. The reliability of logical operations is in the range of 85–95%.

In 2020, $675 mln was invested in quantum computing in the world, which is more than 3 times the investment amount in 2019 ($211 mln). In 2021, the volume of investments in quantum computing exceeds $800 mln [12].

Trust management systems. One of the basic requirements for management systems, including production ones, is to provide them with the required level of trust. According to GOST R 54583-2011 “Information technology. Security techniques. A framework for IT security assurance. Part 3. Analysis of assurance methods”, the purpose of providing credibility is to create confidence in the reliable functioning of the product under given conditions. To provide this, the information system must have the following operational properties [13]:

— functional reliability, i.e., the ability to perform its function with a given reliability, which in turn is normalized by the number of failures, the error and repeatability of the calculation results;

— information security, i.e., the ability to provide a given level of confidentiality, availability and integrity of information: stored, transmitted, received, and processed during the operation of the system.

The subject of this research is control systems that relate to information. Therefore, the above requirements for performance properties are also valid for them. However, management systems have their own specifics in the definition of trust. A trust control system must have:

— the ability to control, e.g., a robot, a machine tool, an enterprise, etc., according to a given number of parameters with a specified reliability, which is regulated by the number of failures, error, and repeatability, and with a given performance, which in turn is regulated by the time of data processing and execution of control commands;

— the ability to control the elements, structure and processes of the system at the hardware and software levels to provide information security.

If the control system has the function of deep machine learning, then the fulfillment of the first of these requirements imposes severe restrictions on the means of technical implementation used. This should be the optimal computer for the formation of a convolutional neural network with high parameters of performance, accuracy, and calculation reliability.

If we do not consider the option of using quantum processors, the full-featured implementations of which are not yet available, then neither hybrid computers based on all the considered architectures, nor computers based on neuromorphic processors fully comply with the first requirement. Computers based on ASIC and neuromorphic processors do not provide high accuracy and reliability, and hybrid computers with GPU or SoC accelerators are not optimal for real-time operation, including impedance.

A certain compromise is provided when using FPGA-based hybrid computers, however, such machines have a high cost in mass production, significantly lower performance than ASIC machines, and significantly less complex computing capabilities than GPU machines. Another compromise option is the simultaneous use of a CPU with a graphics accelerator to solve complex tasks in the process of machine learning and tensor or other highly specialized ASIC-based coprocessors for real-time data processing.

The second requirement, although technical in content, in practice acts as an economic one. The implementation of a control system for process equipment with deep machine learning is possible only through a convolutional neural network, the control of which from the outside is not possible. Information security can be only provided that the main part of the computer will be created by domestic manufacturers who have been certified in the field of information security.

At present, the main part of control systems in Russia is built on the basis of foreign microelectronic components. The share of such components exceeds 85% [14]. Providing information security in the case of using imported components in computers does not have an unambiguous solution and depends on the structure of the created artificial neural network and the order of its use. In particular, when using hybrid computers, information security can be significantly improved through localizing data transfer between the central processor and the accelerator or coprocessor.

Research Results. The analysis of deep machine learning models, basic technologies, and architecture of computers, as well as the requirements for providing confidence in control systems using deep machine learning, allows us to draw the following conclusions:

1. There is an objective problem of lack of computing power for solving problems of deep machine learning. None of the currently existing technologies can solve the full range of training and impedance problems.

2. Since deep machine learning is implemented on the basis of a model of convolutional neural networks, their external control to provide information security and reliability of work is not possible. The only option is developer control, which also has limited capabilities. This determines the need for the production of processors required for ANN in Russia.

3. The practical implementation of trust control systems with deep machine learning based on existing technologies for a significant part of the tasks in real time cannot be provided, for the other part of the tasks, such an implementation is associated with a significant drop in performance.

4. The performance gain of trust control systems can be based on improving the architecture of hybrid computers, including the simultaneous use of processors of different architectures that are optimal for solving the corresponding problems of analysis and control.

Discussion and Conclusions. This paper analyzes and discusses the relevance and implementation of machine learning in the context of digital transformation of industry. The scientific problem covered in the work is in the insufficient development of the technical level of modern computers to provide high performance of algorithms based on deep machine learning. Attention is drawn to the problem of information security, which is one of the prerequisites for the development of domestic processors for ANN. Based on the analysis of the requirements for trust control systems, the objective difficulties of their implementation based on existing technologies and the need to develop new approaches to the architecture of computers are determined.

References

1. Zelensky A, Semenishchev E, Alepko A, et al. Using neuro-accelerators on FPGAs in collaborative robotics tasks. SPIE Optical Instrument Science, Technology, and Applications II. 2021;11876:1187600. https://doi.org/10.1117/12.2600582

2. Zelenskii AA, Pismenskova MM, Voronin VV. Control of Collaborative Robot Systems and Flexible Production Cells on the Basis of Deep Learning. Russian Engineering Research. 2019;39:1065–1068. http://dx.doi.org/10.3103/S1068798X19120256

3. Voronin VV, Sizyakin RA, Zhdanova M, et al. Automated visual inspection of fabric image using deep learning approach for defect detection. Automated Visual Inspection and Machine Vision IV. 2021;11787:117870 http://dx.doi.org/10.1117/12.2592872

4. Phi-Hung Pham, Jelaca D, Farabet C, et al. NeuFlow: Dataflow Vision Processing System-on-a-Chip. In: Proc. IEEE 55th International Midwest Symposium on Circuits and Systems (MWSCAS). 2012. P. 1044–1047. http://dx.doi.org/10.1109/MWSCAS.2012.6292202

5. Shuremov EL. Whether it is worth being fond of big data? Accounting. Analysis. Auditing. 2020;7:17–29. https://doi.org/10.26794/2408-9303-2020-7-2-17-29

6. Jing Pei, Lei Deng, Sen Song, et al. Towards artificial general intelligence with hybrid Tianjic chip architecture. Nature. 2019;572:106–111. http://dx.doi.org/10.1038/s41586-019-1424-8

7. Modha D. TrueNorth: from zero to 64 million neurons. Open Systems. DBMS. 2019;3:8.

8. Akopyan A, Sawada J, Cassidy A, et al. TrueNorth: design and tool flow of a 65 mw 1 million neuron programmable neurosynaptic chip. IEEE transactions on computer-aided design of integrated circuits and systems. 2015;34:1537–1557. http://dx.doi.org/10.1109/TCAD.2015.2474396

9. Mike Davies, Narayan Srinivasa, Tsung-Han Lin, et al. Loihi: A neuromorphic manycore processor with on-chip learning. IEEE Micro. 2018;38:82–99. http://dx.doi.org/10.1109/MM.2018.112130359

10. Kim J, Koo J, Kim T, et al. Efficient synapse memory structure for reconfigurable digital neuromorphic hardware. Frontiers in neuroscience. 2018;12:829. http://dx.doi.org/10.3389/fnins.2018.00829

11. Fedorov A. Kvantovye vychisleniya: ot nauki k prilozheniyam. Open Systems. DBMS. 2019;3:14. (In Russ.)

12. Bobier J-F, Langione M, Tao E, et al. What Happens When 'If' Turns to 'When' in Quantum Computing? BCG Digital Transformation. 2021. 20 p.

13. Sabanov AG. Doverennye sistemy kak sredstvo protivodeistviya kiberugrozam. Zaŝita informacii. Inside. 2015;63:17–21.

14. Kalyaev IA, Melnik EV. Trusted control systems. Mechatronics, Automation, Control. 2021;22:227–236. https://doi.org/10.17587/mau.22.227-236 (In Russ.)

Received 27.12.2021

Revised 22.01.2022

Accepted 26.01.2022

About the Authors:

Zelensky, Alexander A., Director of the Institute of Digital Intelligent Systems, Moscow State University of Technology "STANKIN" (3a, Vadkovsky Lane, Moscow, 127005, RF), Cand.Sci. (Eng.), associate professor, ResearcherID, ScopusID, ORCID, Zelenskyaa@gmail.com

Abdullin, Tagir H., lecturer of the Industrial Electronics and Intelligent Digital Systems Department, Moscow State University of Technology "STANKIN" (3a, Vadkovsky Lane, Moscow, 127005, RF), senior engineer, ScopusID, ORCID, everestultimate@yandex.ru

Zhdanova, Marina M., Junior Research Scholar, Moscow State University of Technology "STANKIN" (3a, Vadkovsky Lane, Moscow, 127005, RF), ResearcherID, ScopusID, ORCID, mpismenskova@mail.ru

Voronin, Viacheslav V., Associate Director of the Center for Cognitive Technologies and Machine Vision, Moscow State University of Technology "STANKIN" (3a, Vadkovsky Lane, Moscow, 127005, RF), Cand.Sci. (Eng.), associate professor, ResearcherID, ScopusID, ORCID, voronin_sl@mail.ru

Gribkov, Andrey A., Director of the Analytical Center, Moscow State University of Technology "STANKIN" (3a, Vadkovsky Lane, Moscow, 127005, RF), Dr.Sci. (Eng.), professor, ResearcherID, ScopusID, ORCID, andarmo@yandex.ru

Claimed contributorship

A. A. Zelensky: basic concept formulation; research objectives and tasks setting; text preparation; formulation of conclusions. T. H. Abdullin and M. M. Zhdanova: conducting research; analysis of existing approaches. V. V. Voronin and A. A. Gribkov: analysis of the research results; the text revision; correction of the conclusions.

All authors have read and approved the final manuscript.

INFORMATION TECHNOLOGY, COMPUTER SCIENCE, AND MANAGEMENT

UDC 004.11.5
https://doi.org/10.23947/2687-1653-2022-22-1-67-75

Original article

Comparison of machine learning models for coronavirus prediction

Brou Kouame Amos ✉, **Ivan Smirnov**, **Mabouh Moise Hermann**
Peoples' Friendship University of Russia (RUDN) (Moscow, Russian Federation)
✉ broukouameamos9@gmail.com

Introduction. Coronavirus, also known as COVID-19, was first detected in Wuhan, China, in December 2019. It is a family of viruses ranging from the common cold to severe acute respiratory syndrome (SARS). The symptoms of such a virus are similar to those of a cold or seasonal allergies. Like other respiratory viruses, it is mainly transmitted through airborne droplets when coughing or sneezing. Therefore, the recognition of COVID-19 requires careful laboratory analysis, and the reduction of recognition resources is a major challenge. On 11 March, 2020, the World Health Organization (WHO) declared COVID-19, caused by SARS-CoV-2, a pandemic, as there had been an exponential increase in cases worldwide, and demand for intensive beds and related structures had far exceeded existing capacity. The first examples of this are the regions of Italy. Brazil registered the first case of SARS-CoV-2 on 02/26/2020. Transmission of the virus in this country shifted very quickly from imported cases to local and, finally, community missions, with the Brazilian federal government announcing national community transmission on 03/20/2020. As of March 23, in the state of São Paulo with a population of about 12 million people, where the Israelita Albert Einstein Hospital is located, 477 cases of the disease and 30 related deaths were registered, and on March 27, there were already 1223 cases of COVID-19 with 68 concomitant deaths. To slow the spread of the virus in the state of São Paulo, quarantines and social distancing measures were introduced. One of the motivations for this challenge is the fact that, in the context of an extensive healthcare system with the possible limitation of SARS-CoV-2 testing, it is not practical to test every case, and test results can only be used in testing the target subpopulation. The study objective is to build a model based on machine learning that can predict the detection of SARS-CoV-2 from medical data. For this, various classification models of machine learning are compared, and the best one to predict coronaviruses is determined. The comparison is based on individuals in class 1, i.e., those with a positive test. Therefore, it is required to determine the machine learning model with the best response and F1 score for class 1.

Materials and Methods. An open-source data set from the Israelita Albert Einstein Hospital in São Paulo, Brazil, was taken as a basis. The following machine learning models were used for the study: RandomForests (RF), K-Nearest Neighbor (KNN), Support Vector Machine (SVM), Logistic Regression (LR), Decision Tree (DT) and AdaBoost (AB), as well as the 10-time cross-validation technique. Some machine learning performance measures, such as accuracy, recall, and F1 score were evaluated.

Results. Out of a total of 5,644 people tested during the COVID-19 pandemic, 5,086 people tested negative and 558 people tested positive. At the same time, support for machine vectors showed the best results in detecting coronavirus with a recall of 75 % and an F1 score of 60 % compared to models: Random drill, KNN, LR, AB, and DT.

Discussion and Conclusions. It was found that when using AB algorithms, greater accuracy is achieved, but the stability of the LSVM algorithm is higher. Therefore, it can be recommended as a useful tool for detecting COVID-19.

***Keywords*:** COVID-19 detection, classification, machine learning models.

For citation: Brou Kouame Amos, I. Smirnov, Mabouh Moise Hermann. Comparison of machine learning models for coronavirus prediction. Advanced Engineering Research, 2022, vol. 22, no. 1, pp. 67–75. https://doi.org/10.23947/2687-1653-2022-22-1-67-75

1. Introduction

The coronavirus is a very severe acute respiratory syndrome caused by the SARS-COV-2 virus. This virus, which can infect humans or animals, was discovered in the Chinese region of Wuhan, more precisely in the province of Hubei, during the pneumonia epidemic of January 2020 [1, 2]. It is therefore the seventh human coronavirus. To everyone's surprise, this virus spread worldwide, causing 318,599 deaths and 4,806,299 infected persons [3].

SARS-CoV-2, SARS-CoV and MERS-COV (Middle East Respiratory Syndrome Coronavirus) cause severe pneumonia with a mortality rate of 2.9 %, 9.6 % and 36 % respectively [4–6].

The other four viruses, namely OC43, NL63, HKU1, and 229E, are responsible for illnesses related to mild symptoms [7].

It should be noted that since the Covid-19 epidemic, there has been much speculation about the origin of this virus [8]. Some said that it was the result of work done in a laboratory. However, after studies conducted on genetic data, this hypothesis was dismissed [9]. Analysis and comparison with the genomes of previously known coronaviruses clearly show that SARS-COV-2 is different from other coronaviruses [8, 11]. The virus responsible for the coronavirus (SARS-COV-2) is similar to the SARS virus of bats [2]. Thus, the Covid-19 virus is believed to have originated from a bat coronavirus that became infectious to humans while acquiring genes specific to pangolin coronaviruses. It should be noted that the actual causes of Covid-19 are still unclear.

The symptoms of Covid-19 are similar to those of seasonal flu. The disease is more severe in the elderly and in people who are vulnerable to certain chronic diseases. Patients with Covid-19 can have symptoms ranging from mild to severe. The most common symptoms are fever (83 %), cough (82 %) and breathlessness (31 %) [12]. In patients with pneumonia, the X-ray of the lungs shows numerous mottles and ground glass opacity [12, 13].

Gastrointestinal symptoms associated with patients with Covid-19 include vomiting, diarrhoea, and abdominal pain [12, 14].

We also see a decrease in lymphocytes and eosinophils, lower haemoglobin levels, and an increase in white blood cells and neutrophils [15–18].

The manifestation of Covid-19 in children is different from that in adults. In children, the symptoms are mild. However, in some children, we have seen severe and fatal cases [19–27].

Like all other viruses, Covid-19 is transmitted mainly by the respiratory route. Among these routes of transmission, we have droplet transmission, which is the most widespread [28, 29]. Other transmission routes exist, namely the faecal route, via saliva. Indeed, SARS-CoV-2 RNA was found in the stool of a patient with Covid-19 [31]. SARS-CoV-2 RNA can be detected on inanimate surfaces (door handles). People who have been in contact with these surfaces could be contaminated [29].

This model will make it possible to identify positive and negative cases from the dataset studied and the elements responsible for COVID-19. The proposed prediction model ensures that it tracks the results regarding this epidemic situation so that the huge economic losses, the spread of the community, the amount of detachment social gens can be detected and a precise decision can also be made accordingly. This method will allow government authorities to put in place preventive measures based on our future work to predict the onset of this disease in the future.

2. Data Resources and Methods

The dataset used was uploaded to Kaggle. It is open source and available on this link kaggle.com/einsteindata4u/covid19. This dataset contains anonymized data in accordance with best international practices and patient recommendations at the Israelita Albert Einstein Hospital in São Paulo, Brazil. This section describes the proposed approach and a detailed overview of the tasks. These tasks can help to understand and extract knowledge from COVID 19 data, which can help countries contain the spread of the virus, raise awareness, launch initiatives, determine if mitigation has a positive effect or not, identify other factors affecting the virus, etc. This will allow countries to prepare for what may happen in the near future. This could help save lives and alleviate the agony. Epidemiological information includes various characteristics of the case studied, including case identification, age, sex, target value, lymphocytes, leukocytes, monocytes, hco3, etc.

2.1. Data Pre-processing

In data analysis, the most important step is pre-processing. However, it is not clear what methods of pre-treatment the author used. This part must be completed.

2.2. Data Transformation

The data is transformed to be processed and stored in. xls for further processing. All data were normalized to have a mean of zero and a unit standard deviation. With a dataset containing 111 characteristics, data mining eliminated missing values (78 characteristics) and retained important characteristics (33). This exploratory analysis of the data also allowed us to identify two categories of characteristics, namely virus-related characteristics and blood-related characteristics. The target value is divided into two categories which are negative cases coded by 0 and positive cases coded by 1.

The dataset from the Israelita Albert Einstein Hospital in São Paulo is divided into training and test data. 70 % of the data is used for predictive model training, and the remaining 30 % is used for testing. The objective of model training is to adapt the model using data from the training set. After the model is formed, the prediction models sound tested to evaluate performance in the test datasets.

2.3. The Proposed Models

This section describes the different machine learning models used in this paper. These models are: Random Drills (RF), K-plus Close Neighbors (KNN), Linear Support Vector Machine (SVM), Logistic Regression (LR), Decision Tree (DT), and AdaBoost (AB).

Random Forest (RF)

Random forests (RF) or random decision forests were first proposed in 1995. This is a general classification training method that tends to work better than traditional decision tree classification methods (Gangaie et al., 2019). Decision trees are the fundamental RF classifiers that vote for each of the forecasts, and the survival prediction is based on the majority voting method in each tree (Breiman, 2001). The accuracy of each tree and the independence of the trees from each other provide the reliability of the classification. We used 100 trees to predict two target classes, survival or death of patients with hepatitis.

Nearest Neighbor (KNN)

The K-Nest Neighbor (KNN) classifier is one of the most commonly used classification algorithms. This algorithm can be used in several applications. It saves all valid attributes and classifies new attributes according to their similarity dimension. KNN is a statistical recognition model method for detecting the different classes of a model. A tree data structure is used to determine the distance between the point of interest and the points in the training dataset. The attribute is classified by its neighbors. In the classification method, the value of k is always a positive integer closest to the neighbor. The nearest visions are selected from a set of classes or property values of the object.

Support Vector Machine (SVM)

SVM-controlled learning method is used for classification and regression [29]. This algorithm is a relatively new approach and has performed well in recent years. The SVM classifier is based on linear classifiers and in the data separated by a row, the SVM isolates the objects in the specified classes. It can also identify and classify instances that are not supported by the data. The only extension of this algorithm is to perform a regression analysis to obtain a linear function, and another extension teaches to classify the elements to obtain a classification of individual elements.

Logistic Regression Model (LR)

Logistic regression is the corresponding regression analysis that should be performed when the dependent variable is dichotomous (binary). Like all regression analyses, logistic regression is predictive analysis. It is used to describe the data and explain the relationship between a dependent binary variable and one or more nominal, ordinal, interval or ordinal independent variables, report [30, 31]. This approach assumes that the binary result follows a binomial distribution.

Decision Tree (DT) Model

The Decision Tree is a controlled learning method that is used to solve classification and regression problems, but it is more used to solve classification. This is a powerful classification method for disease prediction. This is a tree model where the internal nodes represent the characteristics of a data set, the branches represent the decision rules, and each leaf node represents a result. The decision tree consists of two nodes, a decision node and a leaf node. Decision nodes have multiple branches and are used to make a decision, while leaf nodes are the result of those decisions.

Model AdaBoost (AB)

AdaBoost, short for "Adaptive Boosting", is the first boost algorithm proposed by Freund and Schapire in 1996. Its goal is to turn weak predictors into strong predictors to solve classification problems. For classification, the final equation can be put under the heading below:

$$F(x)=\text{sign}\left(\sum_{m=1}^{M}\theta_m\, f_{m(x)}\right) \qquad (1)$$

Where f_m denotes the weak classifier m and m denotes the corresponding weight. AdaBoost can be used for face recognition, as it is a standard algorithm for detecting faces in images. AdaBoost is fast, requires no setup, and is simple and easy to program. Plus, it has the flexibility to be able to be combined with any machine learning algorithm.

2.4. Evaluation of Performance Measures

For the comparison of the different classification algorithms used in this paper, some metrics were evaluated. These are accuracy, recall, and F1-score. These metrics are calculated based on true positives (TP), true negatives (TN), false positives (FP), and false negatives (FN). The standardized confusion matrix illustrates the relationship between classification results and predicted classes. The level of the classification performance is calculated by the number of samples correctly and incorrectly classified in each class.

The accuracy is calculated based on the total number of correct predictions, defined as follows:

$$\text{Accuracy} = \frac{TP+TN}{TP+FN+TN+FP} \qquad (2)$$

Recall, or sensitivity, is the proportion of true positive predictions that have been correctly identified, defined as follows:

$$\text{Recall} = \frac{TP}{TP+FN} \qquad (3)$$

The F1 score is the harmonic mean of accuracy and recall, and it is calculated by:

$$\text{Score F1} = \frac{TP}{TP+\frac{1}{2}(FP+FN)} \qquad (4)$$

3. Result

The objective of this paper is to compare the different models of machine learning for the detection of coronavirus. Our task was to find out which machine learning model has the best recall and f1-score for Class 1. The learning machine models used are: Radom drill, k-nearest neighbor, logistic regression, support vector machine, AdaBoost, and decision tree. Out of a total of 5,644 people tested for COVID-19, 5,086 people tested negative and 558 people tested positive. The results of our study are presented in Figure 1 and Figure 3. These results show that the vector-machine gave better results with a recall of 75 % and an F1 score of 60 %. The different learning curves were also traced in order to understand the phenomenon of over-fitting and under-fitting Figure 2. Indeed, the learning curve is very well known to data scientists, the learning curve shows the efficiency and quality of learning of our machine learning model. Learning curves are widely used as a diagnostic tool in machine learning for algorithms that incrementally learn a training data set. This means that we increase our dataset by a certain step, and then we see the performance of our model. The model can be evaluated on the training dataset and on the exception validation dataset after each update during training, and it traces the measured performance. This can be represented as a curve.

```
RandomForest
[[91  4]
 [11  5]]
              precision    recall  f1-score   support

           0       0.89      0.96      0.92        95
           1       0.56      0.31      0.40        16

    accuracy                           0.86       111
   macro avg       0.72      0.64      0.66       111
weighted avg       0.84      0.86      0.85       111
```

```
AdaBoost
[[91  4]
 [ 9  7]]
              precision    recall  f1-score   support

           0       0.91      0.96      0.93        95
           1       0.64      0.44      0.52        16

    accuracy                           0.88       111
   macro avg       0.77      0.70      0.73       111
weighted avg       0.87      0.88      0.87       111
```

```
KNN
[[88  7]
 [ 8  8]]
              precision    recall  f1-score   support

           0       0.92      0.93      0.92        95
           1       0.53      0.50      0.52        16

    accuracy                           0.86       111
   macro avg       0.72      0.71      0.72       111
weighted avg       0.86      0.86      0.86       111
```

```
DecisionTree
[[86  9]
 [11  5]]
              precision    recall  f1-score   support

           0       0.89      0.91      0.90        95
           1       0.36      0.31      0.33        16

    accuracy                           0.82       111
   macro avg       0.62      0.61      0.61       111
weighted avg       0.81      0.82      0.81       111
```

```
Logistic_Regression
[[92  3]
 [10  6]]
              precision    recall  f1-score   support

           0       0.90      0.97      0.93        95
           1       0.67      0.38      0.48        16

    accuracy                           0.88       111
   macro avg       0.78      0.67      0.71       111
weighted avg       0.87      0.88      0.87       111
```

```
SVM
[[83 12]
 [ 4 12]]
              precision    recall  f1-score   support

           0       0.95      0.87      0.91        95
           1       0.50      0.75      0.60        16

    accuracy                           0.86       111
   macro avg       0.73      0.81      0.76       111
weighted avg       0.89      0.86      0.87       111
```

Fig. 1. Classification report of different machine learning models

Fig. 2. Learning curve of different machine learning models

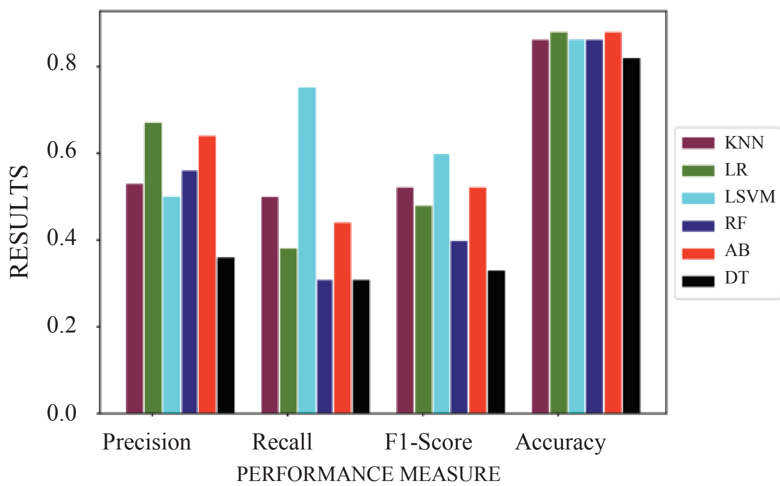

Fig. 3. Results of predictions from various machine learning techniques

Figure 3 shows the performance of the different machine learning algorithms according to the performance measures used in this paper. We see that for recall and F1-score, LSVM outperforms the other machine learning models used, namely LR, KNN, RF, AB, and DT. For accuracy, LR is much better than the others. As for accuracy, we find that LR and AB performed better than the other models. In this paper, we chose recall and F1 score to measure the performance of the model. Recall allowed us to correctly identify the Covid-19 positive test subjects among all the real positive cases. As for the F1 score, we used it because we had an imbalance between different classes, i.e., positive and negative cases.

4. Discussion and Conclusion

The data used in this paper was collected at the Israelita Albert Einstein Hospital in São Paulo, Brazil. After an exploratory analysis, two categories of characteristics were identified. These are the characteristics related to the virus and the characteristics related to the blood. Out of a total of 5,644 people tested with COVID-19, 5,086 people tested negative and 558 people tested positive. The results of this study clearly illustrated that in relation to our goal, machine vector support showed better results in coronavirus detection with a recall of 75 % and an F1 score of 60 %. This co-calculation was done with the other machine learning models, namely the Radom drill, the k-nearest neighbor, the logistic regression, the AdaBoost, and the decision tree. As such, this model can be useful for the diagnosis of COVID-19. However, it is possible to optimize the parameters of this model in order to improve its performance.

After the analysis of the learning curve in Figure 2, we find that apart from the supporting sensor, other machine learning models can be studied for the detection of COVID-19. These include AdaBoost and k-nearest neighbor. Indeed, we find that if we perform a little more advanced optimization of the parameters of these models, they could be candidates for the diagnosis of COVID-19 because the difference between the learning score curve and the validation score curve would have reduced the model's ability to generalize.

References

1. Zhou P, Yang XL, Wang XG, et al. A pneumonia outbreak associated with a new coronavirus of probable bat origin. Nature. 2020;579:270–273. https://doi.org/10.1038/s41586-020-2012-7

2. Wu F, Zhao S, Yu B, et al. A new coronavirus associated with human respiratory disease in China. Nature. 265–269. https://doi.org/10.1038/s41586-020-2008-3

3. World Health Organization Coronavirus Disease 2019 (COVID-19) Situation Report-97. Available from: https://www.who.int/docs/default-source/coronaviruse/situation-reports/20200426-sitrep-97-covid-19.pdf

4. Wang C, Horby PW, Hayden FG, et al. A novel coronavirus outbreak of global health concern. Lancet. 2020;395:470–473. https://doi.org/10.1016/S0140-6736(20)30185-9

5. Hui DSC, Zumla A. Severe acute respiratory syndrome: historical, epidemiologic, and clinical features. Infect Dis Clin North Am. 2019;33:869–889. https://doi.org/10.1016/j.idc.2019.07.001

6. Azhar EI, Hui DSC, Memish ZA, et al. The Middle East respiratory syndrome (MERS). Infect Dis Clin North Am. 2019;33:891–905. https://doi.org/10.1016/j.idc.2019.08.001

7. Corman VM, Muth D, Niemeyer D, et al. Hosts and sources of endemic human coronaviruses. Adv Virus Res. 2018;100:163–188. https://doi.org/10.1016/bs.aivir.2018.01.001

8. Andersen KG, Rambaut A, Lipkin WI, et al. The proximal origin of SARS-CoV-2. Nat Med. 2020;26:450–452. https://doi.org/10.1038/s41591-020-0820-9

9. Almazán F, Sola I, Zuñiga S, et al. Coronavirus reverse genetic systems: infectious clones and replicons. Virus Res. 2014;189:262–270. https://doi.org/10.1016/j.virusres.2014.05.026

10. Nao N, Yamagishi J, Miyamoto H, et al. Genetic predisposition to acquire a polybasic cleavage site for highly pathogenic avian influenza virus hemagglutinin. mBio. 2017;8:e02298. http://dx.doi.org/10.1128/mBio.02298-16

11. Huang C, Wang Y, Li X, et al. Clinical features of patients infected with 2019 novel coronavirus in Wuhan, China. Lancet. 2020;395:497–506. https://doi.org/10.1016/S0140-6736(20)30183-5

12. Wang D, Hu B, Hu C, et al. Clinical characteristics of 138 hospitalized patients with 2019 novel coronavirus-infected pneumonia in Wuhan, China. JAMA. 2020;323:1061. https://doi.org/10.1001/jama.2020.1585

13. Zhu N, Zhang D, Wang W, et al. A novel coronavirus from patients with pneumonia in China, 2019. N Engl J Med. 2020;382:727–733. https://doi.org/10.1056/NEJMoa2001017

14. Chen N, Zhou M, Dong X, et al. Epidemiological and clinical characteristics of 99 cases of 2019 novel coronavirus pneumonia in Wuhan, China: a descriptive study. Lancet. 2020;395:507–513. https://doi.org/10.1016/S0140-6736(20)30211-7

15. Lippi G, Plebani M. The critical role of laboratory medicine during coronavirus disease 2019 (COVID-19) and other viral outbreaks. Clin Chem Lab Med. 2020;58:1063–1069. https://doi.org/10.1515/cclm-2020-024

16. Bhargava A, Fukushima EA, Levine M, et al. Predictors for severe COVID-19 infection. Clin Infect Dis. 2020;71:1962-1968 https://doi.org/10.1093/cid/ciaa674

17. Wang CZ, Hu SL, Wang L, et al. Early risk factors of the exacerbation of coronavirus disease 2019 pneumonia. J Med Virol. 2020;91:2593-2599 https://doi.org/10.1002/jmv.26071

18. Hamming I, Timens W, Bulthuis ML, et al. Tissue distribution of ACE2 protein, the functional receptor for SARS coronavirus. A first step in understanding SARS pathogenesis. J Pathol. 2004;203:631–637. https://doi.org/10.1002/path.1570

19. Renu K, Prasanna PL, Valsala Gopalakrishnan A. Coronaviruses pathogenesis, comorbidities and multi-organ damage — a review. Life Sci. 2020;255:117839. https://doi.org/10.1016/j.lfs.2020.117839

20. Long B, Brady WJ, Koyfman A, et al. Cardiovascular complications in COVID-19. Am J Emerg Med. 2020;38 :1504-1507 https://doi.org/10.1016/j.ajem.2020.04.048

21. Ruan Q, Yang K, Wang W, et al. Clinical predictors of mortality due to COVID-19 based on an analysis of data of 150 patients from Wuhan, China. Intensive Care Med. 2020;46:846–848. https://doi.org/10.1007/s00134-020-05991-x

22. Lippi G, Favaloro EJ. D-dimer is associated with severity of coronavirus disease 2019: a pooled analysis. Thromb Haemost. 2020;120:876–878. http://dx.doi.org/10.1055/s-0040-1709650

23. Lang J, Yang N, Deng J, et al. Inhibition of SARS pseudovirus cell entry by lactoferrin binding to heparan sulfate proteoglycans. Plos One. 2011;6:e23710. https://doi.org/10.1371/journal.pone.0023710

24. Vicenzi E, Canducci F, Pinna D, et al. Coronaviridae and SARS-associated coronavirus strain HSR1. Emerging Infect Dis. 2004;10:413–418. https://doi.org/10.3201/eid1003.030683

25. Belen-Apak FB, Sarialioglu F. The old but new: can unfractioned heparin and low molecular weight heparins inhibit proteolytic activation and cellular internalization of SARSCoV2 by inhibition of host cell proteases? Med Hypotheses. 2020;142:109743. https://doi.org/10.1016/j.mehy.2020.109743

26. Henry BM, Benoit SW, Santos de Oliveira MH, et al. Laboratory abnormalities in children with mild and severe coronavirus disease 2019 (COVID-19): a pooled analysis and review. Clin Biochem. 2020;81:1–8. https://doi.org/10.1016/j.clinbiochem.2020.05.012

27. Sanna G, Serrau G, Bassareo PP, et al. Children's heart and COVID-19: Up-to-date evidence in the form of a systematic review. Eur J Pediatr. 2020;179:1079-1087 https://doi.org/10.1007/s00431-020-03699-0

28. Leung NHL, Chu DKW, Shiu EYC, et al. Respiratory virus shedding in exhaled breath and efficacy of face masks. Nature Med. 2020;26:676–680. https://doi.org/10.1038/s41591-020-0843-2

29. Abdi MJ, Giveki D. Automatic detection of erythemato-masquamous diseases using PSO-SVM based on association rules. Technical applications of artificial intelligence. 2013;26:603-608. https://doi.org/10.1016/j.engappai.2012.01.017

30. McDonald JH. Handbook of Biological Statistics, 3rd ed. Sparky House Publishing: Sparky House Publishing; 2014.

31. Mangiafico SS. An R companion for the handbook of biological statistics, 1.3.3 ed. New Brunswick, NJ: Rutgers Cooperative Extension; 2015.

Received 02.02.2022

Revised 28.02.2022

Accepted 05.03.2022

About the Authors:

Brou Kouame Amos, postgraduate of the Information Technology Department, Peoples' Friendship University of Russia (RUDN) (6, Miklikho-Maklaya St., Moscow, 117198, RF), ORCID, broukouameamos9@gmail.com

Smirnov, Ivan V., associate professor of the Information Technology Department, Peoples' Friendship University of Russia (RUDN) (6, Miklikho-Maklaya St., Moscow, 117198, RF), Cand.Sci. (Phys.-Math.), associate professor, Scopus, ORCID, smirnov-iv@rudn.ru

Mabouh Moise Hermann, postgraduate of the Information Technology Department, Peoples' Friendship University of Russia (RUDN) (6, Miklikho-Maklaya St., Moscow, 117198, RF), ORCID, mrmabouhmoise@gmail.com

Claimed contributorship

Brou Kouame Amos: basic concept formulation; research objectives and tasks; data pre-processing; analysis of research results. Mabouh Moise Hermann: text preparation; formulation of conclusions; data collection; the text revision. I. V. Smirnov: work control; the text revision; correction of the conclusions.

All authors have read and approved the final manuscript.